# Structural Enzymology of Sulfide Oxidation by Persulfide Dioxygenase and Rhodanese

by

Nicole A. Motl

A dissertation submitted in partial fulfillment
of the requirements for the degree of
Doctor of Philosophy
(Biological Chemistry)
in the University of Michigan
2017

Doctoral Committee

Professor Ruma Banerjee, Chair
Assistant Professor Uhn-Soo Cho
Professor Nicolai Lehnert
Professor Stephen W. Ragsdale
Professor Janet L. Smith

Nicole A. Motl

nimotl@umich.edu

ORCID iD: 0000-0001-6009-2988

## ACKNOWLEDGEMENTS

I would like to take this opportunity to acknowledge the many people who have provided me with guidance and support during my doctoral studies. First I would like to express my appreciation and gratitude to my advisor Dr. Ruma Banerjee for the mentorship, guidance, support and encouragement she has provided. I would like to thank my committee members Dr. Uhn-Soo Cho, Dr. Nicolai Lehnert, Dr. Stephen Ragsdale and Dr. Janet Smith for their advice, assistance and support. I would like to thank Dr. Janet Smith and members of Dr. Smith's lab, especially Meredith Skiba, for sharing their expertise in crystallography. I would like to thank Dr. Omer Kabil for his help, suggestions and discussions in various aspects of my study. I would also like to thank members of Dr. Banerjee's lab for their suggestions and discussions. Additionally, I would like to thank my friends and family for their support.

## TABLE OF CONTENTS

## LIST OF TABLES

## LIST OF FIGURES

## ABBREVIATIONS

AdoMet S-adenosyl methionine

BSA bovine serum albumin

CBS Cystathionine β-synthase

CO Carbon monoxide

CSE γ-cystathionase

GSH Glutathione

GSSH glutathione persulfide

$H_2S$ hydrogen sulfide

MST mercaptopyruvate sulfur transferase

NO Nitric oxide

PDO persulfide dioxygenase

PLP Pyridoxal 5'-phosphate

PRF persulfide dioxygenase-rhodanese fusion

SQR sulfide quinone oxidoreductase

TPTZ 2,4,6-tripyridyl-S-triazine

## ABSTRACT

Hydrogen sulfide ($H_2S$) is the third eukaryotic gaseous signaling molecule that evokes a broad range of physiological effects. $H_2S$ levels are governed by the rates of both production and clearance. In eukaryotes, sulfide clearance occurs primarily *via* the mitochondrial sulfide oxidation pathway which consists of the enzymes sulfide: quinone oxidoreductase (SQR), persulfide dioxygenase (PDO), rhodanese and sulfite oxidase. Mutations in PDO result in ethylmalonic encephalopathy (EE), an autosomal recessive disorder. There are over 20 mutations described in patients with EE. Patients with EE and PDO knockout mice exhibit increased excretion of thiosulfate bringing into question the organization of the sulfur oxidation pathway.

Kinetic characterization of several EE patient mutations reported in human PDO: L55P, T136A, C161Y and R163W, was performed to determine the biochemical penalties incurred by these mutations. The variants displayed increasingly impacted $k_{cat}/K_m$ values of 18-, 42-, 65- and 200-fold lower $k_{cat}/K_m$ values for R163W, L55P, C161Y and T136A respectively. Similarly, T136A, R163W, C161Y and L55P displayed 1.4-, 3-, 11- and 10.5-fold lower iron content compared to wild-type PDO, respectively. The PDO mutants all display altered thermal stabilities with R16W, L55P, T136A and C161Y displaying 1.2-, 1.4-, 1.4- and 1.7-fold lower $T_m$ values compared to wild-type PDO.

Recently, bacterial proteins that are fusions between PDO and rhodanese have been identified. Existence of such a fusion suggests that their mitochondrial counterparts in higher organisms may interact and that characterization of such fusion proteins will facilitate the

modeling of interactions between human mitochondrial PDO and rhodanese and aid in elucidating the metabolic intermediates in the sulfide oxidation pathway. We have characterized a bacterial PDO/rhodanese fusion protein from *Burkholderia phytofirmans* which displays 1.8-fold higher PDO activity and 4.8-fold lower $K_m$ for GSSH as compared to human PDO, and rhodanese activity comparable to other bacterial rhodaneses. Additionally, the rhodanese domain catalyzed the formation of GSSH and sulfite from thiosulfate and glutathione, but no detectable sulfur transfer activity was observed for the reverse reaction. Similar observation were made for the stand-alone rhodanese domain; however, several fold increases in $V_{max}$ and $K_m$ values for thiosulfate and glutathione were observed for the various sulfur transfer reactions, suggesting that the PDO domain modulates the activity of the rhodanese domain. Combined, these results suggest that the fusion is poised to produce sulfite as its main product. To obtain structural insights into its mechanism, crystal structures of wild-type and the sulfurtransferase inactivating C314S mutation with and without GSH bound were determined at 1.8, 2.4, and 2.7 Å resolution, respectively. The structures revealed that the two active sites are distant and there is no evidence of direct communication between them. Bioinformatic analysis displays that this enzyme may be involved in sulfur assimilation pathways rather than an orthologous sulfide oxidation pathway.

# Chapter 1

## Introduction: Enzymology of Hydrogen Sulfide Turnover

The contents of this chapter have been published.

Citation:

N. Motl, P. K. Yadav, R. Banerjee. (2013) Enzymology of hydrogen sulfide turnover. in Hydrogen Sulfide and its Therapeutic Applications (Kimura, H. ed.), Springer pp 1-35.

### 1. 1 Introduction to Sulfide Metabolism

Long known as a toxic gas, sulfide like cyanide, targets cellular respiration by reversible inhibition of cytochrome c oxidase. The cell has therefore evolved strategies for handling the twin challenges of averting toxicity problems while exploiting the signaling potential of hydrogen sulfide ($H_2S$), which elicits profound physiological effects (1). Hence, a "safe" window must exist within which low intracellular concentrations of $H_2S$ are maintained and allowed to transiently spike to allow passage of a signal. The concentration width of this window could span three orders of magnitude since steady-state intracellular concentrations of $H_2S$ are estimated to be in the 15-30 nM range, (2,3) while mammalian mitochondrial ATP production is abolished at 50 μM $H_2S$ (4). The steady-state concentrations of $H_2S$ are a product of both the metabolic flux through the sulfide biogenesis and sulfide oxidation pathways (3) (Fig. 1.1). Three enzymes in the mammalian sulfur metabolic network catalyze $H_2S$ biogenesis (5,6). Two of these enzymes reside in the cytosolic transsulfuration pathway and are cystathionine β-synthase (CBS) and γ-

cystathionase (CSE). Both of these enzymes are versatile and catalyze $H_2S$ production in a variety of reactions starting from cysteine and/or homocysteine (7-9). The third enzyme, mercaptopyruvate sulfur transferase (MST) (10,11), is both cytosolic and mitochondrial in location and transfers the sulfur atom from mercaptopyruvate to an acceptor from where it can be subsequently released as $H_2S$. MST works in conjunction with the PLP-dependent enzyme, aspartate/cysteine aminotransferase (CAT), which catalyzes the conversion of cysteine to 3-mercaptopyruvate. Recently, D-amino acid oxidase has been reported to convert to D-cysteine to 3-mercaptopyruvate, providing an alternative supply route for the MST substrate, 3-mercaptopyruvate (12).

Sulfide catabolism occurs in the mitochondria and connects sulfur metabolism to the electron transfer chain, thereby linking sulfide oxidation to both ATP and reactive oxygen species production (Fig. 1.1). Half maximal inhibition of cytochrome *c* oxidase in cell extracts occurs at concentrations of ~0.3 µM versus ~20 µM $H_2S$ needed to inhibit cellular respiration in intact cells (4). To avoid intracellular sulfide build-up and consequent toxicity, the sulfide oxidation pathway is activated at considerably lower (~10-20 nM) sulfide concentrations (4). The high sensitivity of the sulfide oxidation pathway to $H_2S$, suggests that the duration of $H_2S$-based signaling is likely to be short (4). Sulfate and thiosulfate are the major products of the mammalian mitochondrial sulfide oxidation pathway, which comprises four enzymes: sulfide quinone oxidoreductase (SQR), a persulfide dioxygenase (PDO) that is the product of the *ethe1* gene, rhodanese, and sulfite oxidase (13). This chapter focuses on the structural enzymology and regulation of $H_2S$ metabolism.

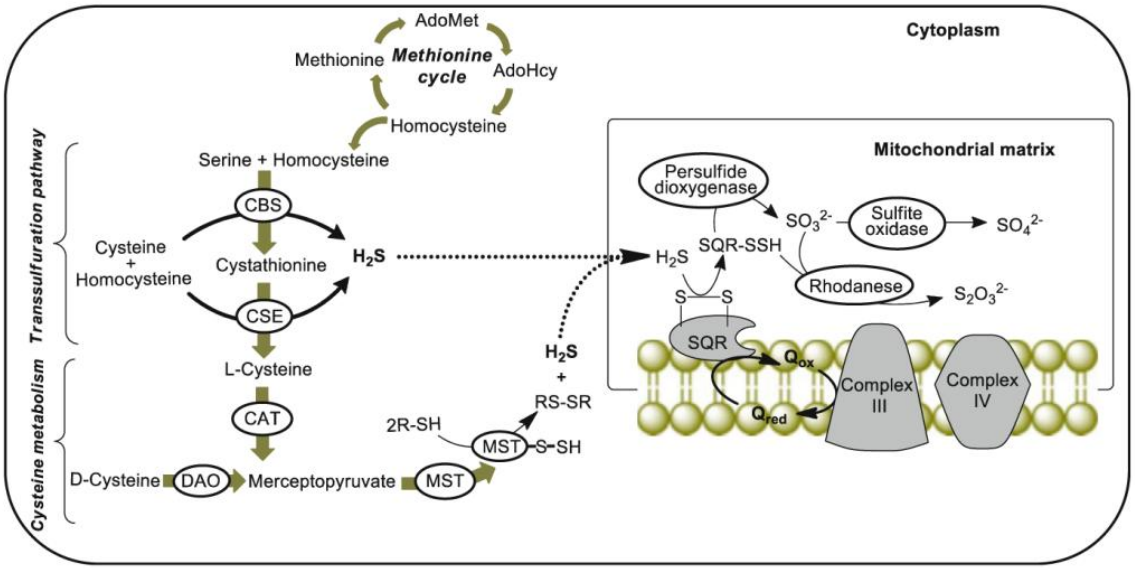


**Figure 1.1.** Scheme showing pathways of biogenesis and catabolism of $H_2S$. DAO is D-amino acid oxidase.

## 1.2 Enzymology of $H_2S$ Biogenesis

### 1.2.1 Cystathionine β-synthase

#### 1.2.1.1 Structural Organization of CBS

CBS is a multidomainal protein which, in its role in the transsulfuration pathway, catalyzes the condensation of homocysteine and serine to produce cystathionine (14). Homocysteine is a redox-active nonprotein amino acid that is produced by hydrolysis of S-adenosylhomocysteine, a product of S-adenosylmethionine (AdoMet)-dependent methylation reactions. Homocysteine is either recycled in the methionine cycle via the action of methionine synthase or committed to cysteine synthesis by the action of CBS (Fig. 1.1). Mutations in CBS are the most common cause of homocystinuria, an autosomal recessive disorder, characterized by severely elevated plasma homocysteine levels (15). CBS deficiency affects multiple organ systems including the ocular, skeletal, cardiovascular and the central nervous system (16).

In addition to the canonical transsulfuration reaction, CBS catalyzes $H_2S$-producing reactions in

which serine is substituted by cysteine (7,9). These reactions involve β-replacement of cysteine by homocysteine, cysteine or water to generate cystathionine, lanthionine or serine, respectively in addition to the common product, $H_2S$.

CBS is a homodimeric enzyme. The full-length human enzyme is prone to aggregation and exists in multiple oligomeric states ranging from 2-to 16-mers (17). The predominance of the 4-mer in the aggregated mixture has led to confusion in the literature about CBS being a homotetramer. Each monomer is organized into an N-terminal heme-binding domain, a central PLP-binding catalytic core and a C-terminal AdoMet-binding regulatory domain, which contains a tandem repeat of CBS domains. The latter, named after this protein, is found in all three domains of life and refers to a β−α−β−β−α secondary structure motif often associated with energy sensing that binds ATP or AMP (18)(19). In CBS, it binds the allosteric activator, AdoMet, which renders transsulfuration flux sensitive to cellular methyl donor status. Thus, when AdoMet levels are low, sulfur is spared and utilized via the methionine cycle to support AdoMet synthesis. In contrast, when AdoMet levels are plentiful, sulfur metabolism is directed towards cysteine synthesis via activation of CBS.

The crystal structures of full-length CBS from *Drosophila melanogaster* (dCBS, Fig. 1.2A) and a truncated variant of human CBS (hCBS) which lacks the C-terminal regulatory domain have been reported (19-21)(20-22). The N-terminal heme domain spans residues 1-70 in hCBS and 1-45 in dCBS while the middle PLP domain spans residues 71-411 in hCBS and 46-350 in dCBS. A 27 residue-long linker (351–377) visible in the structure of dCBS connects the PLP and C-terminal domains, which based on sequence alignment, is predicted to extend between residues 382-411 in hCBS.

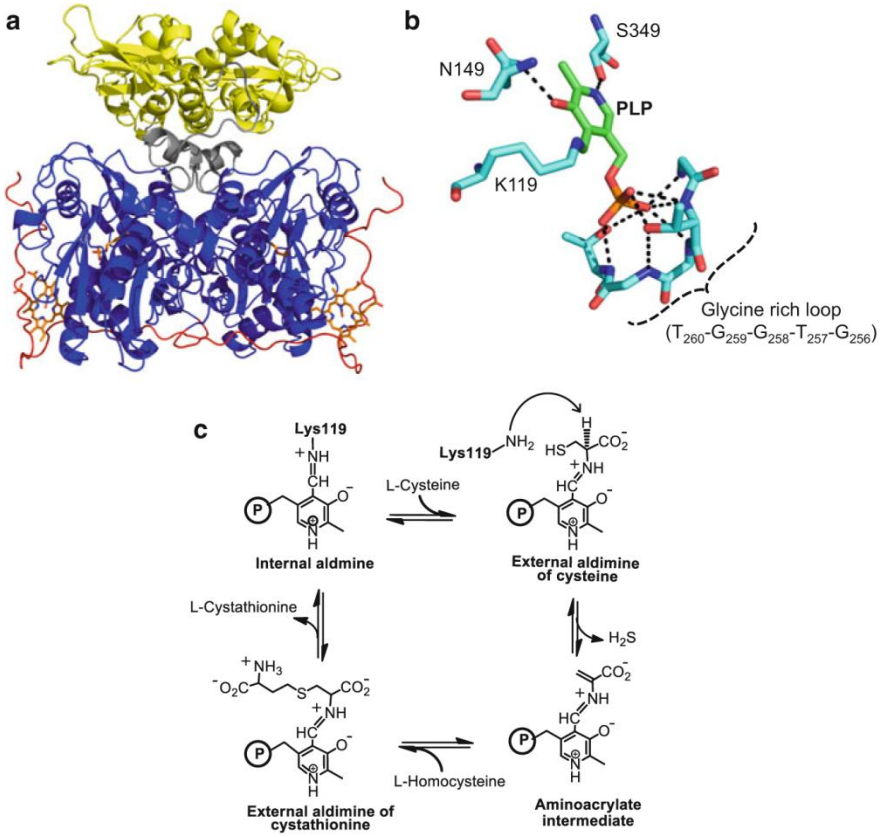


**Figure 1.2. Structure and catalytic mechanism of CBS**. (a) Structures of full-length dCBS. The protein comprises an N-terminal heme-binding domain (red), a PLP domain (blue) and a C-terminal AdoMet-binding domain (yellow). A linker (grey) connects the PLP-and C-terminal domains. (b) Close-up of the active site of hCBS. Hydrogen bonds between PLP and amino acids lining the active site are shown as dotted lines. Figs. 1.2a and b were generated using PDB files 3PC2 and 1M54, respectively. (c) Proposed catalytic mechanism for $H_2S$ generation from cysteine by CBS. The resting enzyme exists as an internal aldimine, which reacts with cysteine to form the external aldimine of cysteine. Elimination of $H_2S$ leads to formation of an aminoacrylate intermediate, which reacts with homocysteine (cysteine or water) to form the external aldimine of the product cystathionine (or lanthionine or serine). The catalytic cycle is completed upon release of product and reformation of the internal aldimine.

### 1.2.1.2 Catalytic Mechanism of CBS

The active site of CBS is lined with residues that position the substrates and cofactor for catalysis. PLP is covalently linked to an active site lysine (Lys119 in hCBS and Lys88 in dCBS) and its phosphate moiety is enveloped by a glycine-rich loop (Thr260- Gly259-Gly258-Thr257-Gly256, hCBS numbering) (Fig. 1.2B). Asn149 and Ser349 form hydrogen bonds with the

exocyclic oxygen and pyridine nitrogen, respectively (19,20). Replacement of the corresponding serine in yeast CBS (yCBS) by alanine results in the complete loss of activity, while replacement with aspartate results in ~80 fold lower activity despite the mutants having only two-fold lower PLP occupancy (22). Fluorescence and resonance Raman studies demonstrate that the PLP exists in two tautomeric forms: an active ketoenamine and an inactive enolimine (23-25). Asn149 helps stabilize the active ketoenamine tautomer. Perturbations in the active site hydrogen-bonding network can influence the tautomeric equilibrium, and, as described below is one mechanism by which the heme cofactor exerts its effects on the active site (23,25). The first step in the catalytic cycle (Fig. 1.2C) is the binding of serine or cysteine (Fig. 1.2C) to the active site followed by displacement of the lysine residue that forms an internal aldimine with PLP (14). Abstraction of the α-proton from the resulting external aldimine of serine/cysteine generates a carbanion intermediate. In the crystal structure of dCBS obtained at 1.7 Å resolution, the carbanion intermediate with serine was captured and revealed how the active site stabilizes this reactive species (21). The Cα atom is clearly $sp^2$ hybridized in this intermediate and the ε-amino group of Lys88 is within 2.1, 2.5 and 3.0 Å of the Cα, imino nitrogen of the Schiff base and C4A of PLP, respectively, where the negative charge is predominantly localized. Elimination of $H_2O$ or $H_2S$ from the external aldimine of serine or cysteine, respectively, leads to formation of the aminoacrylate intermediate, which was also captured in a crystal structure of dCBS obtained at 1.55 Å resolution (21). In this structure, the Cα is also clearly $sp^2$ hybridized and the ε-amino group of Lys88, which is swung away from Cα, is parked near the oxygen atoms of the phosphate moiety of PLP. The Cβ of the aminoacrylate intermediate is positioned for nucleophilic attack by the thiolate of homocysteine (to generate cystathionine), or cysteine (to generate lanthionine) or by water (to generate serine). The final step preceding product release

involves a second transchiffization reaction in which the active site lysine displaces the product and the enzyme returns to its resting internal aldimine state.

#### 1.2.1.3 Kinetics of $H_2S$ Generation by CBS

Detailed steady-state kinetic analyses of $H_2S$ generation by human and yeast CBS have been reported (9). In addition to the canonical β-replacement reaction in the transsulfuration pathway (Eq. 1.1), CBS catalyzes at least three other reactions with a combination of cysteine and homocysteine as substrates, leading to $H_2S$ production (Eqs. 1.2, 1.3, and 1.4). The CBS active site has two pockets for binding amino acids that are designated as sites 1 and 2.

$$\text{Serine} + \text{Homocysteine} \rightarrow \text{Cystathionine} + H_2O \quad [1.1]$$

$$\text{Cysteine} + \text{Homocysteine} \rightarrow \text{Cystathionine} + H_2S \quad [1.2]$$

$$\text{Cysteine} \rightarrow \text{Serine} + H_2S \quad [1.3]$$

$$\text{Cysteine} + \text{Cysteine} \rightarrow \text{Lanthionine} + H_2S \quad [1.4]$$

Site 1 binds the amino acid that forms the external aldimine with PLP while site 2, binds the nucleophilic amino acid (9). At saturating substrate concentrations, the specific activity for the β-replacement of cysteine by homocysteine (reaction 2) is ~4-fold higher than for the canonical β-replacement of serine by homocysteine (reaction 1). $H_2S$ generation from one (reaction 3) or two (reaction 4) moles of cysteine results in serine or lanthionine and is ~40-fold and ~20 fold lower, respectively than the rate of $H_2S$ generation from cysteine and homocysteine (9).

Within the cell, the efficiency of each CBS-catalyzed reaction is dictated in part by the relative concentrations of the individual substrates and the $K_m$ values are high for both yeast and human CBS relative to the intracellular concentrations of their amino acid substrates. The $K_m$ for cysteine for hCBS at site 1 is 6.8 ± 1.7 mM and higher still for site 2 (27.3 ± 3.7 mM). For yCBS, the $K_m$ values for cysteine at sites 1 and 2 are 3.6 ± 1.7 mM and 33 ± 3.7 mM,

respectively. Homocysteine only binds to site 2 and the $K_m$ s for yeast and human CBS are 0.13 ± 0.02 mM and 3.2 ± 1.3 mM, respectively (9). Simulations were performed using the steady-state kinetic data for hCBS at physiological concentrations of substrate (560 μM serine, 100 μM cysteine and 10 μM homocysteine). The simulations predicted that ~96% of $H_2S$ derived from hCBS is via β-replacement of cysteine by homocysteine with the remainder being contributed by the other two reactions (9,23).

Pre-steady state kinetic analysis and characterization of reaction intermediates was first reported for yCBS using stopped flow spectroscopy (26-28). The heme in hCBS interferes with enzyme-monitored pre-steady state kinetic analysis by masking the PLP absorbance. Kinetic analysis of a heme-less hCBS variant lacking the N-terminal heme domain was limited by its poor stability (29). To circumvent these limitations, we have employed difference UV-visible stopped-flow spectroscopy to characterize intermediates in the hCBS-catalyzed reaction (25), an approach, that we used previously to demonstrate the intermediacy of an aminoacrylate intermediate in dCBS (21). The rate of aminoacrylate formation is ~2.5-fold faster with serine than with cysteine in the reaction catalyzed by hCBS and product release appears to limit the overall reaction rate (25).

**1.2.1.4 Allosteric Regulation of CBS by Heme**

The N-terminal heme domain in CBS is devoid of any secondary structure. The heme is hexa-coordinate and its histidine and cysteine axial ligands were predicted by EPR, extended X-ray absorption fine structure (30)(32) and resonance Raman spectroscopy (31). The UV-visible spectrum of ferric CBS exhibits a Soret peak at 428 nm and a broad α/βabsorption band centered at 550 nm. In the ferrous state, the Soret peak shifts to 449 nm with concomitant sharpening of the αand βabsorption bands at 571 nm and 540 nm (32). Mutation of either heme ligand

diminishes hCBS activity (by ~9-fold) despite full PLP saturation in the C52A and C52S mutants and 75% saturation in the H65R mutant (33). On the other hand, heme saturation is greatly reduced in the heme ligand mutants (19% and 40% in the cysteine and histidine ligand mutants, respectively) compared to wild-type CBS. The C52S or C52A mutants have five-coordinate high-spin heme with a Soret peak blue-shifted from 428 to 415-417 nm in the ferric form and from 449 nm to 423 nm in the ferrous form (33). In the ferrous-CO state, the Soret peaks of the mutants (at ~422 nm) are virtually identical to that of wild-type enzyme, consistent with the substitution of the cysteine ligand by CO. The Soret peaks in the ferric, ferrous and ferrous-CO states in the H65R mutant are at 424, 421 and 420 nm, respectively, consistent with the presence of a low-spin heme (33).

While the role of the heme domain in CBS has been debated, there is growing evidence that it regulates CBS activity in response to changes in the heme spin-or ligation-state (34-36). The ferrous heme ligands CO and NO, inhibit CBS activity (34,37). Ferrous-NO CBS is five-coordinate with a broad Soret peak at ~390 nm (34). CBS exhibits nonequivalent binding sites for CO with $K_D$ values of 1.5 ± 0.1 μM and 68 ±14 μM for full-length hCBS and 3.9 ± 2 μM and 50 ± 8 μM for the C-terminal truncated form (39,40). Binding of NO to full-length CBS exhibits a $K_D$ of 30 ± 5 μM for NO (38). Binding of CO to full-length CBS inhibits enzyme activity with $K_i$ value of 5.6 ± 1.9 μM (37). The redox potential of the heme is −350 ± 4 mV (9) and -287 ± 2 mV (39) in full-length and truncated hCBS, respectively. This difference between the full-length and truncated forms suggests that the regulatory C-terminal domain modulates the heme redox potential. Despite the low reduction potential of the CBS heme, reversible regulation by CO can be achieved with physiologically relevant reductants (40). The diflavin oxidoreductases, human methionine synthase reductase and novel reductase 1, reduce ferric CBS and the ferrous-CO

species is formed in the presence of NADPH and CO.

Communication between the heme and PLP domains occurs via an α-helix whose N-terminal end leads in from the glycine rich loop harboring the conserved T257 and T260 residues that make contact with the phosphate moiety of PLP. At the C-terminal end of the helix, Arg266 is involved in a salt-bridge interaction with the heme ligand, Cys52. Changes in the heme coordination state e.g. by formation of the ferrous-CO species, is predicted to disrupt the salt bridge between Cys52 and Arg266, displacing the α-helix, which in turn is propagated to the PLP site shifting the tautomeric equilibrium towards the enolimine (24). Interestingly, replacement of Arg266 by methionine, a mutation described in homocystinuric patients, also results in the predominance of the inactive enolimine. Similarly, substitutions at Thr257 and Thr260 in the PLP domain stabilize the inactive enolimine tautomer leading to significant loss of CBS activity (41). Interestingly, these CBS mutations impact the $H_2S$ and cystathionine-producing versus $H_2O$ and cystathionine-producing reactions unequally, suggesting that that these two activities can be differentially regulated (41).

**1.2.1.5 Allosteric Regulation of CBS by AdoMet**

AdoMet binds to the C-terminal regulatory domain (42) and enhances CBS activity ~2-3 fold (43). Truncation of the C-terminal domain in hCBS leads to loss of AdoMet-dependent regulation, increases CBS activity and also decreases its propensity for aggregation (44). Hence, the regulatory domain exerts an autoinhibitory effect that is alleviated either upon AdoMet binding, by activating mutations or by deletion of the entire domain (45-47). The architecture of the regulatory domain and its juxtaposition relative to the catalytic domain was first visualized in the structure of full-length dCBS (Fig. 1.2A). The secondary structures the two CBS domains are slightly different: β-α-β-β-α-α-βfold in one (spanning residues 416-468 in hCBS) and α-β-α-β-β-

αin the second (residues 486-543). The AdoMet binding sites in CBS is predicted to reside in the β-sheet-lined cleft between the two CBS domains.

#### 1.2.1.6 Other Mechanisms for Regulation of CBS Activity

As a junction enzyme in sulfur metabolism, CBS is the locus of complex regulation. AdoMet is an allosteric regulator, which activates CBS under conditions of methyl group sufficiency (48,49). As noted above, gaseous signaling molecules like NO and CO bind to the heme in CBS and inhibits its activity (34,37,41,50,51), which is reversed upon air oxidation (40). Sumoylation of CBS decreases its activity (50). Lys211 in the catalytic core of human CBS appears to be the site of sumoylation. In addition, the C-terminal regulatory domain of CBS is needed for sumoylation. CBS is reportedly inhibited by lanthionine synthase C-like protein 1 (LanCL1) in the presence of glutathione (52). Under oxidative stress conditions, when oxidized glutathione levels rise, inhibition by LanCL1 is alleviated providing a mechanism for increasing transsulfuration flux and consequently, glutathione synthesis.

### 1.2.2 γ-Lyase Cystathionine (CSE)

#### 1.2.2.1 Structural Organization of CSE

Human CSE (hCSE) is a homotetrameric enzyme that catalyzes the second step in the transulfuration pathway cleaving cystathionine to cysteine, α-ketobutyrate, and ammonia (Fig. 1.3A). The crystal structures of yeast (yCSE) and hCSE are available at 2.6 Å resolution each (53,54). Each hCSE monomer comprises a large N-terminal PLP-binding domain (residues 1-263) and a smaller C-terminal domain (residues 264-401) (Fig. 1.3A). The yCSE monomer comprises three domains: an N-terminal domain, which interacts with the active site of a neighboring monomer, a middle catalytic domain and a small C-terminal domain. The yCSE catalytic and C-terminal domains are organized as in hCSE while the N-terminal extension

interacts with the active site of the neighboring subunit, is not present in hCSE and comprises an extended loop, an α-helix and a β-strand (53).

Mutations in CSE, inherited as an autosomal recessive disorder, results in cystathioninuria, which is often benign (55). Cystathioninuria can be secondarily associated with hepatoblastoma, neuroblastoma, poor development, cystic fibrosis and Down's syndrome.

**1.2.2.2 Catalytic Mechanism of CSE**

Like CBS, CSE also catalyze various reactions leading to $H_2S$ biogenesis in addition to catalyzing the canonical reaction in the transsulfuration pathway (8,23). TPLP is covalently linked to Lys212 in hCSE via a Schiff base and its mutation to alanine reduces $H_2S$ production ~80-fold compared to wild-type enzyme. Several active site residues are engaged in hydrogen bonding interactions with PLP (53,54); Asn187 with the pyridine nitrogen and Gly90, Leu91, Ser209 and Thr211 from one subunit and Tyr60 and Arg62 from an adjacent subunit with the phosphate moiety (Fig. 1.3B). Replacement of Asn187 with alanine or glutamic acid results in complete loss of $H_2S$ production while substitutions of Ser209 and Thr211 by alanine result in a modest ~1.5 fold decrease in $H_2S$ production (56). Interactions between Tyr60 and Arg62 contributed by the N-terminal domain of a neighboring monomer and the phosphate group of PLP helps to stabilize the active site, which is located at the interface between adjacent subunits. Multiple sequence alignment of human, yeast, mouse, rat and slime mold CSEs reveals that Tyr60 and Arg62 are conserved in all five sequences (56). Substitution of Tyr60 with threonine or alanine results in an ~5-8 fold decrease in hCSE activity, while replacement of Arg62 with alanine or lysine results in an ~10-36 fold decrease in activity (56).

CSE belongs to the γ-family of PLP-dependent enzymes, which catalyze elimination reactions at the γ-carbon. However, in the case of CSE, the specificity is not high and the enzyme

catalyzes reactions at both the β-and γ-carbons of the substrate. In the first step, the substrate (i.e. cystathionine or cysteine) forms a Schiffs base with the PLP via a transaldimination reaction, freeing the active site Lys212 residue. In the next step, Lys212 presumably acts as the general base and abstracts the α-proton from bound substrate. When cystathionine is the substrate, cleavage of the C-γ-S bond is promoted by a second proton abstraction from Cβ resulting in the subsequent elimination of cysteine. Hydrolysis of the resulting imine intermediate yields α-ketobutyrate and ammonia. Alternatively, when cysteine is the substrate, the C-β-S bond is cleaved, releasing $H_2S$ (Fig. 1.3C). A second transaldimination reaction regenerates the resting internal aldimine. UV-visible spectroscopy based pre-steady state kinetic analysis of the reaction catalyzed by yCSE suggests that product release constitutes the rate-limiting step (57).

The specificity of the hCSE-catalyzed α,γ-elimination versus α,β-elimination is proposed to be governed by the hydrophobicity of the residue at position 339 (53,56). This hypothesis was tested by replacing Glu339 with lysine, alanine and tyrosine, which increases hydrophobicity in the following order: Y>A>K>E. E339K, E339A and E339Y show approximately 1.8-, 3.2- and 7.2-fold increase, respectively in the catalytic efficiency of $H_2S$ production from cysteine as compared to wild-type enzyme (56), consistent with the view that enhancing the hydrophobicity of the residue at position 339 in hCSE favors the α,β-elimination reaction.

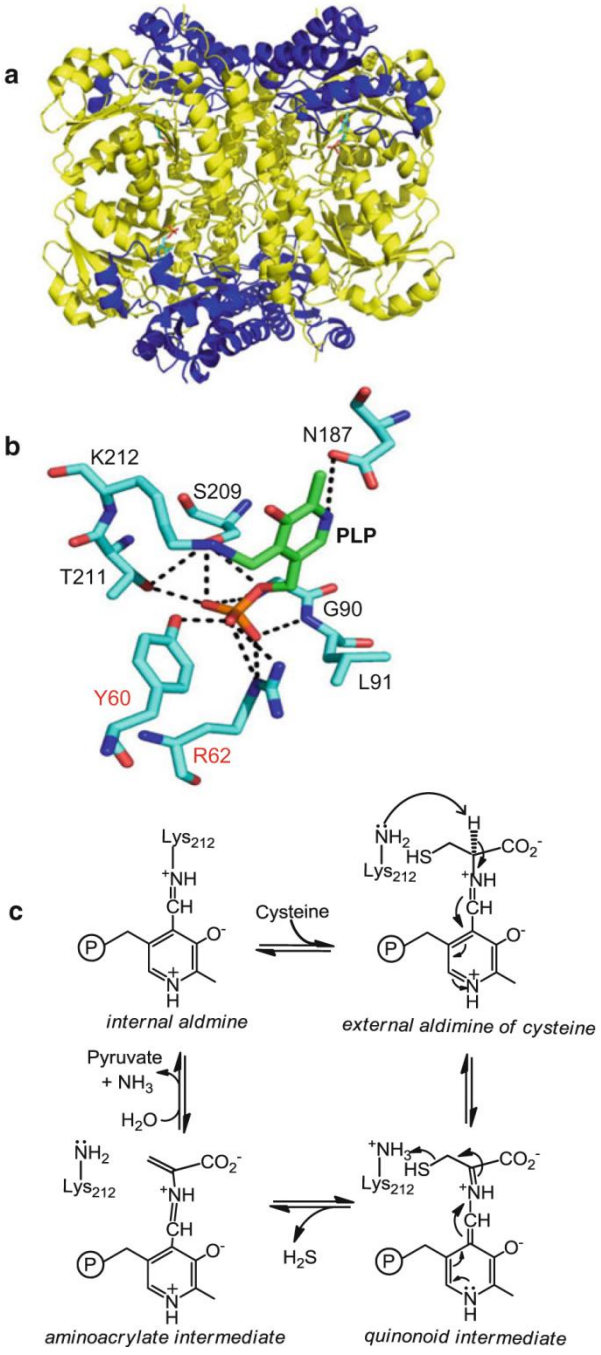


**Figure 1.3. Structure and catalytic mechanism of CSE.** (a) Structures of tetrameric hCSE comprising an N-terminal catalytic domain (red) and a C-terminal domain (blue). PLP is shown in stick representation (cyan). (b) Close-up of the active site of hCSE. Hydrogen bonds between PLP and amino acids lining the active site are shown as dotted lines. The red labels denote residues contributed by a neighboring subunit. Figs 1.3a and b were generated using PDB file 2NMP. (c) Proposed catalytic mechanism of CSE for $H_2S$ generation. Cysteine reacts with the

resting enzyme and forms the external aldimine of cysteine. Abstraction of the α-proton from cysteine leads to formation of cysteine-ketamine intermediate. Cleavage of the C–β–S bond eliminates $H_2S$ and leads to formation of the aminoacrylate intermediate, which undergoes hydrolysis to give pyruvate and ammonia. In the final step, free PLP rebinds with the Lys212 to regenerate the resting internal aldimine.

### 1.2.2.3 Kinetics of $H_2S$ generation by CSE

Detailed steady-state kinetic analysis of hCSE revealed that in addition to the canonical cystathionine cleavage reaction in the transsulfuration pathway (Eq. 1.5), the enzyme can catalyze five distinct $H_2S$-generating reactions in the presence of cysteine and/or homocysteine (Eqs. 1.6-1.10) (8).

L-Cystathionine + $H_2O$ →L-Cysteine + α-Ketobutyrate + $NH_3$ [1.5]

L-Cysteine + $H_2O$ → L-Pyruvate + $NH_3$ + $H_2S$ [1.6]

L-Cysteine + L-Cysteine →L-Lanthionine + $H_2S$ [1.7]

L-Homocysteine + $H_2O$ →L-Homoserine + $H_2S$ [1.8]

L-Homocysteine + L-Homocysteine → L-Homolanthionine + $H_2S$ [1.9]

L-Homocysteine + Cysteine → L-cystathionine + $H_2S$ [1.10]

Unlike hCSE (8), rat CSE reportedly utilizes cystine, the oxidized disulfide form of cysteine, as a substrate for $H_2S$ production (58). However, the availability of cystine in the reducing cellular milieu is questionable and the immediate product of the reaction is cysteine persulfide, which is highly unstable. Under maximal velocity conditions, the highest rate of $H_2S$ production is observed for reaction 9, i.e. γ-replacement of homocysteine by a second mole of homocysteine while the lowest rate is observed for reaction 6, i.e. α,β−elimination of cysteine (8). At physiological substrate concentrations, the highest rate of $H_2S$ production is predicted to occur via the α,β−elimination reaction of cysteine and the lowest rate from the β−replacement of cysteine by a second mole of cysteine (Eq. 1.7).

CSE exhibits two substrate-binding sites: site 1 at which the Schiff base is formed between PLP and an amino acid and site 2 where the nucleophilic second amino acid binds. The $K_m$ for cysteine at site 1 (1.7 ± 0.7mM) is ~1.6-fold lower than for homocysteine (2.7 ± 0.8 mM) while for the $K_m$ for homocysteine at site 2 (5.9 ± 1.2 mM) is ~6-fold lower than for cysteine (33 ± 8 mM). The lower $K_m$ for cysteine versus homocysteine at site 1 together with the higher cellular concentration of cysteine (~100 µM) versus homocysteine (<10 µM), explains the predominance of reaction 6 versus 9 at physiologically relevant substrate concentrations (8).

The relative contributions of the various CSE-catalyzed $H_2S$ producing reactions has been estimated at physiologically relevant substrate concentrations (5 µM cystathionine, 100 µM cysteine and 10 µM homocysteine) and low (10 µM), moderate (40 µM) and severe (100 µM) hyperhomocysteinemia (8). Simulations predict that under normal and hyperhomocysteinemic conditions, ~87-99.5% of the total $H_2S$ is derived via α,β-elimination of cysteine and α,γ-elimination of homocysteine, while the remaining three reactions collectively contribute very little. Between the two major $H_2S$ contributing reactions, the α,β-elimination of cysteine predominates (~71%) at normal homocysteine concentrations while the α,γ-elimination of homocysteine is the major $H_2S$ producer accounting for ~61% and ~78% $H_2S$, respectively under moderate and severe hyperhomocysteinemic conditions (8).

Preliminary pre-steady state kinetic analyses of the yCSE-catalyzed reaction were performed at 5 and 30 °C (59). An aminocrotonate intermediate was detected ($\lambda_{max}$ = 480 nm) upon rapid mixing of yCSE with cystathionine but not with L-cysteine. Conversion of the aminocrotonate intermediate to products represents the rate-limiting step in the CSE-catalyzed cleavage of cystathionine (57).

**1.2.2.4 Regulation of CSE**

Unlike CBS, mechanisms for regulating CSE activity are not well understood. $H_2S$ formation by CSE was reported to be upregulated by calmodulin in the presence of 2 mM $Ca^{2+}$ (59) However, $Ca^{2+}$ /calmodulin-dependent regulation of purified hCSE has not been observed in our laboratory (Chiku and Banerjee, unpublished results). A recent study on rat CSE (60), reports the rate of $H_2S$ production was low in the presence of 2 mM cysteine and 0-100 nM $Ca^{2+}$ and increased 5-fold when 50 μM PLP was added to the reaction mixture. At higher $Ca^{2+}$ concentrations (0.3 -3.0 μM), the rate of $H_2S$ production was ~2.5-fold higher in the presence or absence of PLP. Calmodulin (1 μM) had no effect on $H_2S$ production by CSE. These findings suggest that CSE is not regulated by calmodulin and that low $Ca^{2+}$ enhances $H_2S$ production but only in the presence of exogenous PLP while high $Ca^{2+}$ concentrations (300 nM to 3 μM) inhibit CSE (60). While CSE can be sumoylated in vitro (50), the physiological relevance of this modification is not known. Mammalian CSE has two conserved CXXC motifs. However, their involvement in redox-dependent regulation of CSE activity is not known.

### 1.2.3 Mercaptopyruvate Sulfurtransferase

#### 1.2.3.1 Structural Organization of MST

MST functions on a catabolic arm of cysteine metabolism and acts downstream of CAT to produce $H_2S$ (58,61). CAT or aspartate aminotransferase, can use cysteine as a substrate to produce 3-mercaptopyruvate in the presence of alpha-ketoglutarate. 3-Mercaptopyruvate is a substrate for MST, which transfers the sulfur group to a catalytic cysteine residue forming an enzyme-bound persulfide and releasing pyruvate. In the second half reaction, the sulfane sulfur is transferred to a thiol acceptor e.g. cysteine, homocysteine, dihydrolipoic acid, GSH or thioredoxin and subsequently released as $H_2S$ (62-64). The MST-bound persulfide can also be transferred to non-thiol acceptors like KCN to form thiocyanate (65). Recently an alternative to

the transamination pathway has been reported for the production of 3-mercaptopyruvate from D-cysteine in a reaction catalyzed by D-amino acid oxidase (12). The latter, is expressed in multiple tissues and is most abundant in the cerebellum and kidney (12). Defects in the MST gene are inherited as an autosomal recessive disorder known as mercaptolactate-cysteine disulfiduria (66). The condition is characterized by excessive excretion of mercaptolactate-cysteine disulfide in the urine, with or without mental retardation. Mercaptopyruvate is oxidized by lactate dehydrogenase to mercaptolactate and reacts subsequent to export, with extracellular cysteine to form the mixed disulfide of mercaptolactate and cysteine (67).

The crystal structures of MST from *E. coli* and *Leishmania major* have been solved at 2.8 Å and 2.1 Å resolution, respectively (68,69). Recently, our laboratory has obtained the structure of the product complex of hMST at 2.15 Å resolution with pyruvate and persulfide bound at the active site (64). Both bacterial and human MST are comprised of two domains connected by a linker, which are structurally similar to the rhodanese domain (Fig. 1.4A). The *Leishmania* MST has an extra ~80 amino acids long domain that shares structural homology with the immunosuppressant FK506-binding protein and to macrophage infectivity potentiator protein, both of which exhibit peptidyl prolyl cis-trans isomerase activity (68). Expression of a C-terminally truncated *Leishmania* MST yields a misfolded protein devoid of catalytic activity (70). The C-terminal domain in the *L. major* MST is postulated to be involved in protein folding and protein–protein interactions (68).

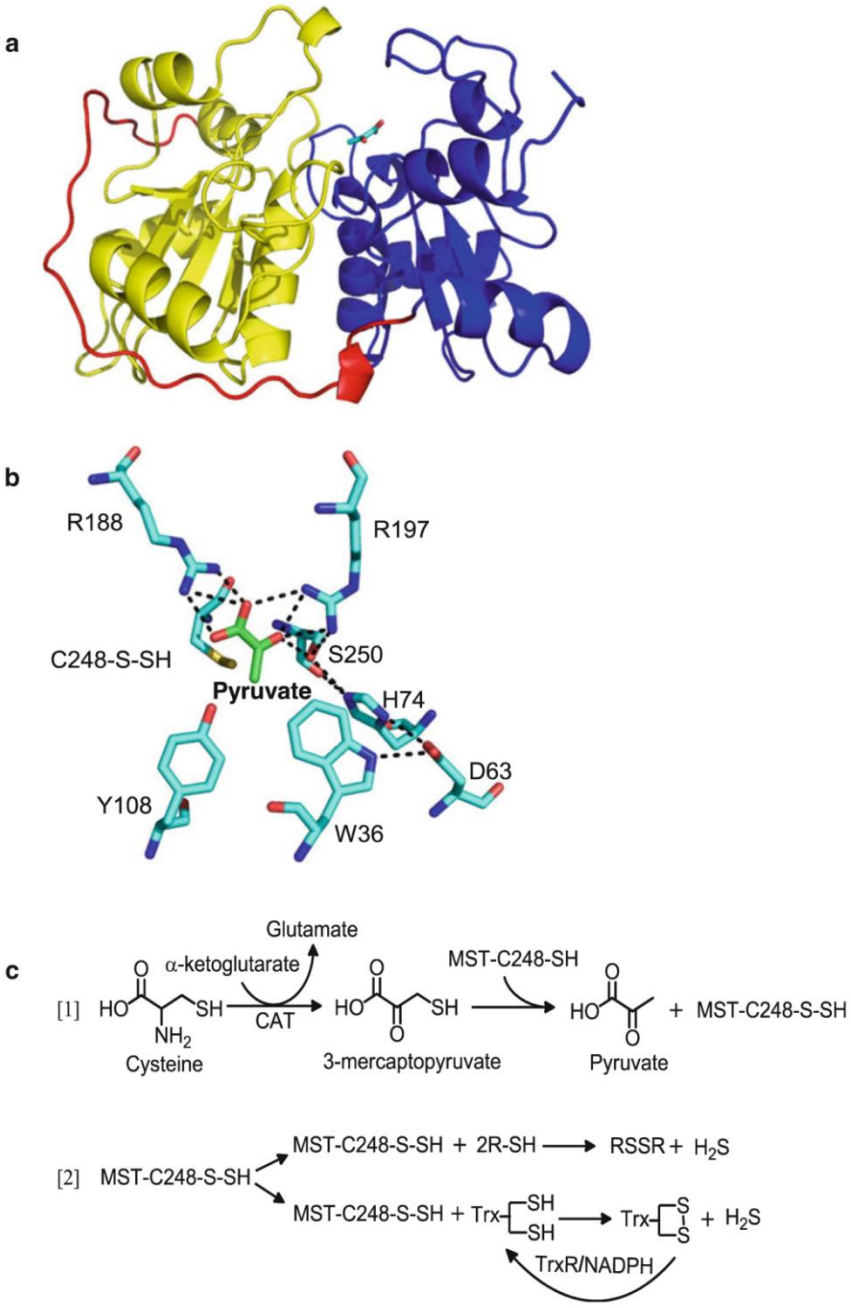


**Figure 1.4. Structure and catalytic mechanism of MST.** (a) Structure of human MST, which comprises an N-terminal domain (yellow) connected to the catalytic domain (blue) by a linker (red). (b) Close-up of the active site of hMST showing a persulfide on Cys248 and pyruvate (hydrogen bonds are represented by dotted lines). Figs. 1.4a and b were generated using PDB file 4JGT. (c) Reaction scheme for CAT/MST-dependent $H_2S$ generation. (1) CAT catalyzes the transamination between cysteine and α-ketoglutarate to generate mercaptopyruvate and glutamate. (2) MST catalyzes the sulfur transfer from mercaptopyruvate to an active site cysteine, giving pyruvate and MST-bound persulfide. The latter reacts with thiols or thioredoxin (in the presence of NADPH and thioredoxin reductase) to generate $H_2S$.

### 1.2.3.2 Catalytic Mechanism of MST

A conserved cysteine residue (Cys248 in hMST) plays a key role in the catalytic mechanism of this enzyme (Fig. 1.4B). All three available MST structures exhibit persulfides at the active site cysteine residue, which represents the product of the MST-catalyzed sulfur transfer from 3-mercaptopyruvate. Substitution of the corresponding active site cysteine with serine in rat MST (rMST), results in complete loss of activity (71). Two conserved arginine residues (Arg188 and Arg197 in hMST) (Fig. 1.4B) are proposed to be important for proper positioning of the substrate and their replacement with glycine is deleterious for rMST activity. The R187G and R196G mutations increase $K_m$ for 3-mercaptopyruvate by 10-and 60-fold, respectively and decrease $k_{cat}$ 4-and 870-fold, respectively. Based on the *Leshmania* MST crystal structure, a serine protease-like catalytic triad, comprising Ser255-His75-Asp61 was predicted to be a common feature of the MST family. The catalytic triad is proposed to play a role in polarizing the carbonyl bond in the substrate to assist in the nucleophilic attack by the active site cysteine (68). The crystal structure of hMST confirms the presence of a serine protease-like catalytic triad (Ser250-His74-Asp63) in the active site (64).

Enzymes belonging to the sulfurtransferase family catalyze the transfer of a sulfur atom from a sulfur donor to a nucleophilic acceptor. Based on steady-state kinetic analysis of bovine MST, the enzyme was proposed to use a sequential mechanism (72). Based on the structure of hMST containing a mixture of the product complex (Cys248-SSH and pyruvate) and an unproductive intermediate (3-mercaptopyruvate in a disulfide linkage with Cys248), we have proposed a detailed reaction mechanism (Fig. 1.4C) (64). The conserved arginine residues, Arg188 and Arg197, interact via hydrogen bonds with the carboxyl group of mercaptopyruvate while Arg197 also hydrogen bonds with the carbonyl group of the substrate. His74 in the

catalytic triad is proposed to function as a general base, abstracting a proton from Ser250, which in turn deprotonates Cys248 for subsequent attack on the sulfur of 3-mercaptopyruvate, leading to transfer of the sulfur atom to form Cys248-persulfide and pyruvate. Following release of pyruvate, an acceptor molecule (e.g. a dithiol or thioredoxin) attacks the sulfane sulfur of the cysteine of the cysteine persulfide regenerating MST and forming a new persulfide on the acceptor. Nucleophilic attack by the second (or resolving cysteine) on the acceptor releases $H_2S$ and results in oxidized disulfide product. Sulfur transfer from mercaptopyruvate to cyanide generates thiocyanate and pyruvate (65).

Dihydrolipic acid, thioredoxin, cysteine, homocysteine and glutathione function as acceptors in the in vitro MST assay and a detailed steady state kinetics analysis of $H_2S$ production by MST in the presence of these acceptors has been reported (64). At pH 7.4 and 37 °C kinetic studies revealed that hMST exhibits the highest $k_{cat}/K_m$ values are obtained in the presence of human thioredoxin (3,200 $M^{-1}s^{-1}$) and dihydrolipoic acid (390 $M^{-1}s^{-1}$), while the lowest value (12.0 $M^{-1}s^{-1}$) was obtained with glutathione. Based on kinetic simulation at physiologically relevant concentrations of acceptors, thioredoxin is predicted to couple most efficiently to the MST reaction (64).

**1.2.3.2 Regulation of MST**

Regulation of the MST/CAT is poorly understood. $Ca^{2+}$ -dependent regulation of MST has been reported based on the effect of varying $Ca^{2+}$ concentrations on MST/CAT-dependent $H_2S$ production in mouse retinal lysate (73). $H_2S$ production decreased as $Ca^{2+}$ concentration increased (0-2.9 μM) in the presence of cysteine and α-ketoglutarate (substrates for the CAT/MST pathway) but not when 3-mercaptopyruvate was used, suggesting that $Ca^{2+}$ regulates CAT (73). Calmodulin is not involved in regulation of MST/CAT-dependent $H_2S$ production

(73). Rat MST has five cysteines and appears to be redox regulated. Of the five cysteines, three (i.e. Cys154, Cys247 & Cys263) are surface exposed (74,75). An intersubunit disulfide bond forms between Cys154 and Cys263 under oxidizing conditions and can be reduced by thioredoxin. Thioredoxin-reduced MST is ~4.6-fold more active than the oxidized form of MST, while pretreatment of MST with DTT results in lower activation (~2.3-fold) (62). Human MST is a monomer and the cysteine residues that form the intersubunit disulfide in rMST are not conserved in hMST (64). The active site cysteine (i.e. Cys247 in rMST) acts as another redox-sensitive switch with the potential to regulate MST (74). Treatment of rMST with stoichiometric oxidants ($H_2O_2$ or tetrathionate) results in inhibition due to formation of cysteine sulfenate at the active site, which can be reversed by reductants such as DTT or thioredoxin (74).

### 1.2.4. The Relative Contributions of CBS, CSE and MST to $H_2S$ Production

It is not readily possible from the available kinetic data collected under varied buffer, pH and temperature conditions, to assess the relative roles of CBS, CSE and MST to $H_2S$ production in different tissues. As a first step towards addressing this question, our laboratory has initiated kinetic studies in a limited set of tissues (murine liver, kidney and brain) at pH 7.4 and at 37 °C (3,76). A second key piece of information that is needed to evaluate the contributions of the individual enzymes, is their concentrations in a given tissue, which can be estimated using semi-quantitative Western blot analysis (76). Finally, it is essential that sensitive and reliable methods for $H_2S$ detection be used to monitor its formation at physiologically relevant substrate concentrations. Initial studies in our laboratory evaluating total $H_2S$ production in murine tissues indicated that in the presence of 100 µM cysteine, liver exhibits the highest rate of $H_2S$ production (484 ± 271 µmole $h^{-1}$ $kg^{-1}$ tissue) followed by kidney (104 ± 44 µmole $h^{-1}$ $kg^{-1}$ tissue at 0.5 mM cysteine) and then brain (29 ± 7 µmole $h^{-1}$ $kg^{-1}$ tissue) (76). Semi-quantitative

Western blot analyses suggest that the expression level of all three $H_2S$-producing enzymes decreases in the following order: liver>kidney>brain ((76) and Yadav & Banerjee, unpublished results).

The relative contributions of CBS and CSE to $H_2S$ production at physiologically relevant substrates concentrations (560 μM serine, 100 μM cysteine and varying homocysteine ranging from its normal concentration (10 μM), to those seen under mild (40 μM) and severe (200 μM) hyperhomocysteinemia conditions) have been assessed. The kinetic simulations predict that CSE is the major $H_2S$ producer and accounts for 97% of the $H_2S$ production in liver at 10 μM homocysteine, with the proportion only increasing under hyperhomocysteinemic conditions (76). A comparable analysis including the contribution of MST is needed to provide a more complete picture of the quantitative significance of CBS, CSE and MST to $H_2S$ production in different tissues. To assess the contribution of the MST/CAT pathway to cysteine-derived $H_2S$ production, the assays need to be conducted in the presence of physiological concentrations of α-ketoglutarate needed by CAT to convert cysteine to 3-mercaptopyruvate.

### 1.3. Enzymology of $H_2S$ Oxidation

#### 1.3.1. Microbial strategies for sulfide oxidation

A major reaction of the global sulfur cycle is the oxidation of $H_2S$ to sulfate. It is instructive to examine the variations in sulfide oxidation strategies used by microbes where the pathways are much better understood than in man. In microbes, inorganic sulfur compounds such as sulfide, sulfur globules, sulfite, thiosulfate and polythionates are oxidized to sulfate for generation of ATP.

##### 1.3.1.1 Sulfide and thiosulfate oxidation by phototrophic bacteria

Green and purple sulfur bacteria utilize both sulfide and thiosulfate as electron donors for

photoautotrophic growth (77,78). Oxidation occurs in a stepwise manner with sulfide being converted initially to elemental sulfur, which is stored as sulfur globules either in the periplasm or on the surface of the outer membrane and utilized when sulfide is limiting. The two major enzymes directly involved in sulfide oxidation are SQR (Eq. 1.11) and flavocytochrome c sulfide dehydrogenase (Eq. 1.12), a heterodimeric flavoprotein comprising a glutathione reductase-like subunit containing an FAD cofactor and a redox-active disulfide and a diheme cyctochrome c subunit (79). Flavocytochrome c sulfide dehydrogenase exists in both soluble and membrane bound forms and, like SQR, catalyzes the oxidation of sulfide to polysulfide while reducing the diheme cytochrome via FAD (79).

$$S^{2-} + \text{Ubiquinone}_{ox} \rightarrow S^0 + \text{Ubiquinone}_{red} \qquad [1.11]$$

$$S^{2-} + \text{cyt } c_{ox} \rightarrow S^0 + \text{cyt } c_{red} \qquad [1.12]$$

Sulfur globules are converted to sulfite via the cytoplasmic dissimilatory sulfite reductase pathway (80). The proteins common to bacteria harboring the dissimilatory sulfite reductase pathway include a siroheme or siroamide-containing sulfite reductase, a transmembrane electron transporting protein complex, a putative siroheme amidase and the product of the *dsr*C gene. In addition, a sulfurtransferase complex and an iron-sulfur cluster-containing NADH oxidoreductase, which is proposed to reduce sulfur polysulfides, are also present in some bacteria. The transmembrane complex shuttles electrons released during oxidation of $H_2S$ to sulfite to quinones (77,80). Sulfite is toxic and is further oxidized to sulfate by one of two pathways. The first is direct oxidation catalyzed by sulfite oxidase (Eq. 1.13) and the second involves oxidation of sulfite to adenosine-5´-phosphosulfate and its subsequent conversion to sulfate liberating either ADP or ATP as the co-product (Eqs. 1.14 and 1.15) (81).

$$SO_3^{2-} + H_2O \rightarrow SO_4^{2-} + 2e^- + 2H^+ \qquad [1.13]$$

$SO_3^{2-} + AMP \rightarrow APS + 2e^-$ [1.14]

$APS + PPi \text{ (or Pi)} \rightarrow SO_4^{2-} + ATP \text{ (or ADP)}$ [1.15]

Thiosulfate is oxidized to sulfate by the multi-enzyme sulfur oxidizing (Sox) system (Eq. 1.16). The Sox system is widely distributed among phototrophic and sulfur oxidizing bacteria

$S_2O_3^{2-} + 5H_2O \rightarrow 2SO_4^{2-} + 8e^- + 10H^+$ [1.16]

and is also present in some green and purple bacteria (77,78,82). It is localized in the periplasm and comprises four proteins: SoxAX, SoxYZ, SoxB and SoxCD. In the first step, thiosulfate is oxidized to a cysteinyl S-thiosulfonate intermediate bound to SoxY, which is then hydrolyzed to sulfate by a dimanganese thiosulfohydrolase, SoxB. The remaining protein-bound sulfane sulfur is oxidized to sulfate by SoxCD, a heterotetramer with a molybdenum cofactor-containing subunit and a diheme cytochrome c-containing subunit. Electrons released during thiosulfate oxidation are transferred to cytochromes and from there, to the electron transport chain. Green and purple sulfur bacteria do not have a SoxCD component in their Sox system, and are unable to completely oxidize thiosulfate using the Sox system (77,78,83). In these bacteria, the remaining sulfane sulfur in the SoxYZ complex is proposed to either be transferred to the bacterial sulfur globule pool or, to be oxidized by the dissimilatory sulfite reductase pathway to sulfite.

#### 1.3.1.2 Sulfur oxidation by acidophilic bacteria

Acidophilic bacteria such as *Acidithiobacillus ferrooxidans* and *Acidithiobacillus thiooxidans*, utilize a sulfur dioxygenase to oxidize elemental sulfur to sulfite (Eq. 1.17) (84). Thiol-containing proteins are predicted to be involved in mobilization of extracellular octameric elemental sulfur and presentation of sulfane sulfur to the periplasmic sulfur dioxygenase, which

$1/8S_8 + O_2 + H_2O \rightarrow SO_3^{2-} + 2H^+$ [1.17]

does not accept sulfide or elemental sulfur as substrate (84). The product of this reaction, sulfite is oxidized to sulfate by sulfite oxidase. Two other enzymes, SQR and thiosulfate quinone oxidoreductase are also active in sulfur oxidation in acidophilic bacteria. SQR oxidizes sulfide to elemental sulfur which can react abiotically with sulfite to produce thiosulfate (84). Thiosulfate can be oxidized to tetrathionate by thiosulfate quinone oxidoreductase with the electrons being transferred to quinone.

**1.3.1.3 Sulfur oxidation by Archaea**

Sulfur-oxidizing Achaea use a variation of the oxidation schemes discussed above. Thus, in *Acidianus ambivalens,* sulfur oxidation is initiated by sulfur oxygenase reductase, a non-heme iron protein that catalyzes the disproportionation of elemental sulfur and/or polysulfide to sulfide and sulfite (85-87). $H_2S$ is oxidized by SQR to elemental sulfur, which can be utilized by sulfur oxygenase reductase setting up an energy-yielding cycle between the two enzymes and allowing the organism to maximize the energy gained from sulfur compounds (88). Sulfite can be further oxidized to sulfate by sulfite oxidase (86) or it can react with elemental sulfur to form thiosulfate, which is oxidized to tetrathionate. Alternatively, sulfite can be oxidized to sulfate via the APS pathway (89).

In the next section, we review the literature on the mitochondrial sulfide oxidation pathway focusing on the enzymes, SQR, the persulfide dioxygenase (PDO) and rhodanese. The conversion of sulfide to sulfite and thiosulfate by this trio of enzymes most closely resembles the components of the sulfide oxidation pathway in acidophilic bacteria with the exception that polysulfide is not generated as an intermediate in the mammalian pathway. Instead, as discussed below, the persulfide product of SQR is transferred to an as yet unidentified acceptor. Sulfite is ultimately oxidized to sulfate by sulfite oxidase in mammals.

### 1.3.2 Sulfide Quinone Oxidoreductase (SQR)

#### 1.3.2.1 Structural organization of SQR

SQR is found in the inner mitochondrial membrane (90) in eukaryotes, which are believed to have acquired the nuclear encoded gene from a mitochondrial endosymbiont (90). SQR exists as a dimer or a trimer, with one FAD and one redox active disulfide in each monomer (91). SQR oxidizes sulfide to a protein-bound persulfide and transfers electrons from $H_2S$ to ubiquinone via a bound FAD, coupling sulfide oxidation to the electron transport chain (Fig. 1.1). Hence, sulfide functions as an inorganic substrate for the ATP-generating electron transfer chain (4).

Several crystal structures of SQRs have been reported, notably from *Acidianus ambivalens* (88), *Aquifex aeolicus* (92), and *Acidithiobacillus ferrooxidans* (93) SQR belongs to the family of flavin disulfide reductases that includes glutathione reductase. SQR contains two Rossman fold domains and a C-terminal domain that is important for membrane binding (Fig. 1.5A). The FAD cofactor is found in the first N-terminal Rossman fold domain and can be non-covalently or covalently bound. In the latter case, a thioether linkage exists between a cysteine or a cysteine persulfide and the 8-methylene group of the isoalloxazine ring of FAD (92). The catalytic disulfide is located on the *re* face of the FAD (Fig. 1.5B). A conserved glutamate residue in the active site is proposed to serve as a general base for deprotonating $H_2S$ (93). The ubiquinone-binding site is located on the *si* face of the FAD and the majority of residues in contact with the quinone are hydrophobic including Phe41, Pro43, Gly322, Tyr323, Gln353, Tyr411, Phe394 and Phe357 (*A. ferrooxidans* numbering) (93). The aromatic ring of the quinone is sandwiched between the benzene rings of Phe394 and Phe357. The O2 atom of the flavin electron donor, and the O4 atom of the quinone acceptor are <3 Å apart. Residues Tyr411 and

Lys391 have been proposed to transfer protons from water for protonation of the reduced quinone (92,93).

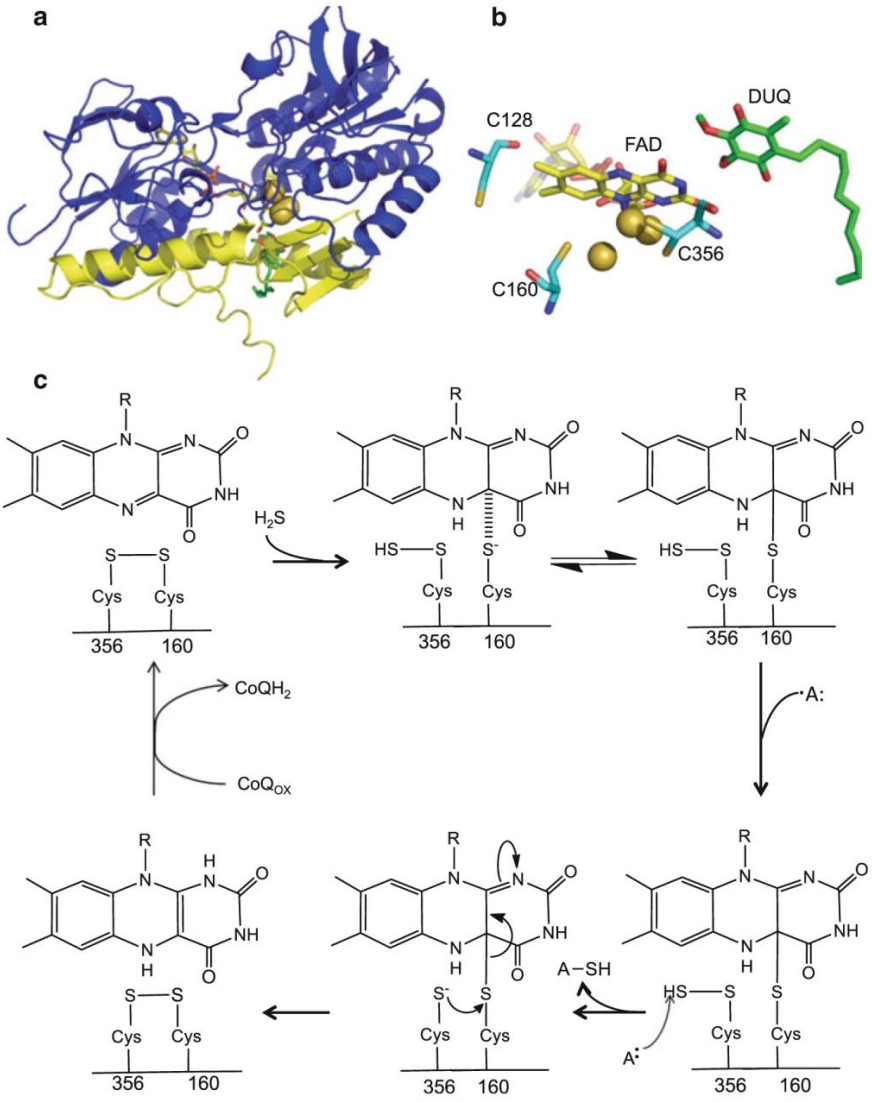


**Figure 1.5. Structure and reaction mechanism of SQR**. (a) Structure of *A. ferrooxidans* SQR monomer displaying the N-terminal Rossman fold domains (blue) and the C-terminal membrane binding domain (yellow) and the cofactors (green). (b) Close-up of the *A. ferrooxidans* SQR active site viewing the *re* face of the FAD isoalloxazine ring and decylubiquinone (DUQ) on the *si* face of FAD. Sulfur atoms between the active site cysteine residues are shown as yellow spheres. Figs. 1.5a and b were generated using PDB file 3T31. (c) Proposed mechanism of SQR. Reaction of $H_2S$ reduces the active site disulfide bond and results in the formation of a persulfide on one cysteine and a covalent linkage between the other cysteine and FAD. The cysteine bound persulfide is released from the enzyme by an acceptor molecule. Reformation of the active site disulfide results in reduction of FAD to $FADH_2$. Electrons are then transferred from FADH2 to ubiquinone allowing for regeneration of the oxidized active site.

#### 1.3.2.2 Catalytic Mechanism of SQR

The catalytic cycle of SQR is initiated by nucleophilic attack of the sulfide on the disulfide resulting in the formation of a persulfide and a cysteine thiolate (Fig. 1.5C) (88,92-95). The cysteine thiolate attacks the FAD cofactor forming a C4A adduct. Nucleophilic attack of an acceptor on the sulfane sulfur results in reformation of the active site disulfide and subsequent two-electron transfer to the FAD results in formation of $FADH_2$. Electron transfer from $FADH_2$ to ubiquinone regenerates FAD.

In bacterial SQRs, multiple rounds of electron transfer occur from sulfide to quinone without release of the persulfide at the end of each catalytic cycle (88,92-95). Instead, the catalytic cycle repeats until the maximum length of the polysulfide product that can be accommodated in the active site is obtained, at which point two consecutive nucleophilic attacks by the sulfide results in product release and reformation of the active site disulfide. Snapshots of these polysulfide species have been observed in structures of prokaryotic SQRs. The structure of *A. ambivalens* SQR revealed a trisulfide bridge between the two active site cysteines (88), while the *A. ferrooxidans* structure revealed a branched intermediate between the two cysteine residues consisting of five sulfur atoms (93,94). In the *A. aeolicus* SQR structures, both linear and cyclic polysulfur intermediates were observed (92). The released product can be soluble polysulfide containing up to ten sulfur atoms (96) or an octasulfur ring (92).

In contrast, in mammalian SQRs, the persulfide product is transferred to an acceptor at the end of each catalytic cycle. Although several molecules have been proposed as acceptors of the persulfide product including sulfite and glutathione, the identity of the physiological co-substrate is not known (95). Human SQR utilizes a number of small molecules as acceptors. It exhibits a $k_{cat}$ value of 82 ± 6 $s^{-1}$ in the presence of 1 mM cyanide (95). With sulfite as an

acceptor SQR displays a $K_m$ value of 0.22 0.02 mM with a $k_{cat}$ of 373 ± 13 $s^{-1}$. In contrast, GSH, cysteine an homocysteine display nearly identical $K_m$ values of 22 ± 3, 23 ± 4 and 22 ± 3.5 mM and $k_{cat}$ values of 113 ± 9, 94 ± 4 and 92 ± 5 $s^{-1}$ respectively (97). As intracellular heptatic glutathione concentrations relatively high, 7mM, it is expected that GSH is the primary acceptor under physiological conditions (97-99). It is not known whether ETHE1 can directly accept the persulfide product from SQR.

### 1.3.3 Persulfide Dioxygenase (PDO)

PDO, also known as ETHE1, is a soluble, mitochondrial matrix enzyme that catalyzes the oxidation of glutathione persulfide to sulfite (13,100,101). However, the physiological substrate is not known unequivocally. PDO contains a mononuclear non-heme iron in its active site (102) (103). Mutations in PDO result in ethylmalonic encephalopathy, an autosomal recessive disorder that results in developmental delay hemorrhagic diarrhea, acrocyanosis, petechiae, and progressive neurological failure (100,104,105). The clinical profile of ethylmalonic encephalopathy includes high levels of lactate, high C5 and C4 acylcarnitine levels in blood, increased ethylmalonic acid concentrations in urine and cytochrome c oxidase deficiency in muscle and brain (100,106,107). PDO deficiency leads to accumulation of thiosulfate and sulfide with the latter inhibiting cytochrome *c* oxidase and possibly other enzymes and accounting in part for the observed pathology (108).

Both glutathione persulfide (GSSH) and CoA persulfide (CoA-SSH) serve as substrates for human PDO while cysteine persulfide, glutathione and thiosulfate are not substrates (101). The specific activity of the enzyme with CoA-SSH is ~50-fold lower than with GSSH. Interestingly, 5 mM glutathione, a high but physiological relevant concentration, increases the catalytic efficiency of the PDO ~3-fold. Despite the similarity between PDO and glyoxylase II,

the former is unable to hydrolyze S-D-lactoylglutathione and other glutathione thioesters like glyoxylase II (103). This is most likely due to a C-terminal loop covering much of the active site in the dioxygenase making it smaller than the glyoxylase II active site (102,103).

#### 1.3.3.1 Structural Organization of Persulfide Dioxygenase

PDO has a typical metallo-β-lactamase fold containing two central β-sheets enclosed by three helices on each side (Fig. 1.6A). The active site iron is ligated via two histidines and one aspartate residue, His84, His135 and Asp154 (Fig. 1.6B). The three remaining coordination sites are occupied by water resulting in octahedral coordination, typical for ferrous iron (102,103). There are conflicting reports of the oligomeric state of the enzyme indicating it exists as either a monomer (101) or a dimer (109).

The geometry of the iron site in PDO resembles that of the 2-His-1-carboxylate facial triad family of oxygenases (110), a common structural motif that binds mononuclear non-heme $Fe^{2+}$. The three coordination sites occupied by water are available for binding ligands such as $O_2$, substrates and/or cofactors, and allow the enzymes to tune the reactivity of the iron center (111,112). With three coordination sites occupied by solvent, the metal center is not reactive towards dioxygen. Substrate binding displaces solvent molecules and results in formation of a five-coordinate metal center. Replacement of neutral solvent molecules with an anionic ligand can decrease the Fe(III)/Fe(II) redox potential rendering the iron center more susceptible to oxidation by dioxygen (111). Hence, substrate binding primes the iron center for dioxygen binding and protects the enzyme from auto-inactivation (111).

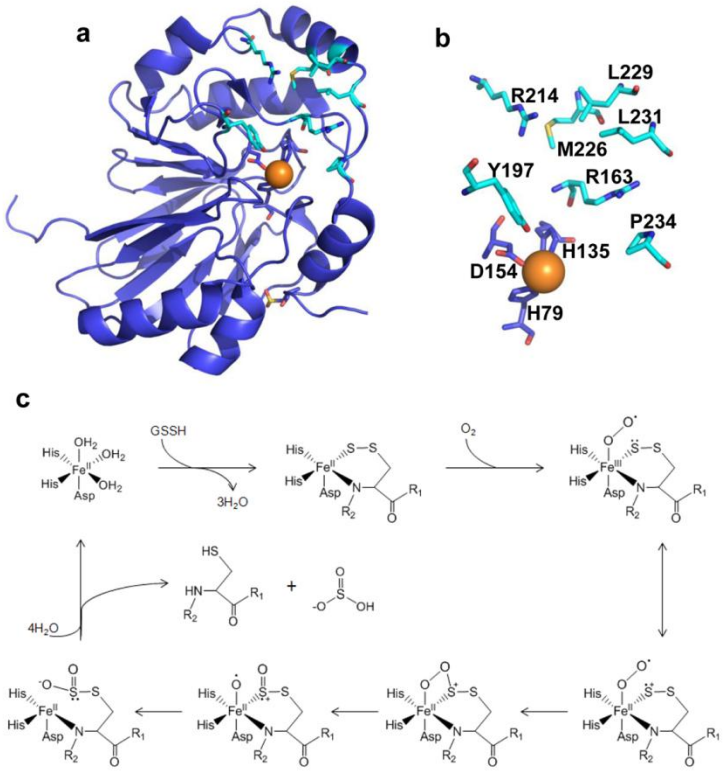


**Figure 1.6. Structure and catalytic mechanism of PDO**. (a) Structure of the human persulfide PDO. The mononuclear non-heme iron is shown in orange. (b) Close up of the active site of PDO. The mononuclear non-heme iron is coordinated by the 2His-1Asp facial triad residues. Figs. 1.6a and b were generated using PDB file 4CHL. (c) Proposed catalytic mechanism of PDO for sulfite generation. Binding of the GSSH substrate displaces coordinated water and promotes binding of oxygen to the iron center to form the Fe (III) superoxo intermediate. Resonance allows for partial radical cation character of the coordinated sulfur leading to recombination and formation of a cyclic peroxo-intermediate. Cleavage of the O-O bond results in a sulfoxy-cation and an iron-bound activated oxygen atom which is transferred to the sulfur to sulfoxy-cation. Subsequent hydrolysis yields sulfite, and GSH is displaced from the active site upon water binding to the metal center. *R1* and *R2* represent residues glutamate and glycine in the GSSH substrate.

The substrate-binding site is predicted to comprise residues Met226, Leu229, Leu231, Pro234, Arg163, Tyr197 and Arg214 based on modeling of GSSH in the active site (109). While not predicted to directly interact with the substrate, residues Met226, Leu229, Leu231, Pro234 line one side of the active site pocket and are predicted to aid in positioning the substrate toward the iron center. Arg163 is predicted to be hydrogen bonded with the glutamate portion of the

GSSH substrate and Arg214 is predicted to be in hydrogen bond distance of the glycine portion of GSSH. Similarly, Tyr197 is predicted to be within hydrogen bonding distance of the cysteine portion of GSSH, while the sulfane sulfur of GSSH would be coordinated to the iron center (109).

### 1.3.3.2 Catalytic Mechanism of PDO

Kinetic characterization of human PDO and two mutants mimicking missense mutations described in ethylmalonic aciduria patients, T151I and D196N, have been described (101). In the presence of GSSH, the $V_{max}$ for human PDO is 113 ± 4 μmol $min^{-1}$ mg $protein^{-1}$, which corresponds to a $k_{cat}$ of 47 $s^{-1}$ at 22 ˚C. Glutathione (5 mM) decreases the $K_M$ for GSSH ~1.4 fold and increases $k_{cat}$ ~2.2-fold yielding an ~3-fold increase in $k_{cat}/K_m$. The physiological relevance of the modulation of PDO activity by GSH is not known. The T152I mutant does not affect the $K_m$ for GSSH while the $k_{cat}$ is diminished ~4 fold and correlates with an ~2.5 fold lower iron content compared to wild-type enzyme. Thr152 is located on the same loop as Asp154, an iron ligand, and participates in a hydrogen bonding interaction with the backbone of Leu156, which may be necessary for correct positioning of Asp154. The Thr152I mutation would result in loss of the interaction with Leu156 possibly leading to repositioning of Asp154 (101).

The impact of the D196N mutation is to increase the $K_m$ for GSSH ~2-fold while leaving the $k_{cat}$ unaltered. Asp196 is located on an internal loop distal from the active site and is proposed to hydrogen bond with Phe200 and His198 to stabilize the loop. The D196N mutation likely destabilizes this loop. Several other pathogenic missense mutations have been described in human persulfide dioxygenase and include Y38C, L55P, T136A, R163Q, R163W, C161Y, T164K and L185R (104,105,113). Many of these mutations are predicted to be located near the active site and may disrupt metal, substrate binding and/or destabilize the enzyme.

The reaction mechanism proposed for PDO is adapted from that described for cysteine dioxygenase (102) and is also based on the general reaction mechanism of mononuclear non-heme iron oxygenases (111,112). In the proposed mechanism (101), solvent is displaced from the iron upon GSSH binding (Fig. 1.6C). The sulfane sulfur and a nitrogen atom from GSSH coordinate to the iron center resulting in a five-coordinate iron species, which is primed for $O_2$ binding. Binding of $O_2$ results in formation of a Fe (III) superoxo intermediate in which the coordinated sulfur acquires a partial radical cation character via resonance. Recombination of the Fe(III) superoxo species with the coordinated sulfur atom leads to formation of a cyclic peroxo-intermediate and is followed by homolytic cleavage of the O-O bond resulting in a sulfoxy-cation species and a metal-bound activated oxygen atom. Transfer of the activated oxygen to the sulfur followed by and hydrolysis yields sulfite. Finally, release of GSH followed by rebinding of solvent to the iron completes the catalytic cycle (101).

### 1.3.4 Rhodanese

Rhodanese is a widely distributed protein found in Archaea, bacteria and eukaryotes (114). It is a mitochondrial matrix protein that catalyzes the transfer of a sulfur atom from a sulfur donor to an acceptor (Eqs. 1.18-1.19).

$$SO_3^{2-} + RSSH \rightarrow S_2O_3^{2-} + RSH \qquad [1.18]$$

$$S_2O_3^{2-} + CN^- \rightarrow SO_3^{2-} + SCN^- \qquad [1.19]$$

Despite extensive studies on rhodanese, its precise physiological function is still not known. Historically, rhodanese was thought to be involved in cyanide detoxification due to its ability to convert cyanide and thiosulfate to thiocyanate (115,116). In fact, thiosulfate along with sodium nitrite is administered to treat acute cyanide poisoning. Cells that are routinely exposed to gaseous and dietary intake of cyanide, such as the epithelial cells surrounding bronchioles,

hepatocytes that are proximal to the liver's blood supply and proximal tubule cells in kidney have the highest rhodanese levels (117). However, the activity of rhodanese is confined to the mitochondrial matrix, where thiosulfate enters with low efficiency suggesting that a different sulfur source than thiosulfate might be used for clearing cyanide (118). Alternatively, rhodanese might play a role in sulfur metabolism (13,118), particularly for mitochondrial thiosulfate production by transfer of the sulfane sulfur from a donor to sulfite (13).

#### 1.3.4.1 Structural Organization of Rhodanese

Bovine liver rhodanese, which shares 89% sequence identity with the human enzyme, has been characterized extensively. This protein is folded into two globular domains of equal size, with each containing a five stranded parallel β-sheet enclosed by two α-helices on one side and three α-helices on the other (Fig. 1.7A) (119). While both domains have a similar fold, the sequence homology is low with only 16% sequence identity between them. The N-terminal domain is inactive due to replacement of the catalytic cysteine residue with an aspartate and plays a role in forming the active site. The catalytic Cys247 residue in bovine liver rhodanese is located at the bottom of a pocket formed between the two domains (Fig. 1.7B). The walls of the pocket comprise hydrophobic and hydrophilic regions. The hydrophobic regions consist of residues Phe212, Phe106, Tyr107, Trp35, and Val251, and the hydrophilic region comprise residues Asp180, Ser181, Arg182, Arg186, Glu193, Arg248, Lys249, and Thr252. The persulfide intermediate is stabilized by hydrogen bonds from the backbone amides of Arg248, Lys249, Val251 and the hydroxyl group of Thr252. Residues Arg186 and Lys249 located at the entrance of the active site pocket and their side chains are positioned to participate in binding and positioning of thiosulfate through ionic interactions and to polarize the sulfane sulfur for nucleophilic attack by the Cys247 thiol. It is possible that the hydrophobic region lining the

active site is important for binding other substrates that contain aromatic or hydrophobic residues (119).

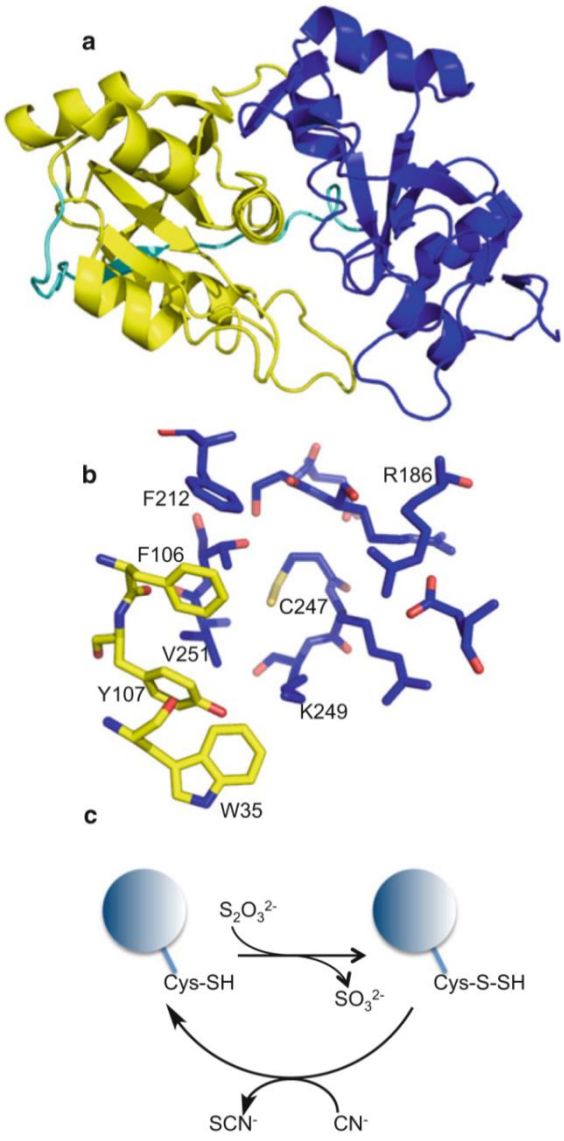


**Figure 1.7. Structure and reaction mechanism of rhodanese**. (a) Structure of *Bos taurus* rhodanese. The protein comprises of two equal sized N-terminal (yellow) and C-terminal (blue) globular domains. The linker region between the two domains is shown in cyan. (b) Close up of the rhodanese active site. The active site is located at the interface of the two domains. N-and C-terminal domain residues contribute to a hydrophobic patch (yellow), while C-terminal domain residues contribute to a hydrophilic region (blue). Figs. 1.7a and b were generated using PDB file 1RHD. (c) Catalytic mechanism of rhodanese for thiocyanate generation from thiosulfate. Rhodanese catalyzes the sulfur transfer from thiosulfate to an active site cysteine, resulting in sulfite and a rhodanese-bound persulfide intermediate. The latter reacts with a sulfur acceptor, in this example cyanide, to generate thiocyanate.

### 1.3.4.2 Catalytic Mechanism of Rhodanese

The sulfurtransferase reaction catalyzed by rhodanese occurs via a double displacement mechanism and involves formation of a stable persulfide intermediate (114,119). The reaction is initiated by the nucleophilic attack of the Cys247 thiolate on the sulfane sulfur of thiosulfate resulting in formation of an enzyme-bound persulfide intermediate (Fig. 1.7C). Next, sulfite is released and followed by binding of a sulfur acceptor, which attacks the sulfane sulfur of the persulfide intermediate. In the case of cyanide, the product of this sulfur transfer reaction is thiocyanate (119). Release of thiocyanate completes the catalytic cycle.

Rhodanese also displays sulfurtransferase activity between a persulfide donor and sulfite acceptor (equation 18). The $K_m$ values for cyanide and thiosulfate for bovine rhodanese are 0.087 ± 0.009 mM and 16.2 ± 1.6 mM, respectively (13). Similar values have also been reported for rat and lugworm rhodanese (13). The human rhodanese displays $K_m$ values of 39.5 ± 2.5 mM and 29 ± 4 mM for thiosulfate and cyanide respectively (120). In contrast, the $K_m$s for GSSH and sulfite are considerably lower (450 ± 4 μM and 60 ± 10 μM respectively), suggesting that the sulfurtransferase activity of rhodanese from GSSH to sulfite might be more physiologically relevant than its cyanide detoxification activity (120).

### 1.3.5 Mitochondrial Sulfide Oxidation: Unanswered Questions

Endogenously produced $H_2S$ must be regulated to maintain low intracellular concentrations. In mammals, steady-state levels of $H_2S$ are governed by flux through the synthetic pathways (transsulfuration and CAT/MST) and the sulfide oxidation pathway (3). In some prokaryotes, sulfide oxidation is essential for ATP generation. Similarly, low concentrations of $H_2S$ (0.1-1 μM), can stimulate mammalian mitochondrial ATP production and serve as an inorganic source of ATP (4,121,122). An important unanswered question regarding

the sulfide oxidation pathway is its organization. Since SQR oxidizes sulfide, it is reasonable to propose that it catalyzes the first step in the pathway. The ambiguity arises thereafter since the persulfide acceptor of SQR is not known. Both PDO and rhodanese can oxidize persulfide forming either sulfite or thiosulfate, respectively. However, the co-substrate for rhodanese is sulfite, which is derived from the PDO-catalyzed reaction. This dependence of rhodanese on the product of PDO suggests that oxidation of $H_2S$ proceeds through SQR, the dioxygenase and then rhodanese. The products of this pathway thus configured are thiosulfate and sulfate, which is derived by oxidation of sulfite catalyzed by sulfite oxidase. The presence of two routes for sulfite removal in the mitochondria is paralleled in microbes where multiple sulfite oxidation routes co-exist in the same organism, e.g. the oxidation of sulfite by sulfite oxidase or via the adenosine-5´-phosphosulfate reductase pathway (81).

Variants of PDO fused to rhodanese are found in certain bacteria (100). The occurrence of fused PDO/rhodanese variants suggests that their proximity enhances utilization of sulfite produced by one active site and consumed by the other. However, this order of the pathway is brought into question by clinical data on PDO deficient patients and PDO knockout mice in which sulfite levels are greatly diminished, as expected, but thiosulfate and $H_2S$ levels are elevated (100). Elevated thiosulfate in the absence of PDO activity suggests that an alternative route for sulfite exists, which supports production of thiosulfate by rhodanese (101). One branch of the cysteine catabolic pathway is initiated by cysteine dioxygenase that oxidizes cysteine to cysteinesulfinate, which is further metabolized to 3-sulfinylpyruvate by CAT. 3-sulfinylpyruvate is unstable and decomposes to form pyruvate and sulfite. We have posited that the persulfide product of SQR is preferentially utilized by rhodanese under conditions of PDO deficiency, explaining the observed accumulation of thiosulfate under these conditions (101). However,

while cysteine catabolism is up regulated under conditions of cysteine excess (123), it is unclear how this pathway responds to PDO deficiency and its role in sulfite production under these conditions warrants investigation.

In this context, understanding the fate of the persulfide product of SQR is pertinent. Bacterial polysulfide products of SQR are stored in sulfur globules until further oxidation to sulfate. However, sulfur globules have not been reported in higher organisms and in fact, eukaryotic lugworm, rat, and human SQRs require a persulfide acceptor for catalytic turnover under in vitro conditions (13,95). The persulfide product bound to the SQR active site might be either oxidized directly by PDO or rhodanese or transferred to a small molecule carrier such as GSH with the resulting GSSH serving as substrate for the PDO and rhodanese. Sulfane sulfur acceptors that support the activity of SQR include sulfite, cyanide, sulfide and glutathione. Human SQR has been proposed to utilize sulfite as the physiological acceptor since it displays a 4-or 13-fold higher catalytic efficiency in the presence of either cyanide or sulfite versus glutathione (95). The product of persulfide transfer to sulfite is thiosulfate, which is however not a substrate for PDO (101). Of the persulfide donors that have been tested as substrates for PDO only CoA-SSH exhibits activity in addition to GSSH (101). Hence, the mechanism by which the persulfide product of SQR is transferred to the PDO and rhodanese is an important unanswered question in the field.

### 1.4 References


1. Kimura, H. (2010) *Antioxid Redox Signal* **12**, 1111-1123
2. Levitt, M. D., Abdel-Rehim, M. S., and Furne, J. (2011) *Antioxid Redox Signal* **15**, 373-378
3. Vitvitsky, V., Kabil, O., and Banerjee, R. (2012) *Antioxid Redox Signal* **17**, 22-31

4. Bouillaud, F., and Blachier, F. (2011) *Antioxid Redox Signal* **15**, 379-391

5. Kabil, O., and Banerjee, R. (2010) *J Biol Chem* **285**, 21903-21907

6. Singh, S., and Banerjee, R. (2011) *Biochim Biophys Acta* **1814**, 1518-1527

7. Chen, X., Jhee, K. H., and Kruger, W. D. (2004) *J Biol Chem* **279**, 52082-52086

8. Chiku, T., Padovani, D., Zhu, W., Singh, S., Vitvitsky, V., and Banerjee, R. (2009) *J Biol Chem* **284**, 11601-11612

9. Singh, S., Padovani, D., Leslie, R. A., Chiku, T., and Banerjee, R. (2009) *J Biol Chem* **284**, 22457-22466

10. Nagahara, N., Ito, T., Kitamura, H., and Nishino, T. (1998) *Histochem Cell Biol* **110**, 243-250

11. Shibuya, N., Tanaka, M., Yoshida, M., Ogasawara, Y., Togawa, T., Ishii, K., and Kimura, H. (2009) *Antioxid Redox Signal* **11**, 703-714

12. Shibuya, N., Koike, S., Tanaka, M., Ishigami-Yuasa, M., Kimura, Y., Ogasawara, Y., Fukui, K., Nagahara, N., and Kimura, H. (2013) *Nat Commun* **4**, 1366

13. Hildebrandt, T. M., and Grieshaber, M. K. (2008) *FEBS J* **275**, 3352-3361

14. Banerjee, R., Evande, R., Kabil, O., Ojha, S., and Taoka, S. (2003) *Biochim Biophys Acta* **1647**, 30-35

15. Kraus, J. P., Janosik, M., Kozich, V., Mandell, R., Shih, V., Sperandeo, M. P., Sebastio, G., de Franchis, R., Andria, G., Kluijtmans, L. A., Blom, H., Boers, G. H., Gordon, R. B., Kamoun, P., Tsai, M. Y., Kruger, W. D., Koch, H. G., Ohura, T., and Gaustadnes, M. (1999) *Hum Mutat* **13**, 362-375

16. Mudd, S. H., Finkelstein, J. D., Irreverre, F., and Laster, L. (1964) *Science* **143**, 1443-1445

17. Sen, U., Tyagi, N., Kumar, M., Moshal, K. S., Rodriguez, W. E., and Tyagi, S. C. (2007) *Am J Physiol Cell Physiol* **293**, C1779-1787

18. Bateman, A. (1997) *Trends Biochem Sci* **22**, 12-13

19. Meier, M., Janosik, M., Kery, V., Kraus, J. P., and Burkhard, P. (2001) *EMBO J* **20**, 3910-3916

20. Taoka, S., Lepore, B. W., Kabil, O., Ojha, S., Ringe, D., and Banerjee, R. (2002)

*Biochemistry* **41**, 10454-10461

21. Koutmos, M., Kabil, O., Smith, J. L., and Banerjee, R. (2010) *Proc Natl Acad Sci U S A* **107**, 20958-20963

22. Quazi, F., and Aitken, S. M. (2009) *Biochim Biophys Acta* **1794**, 892-897

23. Singh, S., Madzelan, P., Stasser, J., Weeks, C. L., Becker, D., Spiro, T. G., Penner-Hahn, J., and Banerjee, R. (2009) *J Inorg Biochem* **103**, 689-697

24. Weeks, C. L., Singh, S., Madzelan, P., Banerjee, R., and Spiro, T. G. (2009) *J Am Chem Soc* **131**, 12809-12816

25. Yadav, P. K., and Banerjee, R. (2012) *J Biol Chem* **287**, 43464-43471

26. Jhee, K. H., Niks, D., McPhie, P., Dunn, M. F., and Miles, E. W. (2001) *Biochemistry* **40**, 10873-10880

27. Taoka, S., and Banerjee, R. (2002) *J Biol Chem* **277**, 22421-22425

28. Singh, S., Ballou, D. P., and Banerjee, R. (2011) *Biochemistry* **50**, 419-425

29. Evande, R., Ojha, S., and Banerjee, R. (2004) *Arch Biochem Biophys* **427**, 188-196

30. Ojha, S., Hwang, J., Kabil, O., Penner-Hahn, J. E., and Banerjee, R. (2000) *Biochemistry* **39**, 10542-10547

31. Green, E. L., Taoka, S., Banerjee, R., and Loehr, T. M. (2001) *Biochemistry* **40**, 459-463

32. Taoka, S., Ohja, S., Shan, X., Kruger, W. D., and Banerjee, R. (1998) *J Biol Chem* **273**, 25179-25184

33. Ojha, S., Wu, J., LoBrutto, R., and Banerjee, R. (2002) *Biochemistry* **41**, 4649-4654

34. Taoka, S., and Banerjee, R. (2001) *J Inorg Biochem* **87**, 245-251

35. Taoka, S., Green, E. L., Loehr, T. M., and Banerjee, R. (2001) *J Inorg Biochem* **87**, 253-259

36. Singh, S., Madzelan, P., and Banerjee, R. (2007) *Nat Prod Rep* **24**, 631-639

37. Taoka, S., West, M., and Banerjee, R. (1999) *Biochemistry* **38**, 2738-2744

38. Gherasim, C., Yadav, P. K., Kabil, O., Niu, W. N., and Banerjee, R. (2014) *PLoS One* **9**, e85544

39. Carballal, S., Madzelan, P., Zinola, C. F., Grana, M., Radi, R., Banerjee, R., and Alvarez, B. (2008) *Biochemistry* **47**, 3194-3201

40. Kabil, O., Weeks, C. L., Carballal, S., Gherasim, C., Alvarez, B., Spiro, T. G., and Banerjee, R. (2011) *Biochemistry* **50**, 8261-8263

41. Yadav, P. K., Xie, P., and Banerjee, R. (2012) *J Biol Chem* **287**, 37611-37620

42. Scott, J. W., Hawley, S. A., Green, K. A., Anis, M., Stewart, G., Scullion, G. A., Norman, D. G., and Hardie, D. G. (2004) *J Clin Invest* **113**, 274-284

43. Finkelstein, J. D., Kyle, W. E., Martin, J. L., and Pick, A. M. (1975) *Biochem Biophys Res Commun* **66**, 81-87

44. Kery, V., Poneleit, L., and Kraus, J. P. (1998) *Arch Biochem Biophys* **355**, 222-232

45. Shan, X., and Kruger, W. D. (1998) *Nat Genet* **19**, 91-93

46. Janosik, M., Kery, V., Gaustadnes, M., Maclean, K. N., and Kraus, J. P. (2001) *Biochemistry* **40**, 10625-10633

47. Evande, R., Blom, H., Boers, G. H., and Banerjee, R. (2002) *Biochemistry* **41**, 11832-11837

48. Prudova, A., Bauman, Z., Braun, A., Vitvitsky, V., Lu, S. C., and Banerjee, R. (2006) *Proc Natl Acad Sci U S A* **103**, 6489-6494

49. Pey, A. L., Majtan, T., Sanchez-Ruiz, J. M., and Kraus, J. P. (2013) *Biochem J* **449**, 109-121

50. Agrawal, N., and Banerjee, R. (2008) *PLoS One* **3**, e4032

51. Yamamoto, T., Takano, N., Ishiwata, K., and Suematsu, M. (2011) *J Clin Biochem Nutr* **48**, 96-100

52. Zhong, W. X., Wang, Y. B., Peng, L., Ge, X. Z., Zhang, J., Liu, S. S., Zhang, X. N., Xu, Z. H., Chen, Z., and Luo, J. H. (2012) *J Biol Chem* **287**, 34189-34201

53. Messerschmidt, A., Worbs, M., Steegborn, C., Wahl, M. C., Huber, R., Laber, B., and Clausen, T. (2003) *Biol Chem* **384**, 373-386

54. Sun, Q., Collins, R., Huang, S., Holmberg-Schiavone, L., Anand, G. S., Tan, C. H., van-den-Berg, S., Deng, L. W., Moore, P. K., Karlberg, T., and Sivaraman, J. (2009) *J Biol Chem* **284**, 3076-3085

55. Wang, J., and Hegele, R. A. (2003) *Hum Genet* **112**, 404-408

56. Huang, S., Chua, J. H., Yew, W. S., Sivaraman, J., Moore, P. K., Tan, C. H., and Deng, L. W. (2010) *J Mol Biol* **396**, 708-718

57. Yamagata, S., Yasugahira, T., Okuda, Y., and Iwama, T. (2003) *J Biochem* **134**, 607-613

58. Stipanuk, M. H., and Beck, P. W. (1982) *Biochem J* **206**, 267-277

59. Yang, G., Wu, L., Jiang, B., Yang, W., Qi, J., Cao, K., Meng, Q., Mustafa, A. K., Mu, W., Zhang, S., Snyder, S. H., and Wang, R. (2008) *Science* **322**, 587-590

60. Mikami, Y., Shibuya, N., Ogasawara, Y., and Kimura, H. (2013) *Biochem Biophys Res Commun* **431**, 131-135

61. Meister, A., Fraser, P. E., and Tice, S. V. (1954) *J Biol Chem* **206**, 561-575

62. Nagahara, N., Yoshii, T., Abe, Y., and Matsumura, T. (2007) *J Biol Chem* **282**, 1561-1569

63. Mikami, Y., Shibuya, N., Kimura, Y., Nagahara, N., Ogasawara, Y., and Kimura, H. (2011) *Biochem J* **439**, 479-485

64. Yadav, P. K., Yamada, K., Chiku, T., Koutmos, M., and Banerjee, R. (2013) *J Biol Chem* **288**, 20002-20013

65. Nagahara, N., Ito, T., and Minami, M. (1999) *Histol Histopathol* **14**, 1277-1286

66. Crawhall, J. C., Parker, R., Sneddon, W., Young, E. P., Ampola, M. G., Efron, M. L., and Bixby, E. M. (1968) *Science* **160**, 419-420

67. Nagahara, N., and Sawada, N. (2006) *Curr Med Chem* **13**, 1219-1230

68. Alphey, M. S., Williams, R. A., Mottram, J. C., Coombs, G. H., and Hunter, W. N. (2003) *J Biol Chem* **278**, 48219-48227

69. Spallarossa, A., Forlani, F., Carpen, A., Armirotti, A., Pagani, S., Bolognesi, M., and Bordo, D. (2004) *J Mol Biol* **335**, 583-593

70. Williams, R. A., Kelly, S. M., Mottram, J. C., and Coombs, G. H. (2003) *J Biol Chem* **278**, 1480-1486

71. Nagahara, N., and Nishino, T. (1996) *J Biol Chem* **271**, 27395-27401

72. Jarabak, R., and Westley, J. (1978) *Arch Biochem Biophys* **185**, 458-465

73. Mikami, Y., Shibuya, N., Kimura, Y., Nagahara, N., Yamada, M., and Kimura, H. (2011)

*J Biol Chem* **286**, 39379-39386

74. Nagahara, N., and Katayama, A. (2005) *J Biol Chem* **280**, 34569-34576

75. Nagahara, N. (2013) *Antioxid Redox Signal* **19**, 1792-1802

76. Kabil, O., Vitvitsky, V., Xie, P., and Banerjee, R. (2011) *Antioxid Redox Signal* **15**, 363-372

77. Gregersen, L. H., Bryant, D. A., and Frigaard, N. U. (2011) *Front Microbiol* **2**, 116

78. Grimm, F., Franz, B., and Dahl, C. (2011) *Front Microbiol* **2**, 51

79. Chen, Z. W., Koh, M., Van Driessche, G., Van Beeumen, J. J., Bartsch, R. G., Meyer, T. E., Cusanovich, M. A., and Mathews, F. S. (1994) *Science* **266**, 430-432

80. Holkenbrink, C., Barbas, S. O., Mellerup, A., Otaki, H., and Frigaard, N. U. (2011) *Microbiology* **157**, 1229-1239

81. Kappler, U., and Dahl, C. (2001) *FEMS Microbiol Lett* **203**, 1-9

82. Friedrich, C. G., Rother, D., Bardischewsky, F., Quentmeier, A., and Fischer, J. (2001) *Appl Environ Microbiol* **67**, 2873-2882

83. Sakurai, H., Ogawa, T., Shiga, M., and Inoue, K. (2010) *Photosynth Res* **104**, 163-176

84. Rohwerder, T., and Sand, W. (2003) *Microbiology* **149**, 1699-1710

85. Kletzin, A. (1992) *J Bacteriol* **174**, 5854-5859

86. Kletzin, A., Urich, T., Muller, F., Bandeiras, T. M., and Gomes, C. M. (2004) *J Bioenerg Biomembr* **36**, 77-91

87. Urich, T., Gomes, C. M., Kletzin, A., and Frazao, C. (2006) *Science* **311**, 996-1000

88. Brito, J. A., Sousa, F. L., Stelter, M., Bandeiras, T. M., Vonrhein, C., Teixeira, M., Pereira, M. M., and Archer, M. (2009) *Biochemistry* **48**, 5613-5622

89. Zimmermann, P., Laska, S., and Kletzin, A. (1999) *Arch Microbiol* **172**, 76-82

90. Theissen, U., Hoffmeister, M., Grieshaber, M., and Martin, W. (2003) *Mol Biol Evol* **20**, 1564-1574

91. Marcia, M., Ermler, U., Peng, G., and Michel, H. (2010) *Proteins* **78**, 1073-1083

92. Marcia, M., Ermler, U., Peng, G., and Michel, H. (2009) *Proc Natl Acad Sci U S A* **106**,

9625-9630

93. Cherney, M. M., Zhang, Y., Solomonson, M., Weiner, J. H., and James, M. N. (2010) *J Mol Biol* **398**, 292-305

94. Cherney, M. M., Zhang, Y., James, M. N., and Weiner, J. H. (2012) *J Struct Biol* **178**, 319-328

95. Jackson, M. R., Melideo, S. L., and Jorns, M. S. (2012) *Biochemistry* **51**, 6804-6815

96. Griesbeck, C., Schutz, M., Schodl, T., Bathe, S., Nausch, L., Mederer, N., Vielreicher, M., and Hauska, G. (2002) *Biochemistry* **41**, 11552-11565

97. Libiad, M., Yadav, P. K., Vitvitsky, V., Martinov, M., and Banerjee, R. (2014) *J Biol Chem* **289**, 30901-30910

98. Mishanina, T. V., Libiad, M., and Banerjee, R. (2015) *Nat Chem Biol* **11**, 457-464

99. Vitvitsky, V., Dayal, S., Stabler, S., Zhou, Y., Wang, H., Lentz, S. R., and Banerjee, R. (2004) *Am J Physiol Regul Integr Comp Physiol* **287**, R39-46

100. Tiranti, V., Viscomi, C., Hildebrandt, T., Di Meo, I., Mineri, R., Tiveron, C., Levitt, M. D., Prelle, A., Fagiolari, G., Rimoldi, M., and Zeviani, M. (2009) *Nat Med* **15**, 200-205

101. Kabil, O., and Banerjee, R. (2012) *J Biol Chem* **287**, 44561-44567

102. McCoy, J. G., Bingman, C. A., Bitto, E., Holdorf, M. M., Makaroff, C. A., and Phillips, G. N., Jr. (2006) *Acta Crystallogr D Biol Crystallogr* **62**, 964-970

103. Holdorf, M. M., Bennett, B., Crowder, M. W., and Makaroff, C. A. (2008) *J Inorg Biochem* **102**, 1825-1830

104. Tiranti, V., D'Adamo, P., Briem, E., Ferrari, G., Mineri, R., Lamantea, E., Mandel, H., Balestri, P., Garcia-Silva, M. T., Vollmer, B., Rinaldo, P., Hahn, S. H., Leonard, J., Rahman, S., Dionisi-Vici, C., Garavaglia, B., Gasparini, P., and Zeviani, M. (2004) *Am J Hum Genet* **74**, 239-252

105. Mineri, R., Rimoldi, M., Burlina, A. B., Koskull, S., Perletti, C., Heese, B., von Dobeln, U., Mereghetti, P., Di Meo, I., Invernizzi, F., Zeviani, M., Uziel, G., and Tiranti, V. (2008) *J Med Genet* **45**, 473-478

106. Burlina, A., Zacchello, F., Dionisi-Vici, C., Bertini, E., Sabetta, G., Bennet, M. J., Hale, D. E., Schmidt-Sommerfeld, E., and Rinaldo, P. (1991) *Lancet* **338**, 1522-1523

107. Garcia-Silva, M. T., Campos, Y., Ribes, A., Briones, P., Cabello, A., Santos Borbujo, J., Arenas, J., and Garavaglia, B. (1994) *J Pediatr* **125**, 843-844

108. Di Meo, I., Fagiolari, G., Prelle, A., Viscomi, C., Zeviani, M., and Tiranti, V. (2011) *Antioxid Redox Signal* **15**, 353-362

109. Pettinati, I., Brem, J., McDonough, M. A., and Schofield, C. J. (2015) *Hum Mol Genet* **24**, 2458-2469

110. Hegg, E. L., and Que, L., Jr. (1997) *Eur J Biochem* **250**, 625-629

111. Koehntop, K. D., Emerson, J. P., and Que, L., Jr. (2005) *J Biol Inorg Chem* **10**, 87-93

112. Bruijnincx, P. C., van Koten, G., and Klein Gebbink, R. J. (2008) *Chem Soc Rev* **37**, 2716-2744

113. Tiranti, V., Briem, E., Lamantea, E., Mineri, R., Papaleo, E., De Gioia, L., Forlani, F., Rinaldo, P., Dickson, P., Abu-Libdeh, B., Cindro-Heberle, L., Owaidha, M., Jack, R. M., Christensen, E., Burlina, A., and Zeviani, M. (2006) *J Med Genet* **43**, 340-346

114. Cipollone, R., Ascenzi, P., and Visca, P. (2007) *IUBMB Life* **59**, 51-59

115. Westley, J. (1973) *Adv Enzymol Relat Areas Mol Biol* **39**, 327-368

116. Cipollone, R., Frangipani, E., Tiburzi, F., Imperi, F., Ascenzi, P., and Visca, P. (2007) *Appl Environ Microbiol* **73**, 390-398

117. Sylvester, M., and Sander, C. (1990) *Histochem J* **22**, 197-200

118. Westley, J., Adler, H., Westley, L., and Nishida, C. (1983) *Fundam Appl Toxicol* **3**, 377-382

119. Hol, W. G., Lijk, L. J., and Kalk, K. H. (1983) *Fundam Appl Toxicol* **3**, 370-376

120. Libiad, M., Sriraman, A., and Banerjee, R. (2015) *J Biol Chem* **290**, 23579-23588

121. Goubern, M., Andriamihaja, M., Nubel, T., Blachier, F., and Bouillaud, F. (2007) *FASEB J* **21**, 1699-1706

122. Modis, K., Coletta, C., Erdelyi, K., Papapetropoulos, A., and Szabo, C. (2013) *FASEB J* **27**, 601-611

123. Stipanuk, M. H., Hirschberger, L. L., Londono, M. P., Cresenzi, C. L., and Yu, A. F. (2004) *Am J Physiol Endocrinol Metab* **286**, E439-448

# Chapter 2

# Characterization of Human Persulfide Dioxygenase Mutations Associated with Ethylmalonic Encephalopathy

## 2.1 Abstract

Hydrogen sulfide ($H_2S$), a gas with toxicity comparable to cyanide is a signaling molecule that is capable of inducing a wide range of physiological effects, including acting as a vasorelaxant and a cardioprotectant during myocardial ischemia reperfusion. Although $H_2S$ has several beneficial effects, its concentrations must be strictly regulated to avoid toxicity. $H_2S$ is clearance occurs primarily via the mitochondrial sulfide oxidation pathway resulting in formation of thiosulfate and sulfate. Several enzymes are involved in this pathway: sulfide:quinone oxidoreductase (SQR), persulfide dioxygenase (PDO), rhodanese and sulfite oxidase. Mutation of PDO results in the autosomal recessive disorder ethylmalonic encephalopathy (EE). Over 20 PDO mutations have been described in EE patients. Kinetic characterization of several EE patient mutations (L55P, T136A, C161Y and R163W), was performed to determine the biochemical penalties incurred by these mutations. The mutants displayed varying degrees of decreased activity. R163W was the least impacted displaying 18-fold lower $k_{cat}/K_m$ compared to wild-type. L55P, C161Y and T136A displayed decreasing activity with 42-, 65- and 200-fold lower $k_{cat}/K_m$ values. Similarly, all mutants displayed decreased iron content. T136A, R163W, C161Y and L55P displayed 1.4-, 3-, 11- and 10.5-fold

lower iron content, respectively, compared to wild-type PDO. The thermal denaturation profiles of the PDO mutants revealed altered thermal stabilities with R16W, L55P, T136A and C161Y displaying 1.2-, 1.4-, 1.4- and 1.7-fold lower $T_m$ values compared to wild-type PDO.

## 2.2 Introduction

EE is an autosomal recessive disorder that is associated with pathological effects in the brain, gastrointestinal tract and peripheral vessels (1-3). It results in acrocyanosis, petechiae, hemorrhagic diarrhea, developmental delay and progressive neurological failure leading to necrotic lesions in the deep gray matter of the brain. Patients with EE usually succumb to the disease within the first decade of life (4-6).

The clinical profile of EE includes increased concentrations of ethylmalonic acid in urine, C4 and C5 acrylcarnitines in blood and a deficiency of cytochrome c oxidase in brain and muscle tissue (1,2,6). EE is caused by mutations in the *ethe1* gene that encodes a PDO, also known as ETHE1. Over 20 mutations have been described in the *ethe1* gene (3,5,7). PDO is a mitochondrial matrix protein that participates in the mitochondrial sulfide oxidation pathway where $H_2S$ is oxidized to end the products, sulfate and thiosulfate (8-10). In addition to PDO, the other enzymes involved in the mitochondrial sulfur oxidation pathway are SQR, rhodanese, and sulfite oxidase. PDO catalyzes the second step in the pathway, i.e. the oxidation of glutathione persulfide (GSSH) to sulfite (Eq. 2.1) (11,12).

$$GSSH + O_2 + H_2O \rightarrow GSH + SO_3^{2-} + 2H^+ \quad [2.1]$$

Sulfite can undergo further oxidation by sulfite oxidase to produce sulfate, or sulfur transfer via rhodanese and the sulfur donor GSSH, to produce thiosulfate.

PDO is a member of the metallo-β-lactamase family, and contains a mononuclear nonheme iron (10,13). PDO exists as a monomer or a dimer in solution (10,12,14). The structure

of human PDO displays a typical αββα metallo-β-lactamase-type fold consisting of two central β-sheet clusters enclosed by three helices on each side (12,15,16). The mononuclear iron is coordinated by a 2-His-1-Asp facial triad consisting of residues His79, His135, and Asp154. Three water molecules occupy the remaining coordination sites. The active site iron is located inside a large groove that is framed with positively charged residues on one side and a polar tyrosine on the other (12).

Mutations in PDO lead to an increase in levels of thiosulfate and sulfide in EE patients and in *ethe1*$^{-/-}$ mice (5,8). The majority of patient mutations are clustered near the iron coordination residues and the active site pocket suggesting that they may disrupt metal and substrate binding and destabilize the enzyme. To date, only four PDO mutations described in EE patients have been characterized. The D196N mutation, located on an internal loop away from the active site, has modest effects on enzymatic function, primarily affecting the $K_m$ for GSSH, which increases 2-fold compared to wild-type PDO. In contrast, the T1521 mutation, located upstream the iron ligand Asp154, displayed a 2.5-fold lower iron content and an ~4-fold lower $k_{cat.}$ (10). Both mutants showed significantly lower thermal stability ($T_m$ 10-15 ˚C lower) than wild-type PDO. In a separate study, the R163W and R163Q mutations, located near the active site and proposed to bind GSSH, were also shown to decrease the $T_m$ (~7-9 ˚C lower). These mutants also exhibited significantly lower iron reduction potentials (-310 mV for R163Q and -370 mV for R163W versus -272 mV for wild-type PDO) (14). While it was shown that the mutations resulted in an ~10-fold lower specific activity, kinetic characterization of the Arg163 mutations was not reported (14).

Herein, we report the kinetic characterization of four PDO patient mutations, L55P, T136A, C161Y, and R163W. These mutations impact to varying degrees, the kinetics, stability

and iron content of PDO compared to the wild-type protein and provide insights into the biochemical penalties associated with mutations distal from the active site.

### 2.3 Experimental Procedures

#### 2.3.1 Materials

Sodium sulfide, oxidized glutathione, pararosaniline hydrochloride and 2,4,6-tripyridyl-S-triazine were purchased from Sigma.

#### 2.3.2 Expression constructs for mutant PDOs

The PDO mutations were generated using the QuickChange kit (Stratagene) and the wild-type PDO expression construct as a template (10). Primers used in this study are listed in Table 2.1. The resulting plasmids were transformed into BL21 *E. coli* cells.

**TABLE 2.1 PDO mutagenesis primer sequences.**

| Mutation | Primer Sequence |
|---|---|
| L55P | Forward: 5'-CCGTTCTGATCGACCCAGTC**CCT**GAAACAGCGCC-3'<br>Reverse: 5'-GGCGCTGTTTC**AGG**GACTGGGTCGATCAGAACGG-3' |
| T136A | Forward: 5'-GCCAGCCCTGGCCAC**GCC**CCAGGCTGTGTCACC-3'<br>Reverse: 5'-GGTGACACAGCCTGG**GGC**GTGGCCAGGGCTGGC-3' |
| C161Y | Forward: 5'-CCCTGTTGATCCGTGGGT**ACG**GGCGGACAGACTTCC-3'<br>Reverse: 5'-GGAAGTCTGTCCGCC**CGT**ACCCACGGATCAACAGGG-3' |
| R163W | Forward: 5'-CCGTGGGTGTGGG**TGG**ACAGACTTCCAGCAAGGC-3'<br>Reverse: 5'-GCCTTGCTGGAAGTCTGT**CCA**CCCACACCCACGG-3' |

#### 2.3.3 Expression and purification of human PDO mutants

The recombinant PDO proteins were expressed in BL21 *E.coli* cells. A Luria Broth (LB) culture (200 mL) grown overnight at 37 $^{o}$C was used to inoculate 3 L of LB media. Cultures were grown at 28 °C and expression was induced with 100 μM isopropyl-β-D-

thiogalactopyranoside when the optical density at 600 nm reached 0.5. At the time of induction, cultures were supplemented with ferrous ammonium sulfate to a final concentration of 250 μM and growth was continued for an additional 14 h at 28 °C. Cells were harvested by centrifugation at 2683 x *g* for 20 min at 4 °C. The PDO proteins were purified as follows: The cell pellet from a 3 L culture was re-suspended in 500 mL of 50 mM Tris buffer, pH 8, containing 0.5 M NaCl (Buffer A), 0.1% Tween 20, 1 tablet of protease inhibitor cocktail (Roche) and 100 mg of lysozyme (Sigma). DNase (50 mg) and $MgCl_2$ (10 mM final concentration) were added to the cell suspension and stirred at 4 °C for 60 min followed by sonication on ice with the following pulse sequence: 30 sec burst, 1 min rest for a total burst time of 5 min at a power output setting of 6. The resulting sonicate was centrifuged at 8217 x *g* for 15 min at 4 °C. The resulting supernatant was diluted to a final volume of 1 L with Buffer A and loaded onto a 20 mL Ni-NTA column equilibrated with the same buffer. The column was washed with Buffer A, 20 mM imidazole (500 mL). PDO was eluted from the column with a linear gradient ranging from 20-500 mM imidazole. Protein containing fractions were pooled, concentrated, and dialyzed overnight against 50 mM Tris, pH 8.0, 0.25 M NaCl (4 L) and stored at -80 °C. Protein concentration was determined using the Bradford reagent with BSA standards.

**2.3.4 Metal analysis**

Iron content was measured using a colorimetric assay described by Fischer and Price (17). Briefly, the protein (10-50 μM) was denatured with 0.5 N HCl and 5% (w/v) trichloroacetic acid, mixed for 30 s and subsequently centrifuged for 10 min at 16,000 x *g* in a microcentrifuge. To determine the total iron content, the supernatant (700 μL) was mixed with 300 μL of a 1:2:1 mixture of 4 mM 2,4,6-tripyridyl-S-triazine (TPTZ), 50 % ammonium acetate, and 10 % hydroxylamine chloride, and incubated at room temperature for 5 min. Absorbance of the

resulting Fe(II)-TPTZ complex as measured at 596 nm. The concentration of Fe was calculated using an extinction coefficient of 22,600$M^{-1}$ $cm^{-1}$ for the Fe(II)-TPTZ complex (17).

### 2.3.5 Thermal stability assay

Wild-type and mutant PDO thermal stabilities were evaluated as described previously (10) by monitoring the increase in absorbance at 600 nm with increasing temperature. For this, enzyme (100 μg) in Buffer A (final volume 200 μl) was placed in a cuvette housed in a Cary 100 Bio UV/visible spectrophotometer equipped with a heating block connected to a water bath. The temperature was increased from 25-70 °C in 5 °C increments.

### 2.3.6 Preparation of glutathione persulfide

GSSH was prepared anaerobically as described previously (10) by the reaction of oxidized glutathione (GSSG) with sodium sulfide ($Na_2S$) in a Coy anaerobic chamber (atmosphere of 95:5 $N_2$:$H_2$) (Eq. 2.2).

$$GSSG + Na_2S \rightarrow GSSH + GSH \qquad [2.2]$$

Briefly, solid $Na_2S$ was added in 4-fold excess, to an anaerobic solution of 50 mM GSSG in 350 mM sodium phosphate, pH 7.4 (final volume 5 mL). The reaction vial was immediately sealed to prevent loss of $Na_2S$ and incubated at 37 °C for 25-30 min. The concentration of GSSH was measured using the cold cyanolysis method as described previously (18).

### 2.3.7 Oxygen consumption assay

The PDO activity of the mutants was measured as described previously (10). The reaction mixture consisted of 100 mM sodium phosphate, pH 7.4, and 0.5-170 μg of enzyme (final volume 1.6 mL) mixed in a Gilson-type chamber containing a Clark oxygen electrode and a magnetic stir bar. The reaction was initiated by addition of GSSH. The GSSH concentration was

varied from 0.02-4.0 mM to determine the dependence of enzyme activity on substrate concentration. All reactions were performed at room temperature (22 °C).

## 2.4 Results

### 2.4.1 Purification of wild-type and mutant PDOs

The recombinant proteins were purified using a one-step protocol and obtained with a purity of >95% (Fig. 2.1A). The protein migrates on SDS-PAGE with a molecular mass of ~25 kDa band, which is consistent with its predicted molecular weight size of 27 kDa. Protein preparations of L55P, T136A, C161Y and R163W yielded 65, 21, 40 and 53 mg, respectively from 3 L cultures.

### 2.4.2 Stability of wild-type and mutant PDOs

The thermal denaturation profiles for the mutant PDOs revealed altered stability compared to wild-type enzyme (Fig. 2.1B) with R163W being least impacted with a $T_m$ of 53 ± 2 °C compared to 64 ± 5 °C for wild type enzyme. The L55P and T136A mutants displayed similar thermal stabilities, with $T_m$s of 47 ± 6 °C and 44 ± 2 °C, respectively. The C161Y mutation was the most destabilizing with a $T_m$ of 38 ± 3 °C.

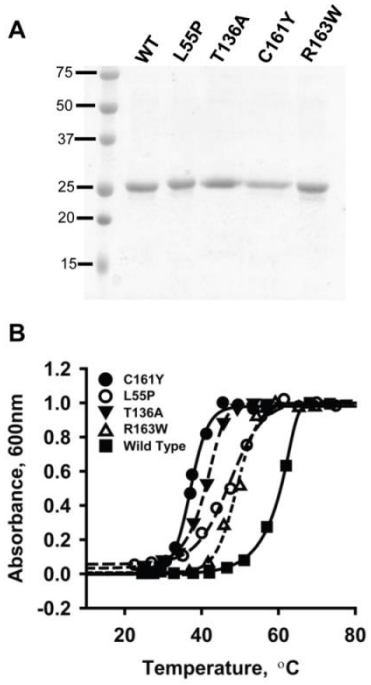


**Figure 2.1 Properties of PDO mutants.** *A*, The purity of wild-type and mutant PDOs (5 μg each) was evaluated by SDS-PAGE analysis and estimated to be >90%. *B*, Thermal denaturation curves for C161Y (solid circles), L55P (open circles), T136A (solid triangles), R163W (open triangles) and wild-type PDO (solid squares). Protein denaturation was monitored by the increase in absorbance at 600 nm as described under Experimental Procedures. The data are representative of three independent experiments.

### 2.4.3 Metal Analysis

The iron content of wild-type and mutant PDOs was determined using the 2,4,6-TPTZ based colorimetric method (17). Of the mutants, T136A displayed the highest iron content (0.58 mol Fe/mol enzyme) compared to wild-type PDO (0.82 mol Fe/mol enzyme) (Table 2.2). The R163W mutant displayed 3-fold lower iron while the C161Y and L55P displayed ~11-fold lower iron content than wild-type PDO. Attempts at reconstituting the PDO iron sites with FeCl2 to obtain full iron occupancy were unsuccessful.

TABLE 2.2. **Comparison of kinetic properties for wild-type and mutant PDOs**[a]

| Enzyme | Iron Content *mol Fe/mol Enzyme* | $V_{max}$ *μmol min$^{-1}$ mg$^{-1}$* | $K_m$ (GSSH) *mM* | $k_{cat}$ *s$^{-1}$* | $k_{cat}/K_m$ *mM$^{-1}$ s$^{-1}$* |
|---|---|---|---|---|---|
| Wild type* | 0.82 ± 0.05 | 113 ± 4 | 0.34 ± 0.03 | 47 | 140 |
| L55P | 0.078 ± 0.005 | 6.3 ± 0.8 | 0.86 ± 0.07 | 2.8 | 3.3 |
| T136A | 0.58 ± 0.02 | 1.7 ± 0.2 | 1.1 ± 0.3 | 0.8 | 0.7 |
| C161Y | 0.073 ± 0.001 | 5.8 ± 0.5 | 1.2 ± 0.2 | 2.6 | 2.2 |
| R163W | 0.27 ± 0.04 | 12.9 ± 0.8 | 0.73 ± 0.09 | 5.6 | 7.6 |

[a]The kinetic parameters were determined by monitoring $O_2$ consumption in the presence of GSSH at 22 ˚C in 100 mM sodium phosphate at pH 7.4, as described under Experimental Procedures. *The values for wild-type PDO have been reported previously (10).

### 2.4.4 Kinetic characterization of PDO mutants

The rate of oxygen consumption during enzyme-catalyzed oxygenation of GSSH to sulfite (Eq. 1) was monitored using an oxygen electrode (Fig. 2.2). The PDO mutants displayed varying effects on specific activity, which was lowered and on $K_m$, which was increased, compared to wild-type PDO (Table 2.2). The R163W mutant was the least impacted and exhibited an ~9-fold decrease in specific activity and a 2-fold increase in $K_m$. The T136A mutant was most impacted displaying a 66-fold decrease in specific activity and a 3.2-fold increase in $K_m$ resulting in a 200-fold decrease in $k_{cat}/K_m$.

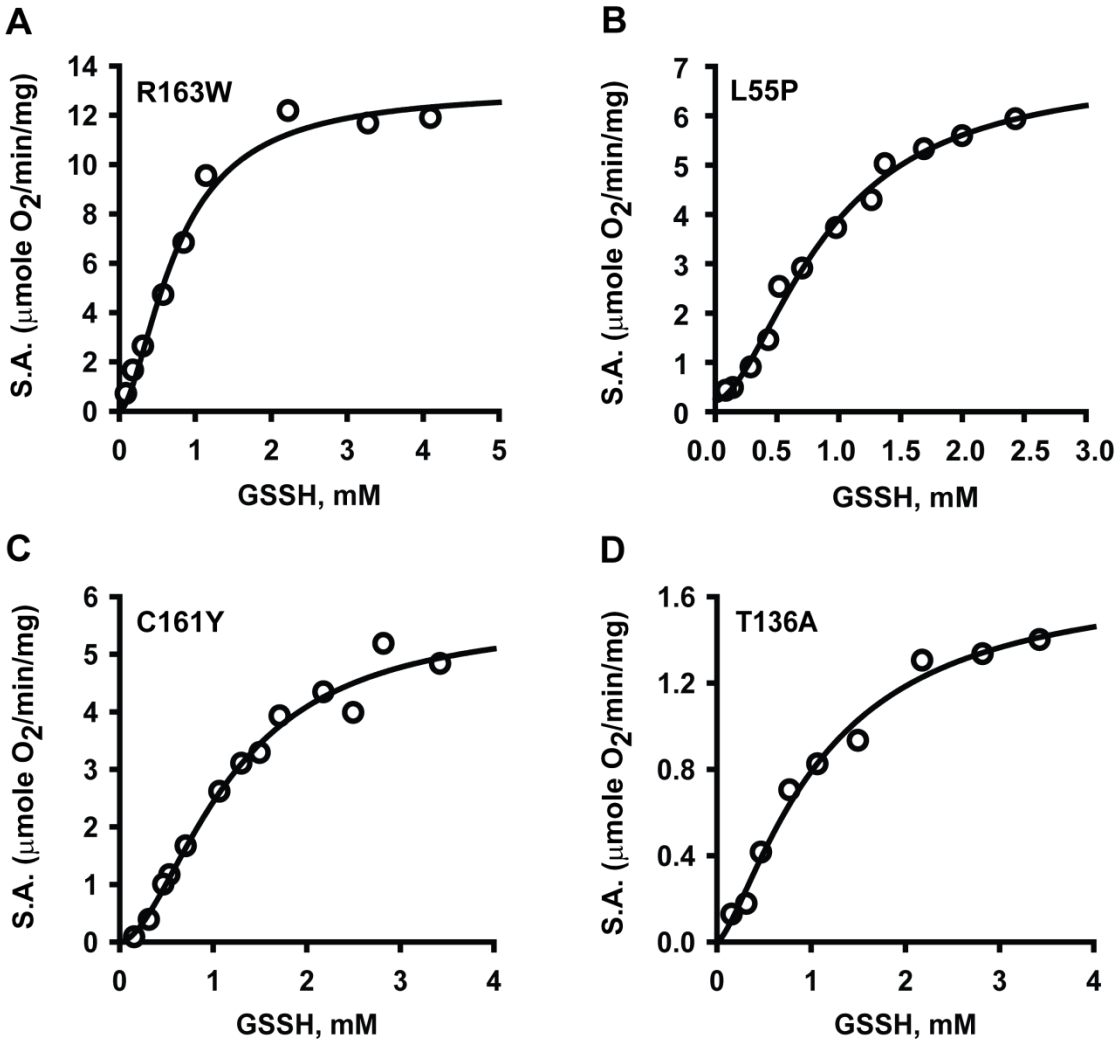


**Figure 2.2 Kinetic analysis of PDO activity.** The dependence of PDO activity on GSSH concentration for *A*, R163W, *B*, L55P, *C*, C161Y and *D*, T136A PDO. Oxygen consumption by PDO in 100 mM sodium phosphate buffer, pH 7.4, was monitored at 22 °C in the presence of varying concentrations of GSSH. The data are representative or three independent experiments. Data were fitted with the Hill equation as described under Experimental Procedures.

### 2.5 Discussion

Over 20 missense mutations in PDO have been identified in EE patients (3,5,7). The majority of these mutations are clustered near the iron binding ligands and the substrate pocket (12). In this study, we investigated three mutations (T136A, C161Y and R163W) that are proximal and one that is distal from the active site pocket (L55P) (Fig. 2.3A). Overall, these

mutations resulted in decreased iron content, thermal stability and altered kinetics. In the human PDO structure, Thr136 is located immediately downstream of the iron coordinating ligand, His135 (Fig. 2.3B). It participates in hydrogen bonding interactions with the backbone amide groups of Gly138 and Cys139, which likely aid in stabilizing the loop and positioning His135 for iron coordination. Additionally, Thr136 participates in a hydrogen-bonding network that stabilizes an adjacent loop in the β-sheet core. The T136A mutation would likely disrupt this network and lead to destabilization of the loops causing displacement of H135 and loss of iron. Surprisingly, the iron content of the T136A mutant was 70% that of wild-type PDO, but its kinetic parameters were severely impacted (Table 2).

Leu55 is located on a loop 16.6 Å away from the active site iron (Fig. 2.3C). Both upstream and downstream of Leu55, several residues are involved in a hydrogen-bonding network that are involved in positioning the iron coordinating residue, His79. Therefore, mutation of Leu55 to proline is predicted to cause perturbations originating from the third coordination sphere of iron. The mutation leads to 10% iron content compared to wild-type PDO and a >40-fold decrease in $k_{cat}/K_m$, with most of the loss in catalytic efficiency expressed on $k_{cat}$.

Cys161 is located on the same loop as the iron coordinating ligand, Asp154, and its backbone carbonyl is hydrogen bonded to Arg214 (Fig. 2.3D). Mutation of Cys161 to the larger tyrosine residue is expected to lead to loss of the hydrogen bonding interaction with Arg214 and to steric clashes with Phe222 and Met226 on the adjacent α-helix (Fig. 2.3D). It likely that the mutation would result in repositioning of the loop to accommodate the tyrosine and perturb proper positioning of Asp154 needed for iron coordination and Arg163 needed for substrate binding. The mutant shows significant loss of iron (10% of wild-type) and a 3.5-fold higher $K_m$ for the substrate.

Arg163 is located near the iron and is downstream of the iron ligand Asp154. Arg163 participates in hydrogen-bonding interactions with Asp165 and Ser230 and is implicated in substrate binding (Fig. 2.3E). Modeling of GSSH in the human PDO structure and the crystal structure of *Pseudomonas putida* PDO in complex with GSH both suggest that Arg163 is within hydrogen-bonding distance of the carboxyl group in the glutamate moiety of GSSH (12,16). Mutation of Arg163 to tryptophan is predicted to result in a conformational change to accommodate the bulkier side chain and reposition the upstream iron binding ligand Asp154. The mutation decreases iron content to 33% of wild-type PDO, increases the $K_m$ for GSSH ~2-fold and decreases $k_{cat}$ ~10-fold. A previous study on the R163W mutation reported reduced thermal stability and specific activity as found in our study, and also, a significantly lower iron reduction potential (14). The sensitivity to iron oxidation would be increased in the R163W mutant as a result of its ~100 mV more negative redox potential, further impacting PDO activity. Changes in the iron reduction potential might also be true of the other PDO mutations characterized in this study explaining the greater magnitude of decrease in their specific activities (~9-66-fold) compared to their decrease in iron content (1.4-11-fold) (Table 2.2).

The lower catalytic efficiency of the mutants helps explain the metabolic profile observed in EE patients and in *ethe1*$^{-/-}$ mice where $H_2S$ and thiosulfate levels are increased (5,8). Loss of

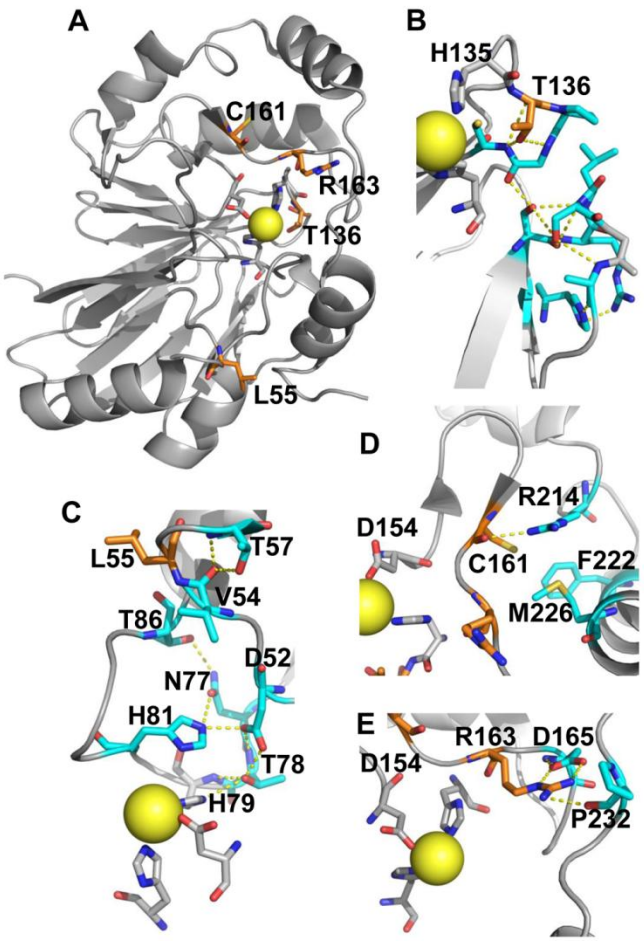


**Figure 2.3. Structural analysis of PDO mutations**. The structure of human PDO (PDB ID: 4CHL) was use to map the locations of PDO mutations characterized in this study. *A*, Iron (yellow sphere) ligands (His79, His135 and Asp154) that form the 2-His-1-Asp facial triad are shown in stick representation. The location of the four residues that are mutated in patients, Leu55, Thr136, Cys161 and Arg163, (orange) are shown in stick representation. *B*, Close-up showing the side chain interctions of Thr136, which would be lost in the T136A mutation. The hydroxyl group of threonine interacts with the backbone amides of Gly138 and Cys139 stabilizing the loop and participates in a hydrogen bond network that stabilizes an adjacent loop. These interactions are likely important for positioning His135 and stabilizing part of the β-sheet core of the protein. *C*, Close-up of Leu55 displays interactions that would potentially be lost due to the L55P mutation. Residues upstream (Val54 and Asp52) and downstream (Thr57, Asn77, Thr78, H81 and Thr86) of Leu55 participate in a hydrogen-bonding network that interacts with the iron ligand His79. This network is likely important for positioning the His79 residue. *D*, Close-up of Cys161 reveals that its backbone carbonyl participates in a hydrogen bond with the side chain of Arg214, which likely stabilizes the loop and helps position Asp154. *E*, Close-up of Arg163 reveals that it is engaged in hydrogen bonding interactions with the backbone carbonyl of Pro232 and the carboxylate oxygens of Asp165. This network is likely important for stabilizing and positioning the loop of Asp154.

PDO activity might lead to a redirection of the sulfide oxidation pathway towards thiosulfate production as competition for GSSH between rhodanese ($8.60 \times 10^5$ $M^{-1}$ $s^{-1}$) and PDO ($1.40 \times 10^5$ $M^{-1}$ $s^{-1}$ for wild type enzyme) would further favor the former. The $k_{cat}/K_m$ values for the mutants are significantly lower ($0.7\text{-}7.6 \times 10^3$ $M^{-1}$ $s^{-1}$) than wild-type PDO. Under PDO deficiency conditions, it is expected that the sulfide oxidation pathway would eventually stall due to decreased production of sulfite, which is needed for thiosulfate formation by rhodanese. Under these conditions, $H_2S$ levels would increase due to the reactivity of GSSH, forming GSSG and $H_2S$. The increase in $H_2S$ levels would inhibit cytochrome c oxidase and consequently, SQR leading to further accumulation of $H_2S$ (19,20). The observed increased in thiosulfate in EE levels could also result from enhanced $H_2S$ oxidation by hemeproteins, which catalyze its conversion to thiosulfate (21,22).

In summary, we have shown that four of the PDO missense mutations identified in EE patients adversely impacted the iron content, thermal stability and kinetic properties of the enzyme. Examination of the PDO structure suggests that the functional consequences of these mutations are due to perturbations in the positioning and interactions of the iron ligands and in the case of R163W, to additionally affecting substrate binding. The observed biochemical profile of EE can be explained by a shift in the partitioning of the substrate GSSH produced in the first step in the sulfide oxidation pathway, towards rhodanese and thiosulfate production due to reduced competition from PDO resulting in increased thiosulfate and eventually, to a buildup of $H_2S$ levels.

## 2.6 References

1. Burlina, A., Zacchello, F., Dionisi-Vici, C., Bertini, E., Sabetta, G., Bennet, M. J., Hale, D. E., Schmidt-Sommerfeld, E., and Rinaldo, P. (1991) *Lancet* **338**, 1522-1523

2. Garcia-Silva, M. T., Campos, Y., Ribes, A., Briones, P., Cabello, A., Santos Borbujo, J., Arenas, J., and Garavaglia, B. (1994) *J Pediatr* **125**, 843-844

3. Tiranti, V., Briem, E., Lamantea, E., Mineri, R., Papaleo, E., De Gioia, L., Forlani, F., Rinaldo, P., Dickson, P., Abu-Libdeh, B., Cindro-Heberle, L., Owaidha, M., Jack, R. M., Christensen, E., Burlina, A., and Zeviani, M. (2006) *J Med Genet* **43**, 340-346

4. Mineri, R., Rimoldi, M., Burlina, A. B., Koskull, S., Perletti, C., Heese, B., von Dobeln, U., Mereghetti, P., Di Meo, I., Invernizzi, F., Zeviani, M., Uziel, G., and Tiranti, V. (2008) *J Med Genet* **45**, 473-478

5. Tiranti, V., D'Adamo, P., Briem, E., Ferrari, G., Mineri, R., Lamantea, E., Mandel, H., Balestri, P., Garcia-Silva, M. T., Vollmer, B., Rinaldo, P., Hahn, S. H., Leonard, J., Rahman, S., Dionisi-Vici, C., Garavaglia, B., Gasparini, P., and Zeviani, M. (2004) *Am J Hum Genet* **74**, 239-252

6. Tiranti, V., Viscomi, C., Hildebrandt, T., Di Meo, I., Mineri, R., Tiveron, C., Levitt, M. D., Prelle, A., Fagiolari, G., Rimoldi, M., and Zeviani, M. (2009) *Nat Med* **15**, 200-205

7. Valente, L., Piga, D., Lamantea, E., Carrara, F., Uziel, G., Cudia, P., Zani, A., Farina, L., Morandi, L., Mora, M., Spinazzola, A., Zeviani, M., and Tiranti, V. (2009) *Biochim Biophys Acta* **1787**, 491-501

8. Hildebrandt, T. M., and Grieshaber, M. K. (2008) *FEBS J* **275**, 3352-3361

9. Mishanina, T. V., Libiad, M., and Banerjee, R. (2015) *Nat Chem Biol* **11**, 457-464

10. Kabil, O., and Banerjee, R. (2012) *J Biol Chem* **287**, 44561-44567

11. Kabil, O., and Banerjee, R. (2012) *J Biol Chem* **287**, 44561-44567

12. Pettinati, I., Brem, J., McDonough, M. A., and Schofield, C. J. (2015) *Hum Mol Genet* **24**, 2458-2469

13. Pettinati, I., Brem, J., Lee, S. Y., McHugh, P. J., and Schofield, C. J. (2016) *Trends Biochem Sci* **41**, 338-355

14. Henriques, B. J., Lucas, T. G., Rodrigues, J. V., Frederiksen, J. H., Teixeira, M. S., Tiranti, V., Bross, P., and Gomes, C. M. (2014) *PLoS One* **9**, e107157

15. McCoy, J. G., Bingman, C. A., Bitto, E., Holdorf, M. M., Makaroff, C. A., and Phillips, G. N., Jr. (2006) *Acta Crystallogr D Biol Crystallogr* **62**, 964-970

16. Sattler, S. A., Wang, X., Lewis, K. M., DeHan, P. J., Park, C. M., Xin, Y., Liu, H., Xian, M., Xun, L., and Kang, C. (2015) *J Biol Chem* **290**, 18914-18923

17. Fischer, D. S., and Price, D. C. (1964) *Clin Chem* **10**, 21-31

18. Wood, J. L. (1987) *Methods Enzymol* **143**, 25-29

19. Libiad, M., Yadav, P. K., Vitvitsky, V., Martinov, M., and Banerjee, R. (2014) *J Biol Chem* **289**, 30901-30910

20. Di Meo, I., Fagiolari, G., Prelle, A., Viscomi, C., Zeviani, M., and Tiranti, V. (2011) *Antioxid Redox Signal* **15**, 353-362

21. Vitvitsky, V., Yadav, P. K., An, S., Seravalli, J., Cho, U. S., and Banerjee, R. (2017) *J Biol Chem* **292**, 5584-5592

22. Bostelaar, T., Vitvitsky, V., Kumutima, J., Lewis, B. E., Yadav, P. K., Brunold, T. C., Filipovic, M., Lehnert, N., Stemmler, T. L., and Banerjee, R. (2016) *J Am Chem Soc* **138**, 8476-8488

# Chapter 3

## Sulfur Transfer and Oxidation Catalyzed by a Persulfide Dioxygenase-Rhodanese Fusion Protein

The contents of this chapter have been submitted to the Journal of Biological Chemistry.

Citation:

Motl, N., Skiba, M. A., Kabil, O., Smith, J., L., Banerjee, R. (2017) *submitted to J Biol Chem.*

### 3.1 Abstract

Hydrogen sulfide is a signaling molecule, which is toxic at elevated concentrations. In eukaryotes, its clearance occurs via a mitochondrial sulfide oxidation pathway, which comprises sulfide quinone oxidoreductase, persulfide dioxygenase (PDO), rhodanese and sulfite oxidase and converts $H_2S$ to thiosulfate and sulfate. Natural fusions between the non-heme iron containing PDO and rhodanese, a thiol sulfurtransferase, exist in some bacteria. Herein, we report the kinetic properties and the crystal structure of a PDO-rhodanese fusion protein, (PRF), from *Burkholderia phytofirmans*. The crystal structures of wild-type PRF and of the sulfurtransferase-inactivating C314S mutant with and without glutathione bound were determined at 1.8, 2.4, and 2.7 Å resolution, respectively. The two active sites are distant and do not show evidence of direct communication. The *B. phytofirmans* PRF exhibited robust PDO activity and preferentially catalyzed sulfur transfer in the direction of thiosulfate to sulfite and glutathione persulfide; sulfur transfer in the reverse direction, i.e. leading to thiosulfate formation, was not detectable. Together with the kinetic data, our bioinformatics analysis reveals

that PRF is poised to metabolize thiosulfate to sulfite and is involved in a sulfur assimilation pathway rather than in sulfide stress response as seen with the *Staphylococcus aureus* PRF or in sulfide oxidation and disposal as seen with the homologous proteins in mammals.

### 3.2 Introduction

Hydrogen sulfide ($H_2S$) is a gas with toxicity comparable to that of cyanide (1). It is also a signaling molecule produced by prokaryotes and eukaryotes and elicits a broad range of physiological effects (2-4). Notably, it acts as a cardioprotectant during myocardial ischemia reperfusion and is implicated in regulation of the cellular stress response, apoptosis, and inflammation (5-8). Steady-state $H_2S$ levels are governed by the rates of its production and clearance (9). In eukaryotes, $H_2S$ is produced by the transsulfuration pathway enzymes, cystathionine β-synthase and cystathionine γ-lyase, and by the cysteine catabolic pathway enzyme, mercaptopyruvate sulfurtransferase (10,11). Sulfide clearance occurs primarily via the mitochondrial sulfide oxidation pathway (12,13). Several enzymes are involved in the mitochondrial sulfur oxidation pathway: sulfide quinone oxidoreductase, the persulfide dioxygenase (PDO, also known as ETHE1), rhodanese, and sulfite oxidase. The main products of the sulfide oxidation pathway are thiosulfate and sulfate. PDO is a member of the 2-His-1Asp mononuclear iron containing enzyme superfamily and catalyzes the oxidation of glutathione persulfide (GSSH) to sulfite (14,15). Mutations in PDO result in ethylmalonic encephalopathy, an autosomal recessive disorder (16). Over 20 mutations have been described in the *ethe1* gene (17). Rhodanese is a thiosulfate sulfurtransferase; in humans, it preferentially catalyzes sulfur transfer from GSSH to sulfite producing thiosulfate and GSH (Eq. 3.1) (18).

$$GSSH + SO_3^{2-} \rightarrow GSH + S_2O_3^{2-} \qquad [3.1]$$

Rhodanese domains are universal structural modules that occur in one of three variations (19). They can be found as tandem repeats as in human rhodanese, which possesses a non-catalytic N-terminal domain and a catalytically active C-terminal domain (18,20). Alternatively, they can be found as a single domain in proteins such as human TSTD1 (21) and *E. coli* GlpE (22), or as natural fusions with other protein domains as in the *S. aureus* CstB (23). In prokaryotes, $H_2S$ can be generated via several pathways. It is an end product of the dissimilatory sulfate reducing pathway in which sulfate is used as a terminal electron acceptor during anaerobic respiration (24). $H_2S$ is an intermediate in the assimilatory sulfate-reducing pathway where it is produced from sulfite by sulfite reductase and is used as a substrate for cysteine synthesis (25). Additionally, $H_2S$ can be produced by orthologs of the eukaryotic $H_2S$ biosynthetic enzymes cystathionine β-synthase and cystathionine γ-lyase and mercaptopyruvate sulfurtransferase, which have been identified in several bacterial species and suggested to play a role in defense against antibiotic-induced oxidative stress (26). $H_2S$ metabolism by prokaryotes combined with its toxicity at high concentrations, necessitates mechanisms for regulating its levels (27). The sulfide anion efflux transporter described in *Clostridium difficile* represents one mechanism for clearing sulfide via export (28). Additionally, several bacterial species possess orthologs of the eukaryotic mitochondrial sulfide oxidation pathway enzymes, and presumably dispose of oxidation products of sulfide (23,29,30).

Recently, bacterial proteins that are natural fusions between PDO and rhodanese have been identified (23). Hereafter, we refer to these fusion proteins as PRF (for *P*DO *r*hodanese *f*usion). Bioinformatics analysis reveals that in a subset of these PRFs, e.g. the one from *Burkolderia phytofirmans PsJN*, the PDO domain is fused to a single rhodanese domain, which is orthologous to human thiol sulfurtransferase, TSTD1 and distinct from the two-domain human

rhodanese (Fig. 3.1A). In another subset, exemplified by CstB (23), the PDO domain is fused to two rhodanese domains (Fig. 3.1A). Of these, the first (or middle) rhodanese domain is non catalytic while the second (or C-terminal) domain houses the sulfurtransferase activity and, as in the case of CstB, oxidizes bacillithiol persulfide and coenzyme A persulfide to thiosulfate (23,30). CstB is implicated in protecting against persulfide stress and $H_2S$ toxicity (23).

The existence of PRFs in nature suggests that their mitochondrial homologs, which exist as stand-alone proteins, might interact. Structures of two PRFs are available from structural genomic projects. The first is of CstB (PDB ID: 3R2U) in which density for the catalytic rhodanese domain is missing. The second structure is of the biochemically uncharacterized *Alicyclobacillus acidocaldarius* PRF (PDB ID: 3TP9), which contains a PDO domain fused to two rhodanese domains. Interestingly, these structures reveal the presence of a cysteine-containing loop in the PDO active site that is absent in the human PDO structure and is not predicted in the sequence of *Bp*PRF. This additional loop is speculated to aid in substrate transfer from the PDO domain to the rhodanese domain (23).As CstB is the only PRF that has been characterized biochemically to date (23,30), there is a scarcity of information on the roles of PRFs in sulfur metabolism in bacteria.

In this study, we have characterized the PRF protein from *Burkolderia phytofirmans* (referred hereafter as *Bp*PRF), a gram-negative endophyte originally isolated from onion roots (31). In *Bp*PRF, the N-terminal nonheme Fe(II)-containing PDO domain is followed by a rhodanese domain containing the signature CRXGX(T/R) active site motif (Fig. 3.1B). Interestingly, this motif is more similar to that of sulfurtransferases containing two rather than one rhodanese domain. The N-terminal PDO domain of *Bp*PRF displays high sequence identity to human PDO (56%) and displays complete conservation of the active site iron binding ligands.

We demonstrate that *Bp*PRF is a bifunctional enzyme that uses the rhodanese domain to preferentially catalyze sulfur transfer from thiosulfate to GSH to form sulfite and GSSH and uses the PDO domain to oxidize GSSH to sulfite (Eqs. 3.2 and 3.3).

$$S_2O_3^{2-} + GSH \rightarrow SO_3^{2-} + GSSH \qquad [3.2]$$

$$GSSH + O_2 \rightarrow GSH + SO_3^{2-} \qquad [3.3]$$

The crystal structures of *Bp*PRF provide insights into the architecture and the relative juxtaposition of its active sites.

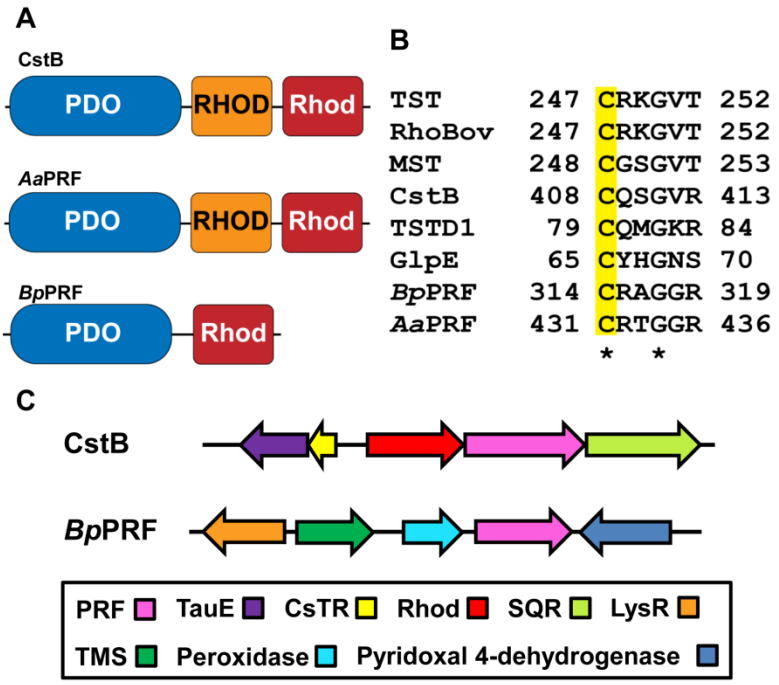


**Figure 3.1. Organization of *Bp*PRF and limited sequence comparison**. *A,* Domain organization of PRFs. PRFs form *S. aureus* (*Sa*PRF) and *A. acidocaldarius* (*Aa*PRF) have an N-terminal PDO domain, a non-catalytic rhodanese (RHOD) domain and a catalytic rhodanese (Rhod) domain. *Bp*PRF displays an N-terminal PDO domain and C-terminal catalytic rhodanese domain. *B,* Sequence alignment of rhodanese active site sequences from human (hTST) and bovine (RhoBov) rhodanese, human mercaptopyruvate sulfurtransferase (MST), *E. coli* single domain rhodanese (GlpE), human mitochondrial single-domain sulfurtransferase (TSTD1), *S. aureus* PRF (CstB), *B. phytofirmans* PRF (*Bp*PRF), *A. acidocaldarius* PRF (*Aa*PRF). The conserved active site cysteine is highlighted in yellow. *C,* Comparison of the genomic contexts of CstB (top) and *Bp*PRF (bottom). The operon encoding CstB (pink) includes a multi-domain rhodanese (CstA, red) and an SQR homolog (light green). The adjacent locus includes the polysulfide sensing repressor CsTR (yellow) and TauE (purple), a putative sulfite

permease/transmembrane sulfur compound exporter. The loci adjacent to *Bp*PRF (pink) include a putative peroxidase (cyan) and pyridoxal 4-dehydrogenase (blue), a putative transmembrane (TMS)-type transporter (dark green) and a putative LysR-type regulator (orange).

### 3.3 Experimental Procedures

#### 3.3.1 Materials

The sodium salts of sulfide, sulfite and thiosulfate, GSH, oxidized glutathione, *L*-cysteine, para-rosaniline hydrochloride and 2,4,6- tripyridyl-S-triazine were purchased from Sigma. FluoroPure grade monobromobimane was purchased from Life Technologies.

#### 3.3.2. Expression constructs for BpPRF

The cDNA encoding *Bp*PRF was amplified from genomic DNA isolated from *Burkholderia phytofirmans* PsjN (purchased from DSMZ, Braunschweig, Germany), using the following primers containing NdeI and HindIII restriction sites (bold font): forward 5′-TTAATT**CATATG** TTGATCTTCCG GCAGCTATTC-3′ and reverse 5′-TTAATT **AAGCTT**CTACACGCTGTTTTCAACGACGG-3′. The resulting PCR fragment was cloned into a pET28b vector. A C-terminal truncated *Bp*PRF (ΔC-*Bp*PRF) construct missing the last 4 residues (ΔC 354-357), was generated for cryastallography only, using the full-length *Bp*PRF expression construct as a template and the following primers containing NdeI and HindIII restriction sites (bold font): forward 5′TTAATT**CATATG**TTGA TCTTCCGGCAGCTATTC-3′ and reverse 5′-TTAATT**AAGCTT**CTATTCAACGA CGCGGCC-3′. The resulting PCR fragment was cloned into a pET28b vector. The, C314S mutant, was generated using the QuickChange kit (Stratagene) and the wild-type *Bp*PRF expression construct as a template. The isolated rhodanese domain was subcloned from the wild-type *Bp*PRF expression construct using the following primers containing NdeI and HindIII restriction sites (bold font): forward 5′-TTAATT**CATATG**ATGACCGAGCC CGATTTGGCG-3′ and reverse 5′-TTAATT**A**

**AGCTT**CTACTGCGTGGGGACGCTCGC-3′. The resulting PCR fragment was cloned into a pET28b vector.

### 3.3.3. Expression and purification of BpPRF

The recombinant *Bp*PRF protein was expressed in BL21 *E.coli*. A 200 mL culture in Luria Bertani medium was grown overnight at 37 $^{o}$C and used to inoculate a 4 × 1 L culture in the same medium. Cultures were grown at 28 °C and expression was induced with isopropyl-β-D-thiogalactopyrano-side (100 μM) when the optical density at 600 nm reached 0.5. Cultures were supplemented with ferrous ammonium sulfate at the time of induction to a final concentration of 250 μM and growth was continued for an additional 14 h at 28 °C. Cells were harvested by centrifugation at 2683 × *g* for 20 min at 4 °C.

*Bp*PRF was purified as follows. The cell pellet from a 4-liter culture was resuspended in 500 mL of 50 mM Tris buffer, pH 8, containing 0.5 M NaCl (Buffer A), 1 tablet of protease inhibitor cocktail (Roche) and 100 mg of lysozyme (Sigma). DNase (50 mg) and $MgCl_2$ (10 mM final concentration) were added to the cell suspension and stirred at 4 °C for 60 min followed by sonication on ice with the following pulse sequence: 30 sec burst, 1 min rest for a total burst time of 5 min at a power output setting of 6.The sonicate was centrifuged at 8217 × *g* for 15 min at 4 °C. The resulting supernatant was diluted 2-fold with Buffer A and loaded onto a 20 mL Ni-NTA column equilibrated with the same buffer. The column was washed with 500 mL of Buffer A containing 30 mM imidazole buffer. PRF was eluted from the column with a linear gradient ranging from 30-500 mM imidazole in Buffer A. Fractions containing the PRF protein were pooled, concentrated, and dialyzed overnight against 4 L of Buffer A and stored at -80 °C. Protein concentration was determined using the Bradford reagent (BioRad) with BSA as a

standard. The ΔC*Bp*PRF, the C314S mutant and the isolated rhodanese domain were purified using the same protocol.

### 3.3.4. Metal analysis

Plasma emission spectroscopy was used to analyze the total metal content of wild-type *Bp*PRF at the Chemical Analysis Laboratory (University of Georgia, Athens). Twenty metal ions are detected by this method. The iron content of the enzyme was also measured using a colorimetric assay described previously (32). This method allows for the direct measurement of total iron content, the Fe(II) content and consequently, estimation of the Fe(III) content of the enzyme. Briefly, *Bp*PRF (10-50 μM) was denatured with 0.5 N HCl and 5% (w/v) trichloroacetic acid (final volume 1 mL), mixed for 30 s and subsequently centrifuged for 10 min at 16,000 × *g* in a microcentrifuge. To determine the total iron content, the supernatant (700 μL) was mixed with 300 μL of a 1:2:1 mixture of 4 mM 2,4,6-tripyridyl-S-triazine, 50 % ammonium acetate, and 10 % hydroxylamine chloride, and incubated at room temperature for 5 min. Hydroxylamine was present to reduce residual Fe(III) to Fe(II). Absorbance of the resulting Fe(II)-2,4,6-tripyridyl-S-triazine complex was measured at 569 nm. The total Fe concentration was calculated using an extinction coefficient of 22,600 $M^{-1}$ $cm^{-1}$ for the Fe(II)-2,4,6-tripyridyl-S-triazine complex (32).

### 3.3.5. Molecular mass determination

Purified *Bp*PRF (5 ml of 3.7 mg/ml) was loaded onto a HiLoad™ 16/60 Superdex G-200 column equilibrated with Buffer A at 4 °C and calibrated with protein standards (Bio-Rad). The protein was eluted at a flow rate of 0.5 mL $min^{-1}$ and was monitored by absorbance at 280 nm.

### 3.3.6. Thermal denaturation assay

The thermal stability of *Bp*PRF and of the C314S rhodanese domain mutant was evaluated by monitoring the increase in absorbance at 600 nm with increasing temperature. For this, enzyme (100 μg) in Buffer A (final volume 200 μl) was placed in a cuvette housed in a Cary 100 Bio spectrophotometer equipped with a heating block connected to a water bath. The temperature was increased from 25-70 °C in 5 °C increments.

### 3.3.7. Preparation of GSSH

GSSH was prepared anaerobically as described previously (14) by reacting oxidized glutathione (GSSG) with $Na_2S$ in a Coy anaerobic chamber (atmosphere of 95:5 $N_2$:$H_2$) (Eq. 3.4).

$$GSSG + Na_2S \rightarrow GSSH + GSH \qquad [3.4]$$

Briefly, solid $Na_2S$ was added in 4-fold excess, to an anaerobic solution of 50 mM GSSG in 350 mM sodium phosphate, pH 7.4 (final volume 5 mL). The reaction vial was immediately sealed to prevent loss of $Na_2S$ and incubated at 37 °C for 25-30 min. The concentration of GSSH was measured using the cold cyanolysis method as described previously (14). Substrate was either used immediately or stored at -20 °C until use. Substrate concentration was measured both before freezing and after thawing prior to use in the enzyme assay. Cysteine persulfide was prepared using the same procedure.

### 3.3.8. Oxygen consumption assay

The PDO activity of *Bp*PRF was measured by monitoring $O_2$ consumption at room temperature (22 ˚C). The reaction mixture consisted of 100 mM sodium phosphate, pH 7.4, and 0.5-2 μg of enzyme (final volume 1.6 mL) mixed in a Gilson-type chamber containing a Clark oxygen electrode and a magnetic stir bar. The reaction was initiated by addition of GSSH (0.02-3 mM). The effects of GSH, $Na_2S$, sulfite and thiosulfate on the PDO activity were assessed at 5

mM concentrations of each except for sulfite, which was added to a final concentration of 0.6 mM. Cysteine persulfide was tested as an alternative substrate at a final concentration of 1 mM. The dependence of reaction velocity on $O_2$ concentration was determined as follows. The complete reaction mixture containing enzyme, the substrate GSSH and 100 mM phosphate pH 7.4 was prepared anaerobically in an inflatable glove chamber, Glove-Bag™ (Cole-Palmer), filled with nitrogen (concentration > 99%) and the reaction was started by injecting buffer with a known concentration of dissolved oxygen $O_2$ (generated using a 100% oxygen tank) to give the final $O_2$ concentrations ranging from 1.6-250 μM. $O_2$ concentration in oxygenated buffer was independently determined using the oxygen probe.

**3.3.9. Thiosulfate:cyanide sulfurtransferase assay**

The cyanide detoxification activity of *Bp*PRF was measured in a colorimetric assay as described previously (33). The reaction mixture contained 60 mM thiosulfate, 60 mM potassium cyanide and 5-10 μg protein in 200 mM sodium phosphate buffer, pH 7.4 (330 μL final volume). The reaction was initiated by addition of enzyme. After incubation for 20 min at 22 ˚C, the reaction was stopped by addition of 100 μL of 15 % (w/v) formaldehyde. Thiocyanate formation was measured by addition of 500 μL of a ferric nitrate solution containing 165 mM ferric nitrate nonahydrate and 13.3% (v/v) nitric acid. The absorbance of the resulting ferric thiocyanate complex was measured at 460 nm. The concentration of thiocyanate formed was determined using a standard curve. The concentrations of cyanide and thiosulfate were varied from 0.5-60 mM to determine the dependence of enzyme activity on substrate concentration.

**3.3.10. Thiosulfate:GSH sulfurtransferase activity monitored in a coupled assay**

The GSSH formed via the sulfur transfer activity of *Bp*PRF was measured by coupling to $O_2$ consumption during GSSH utilization by the PDO activity. For this, the reaction mixture

contained 30 mM thiosulfate, 30 mM GSH, 25-30 μg enzyme and 200 mM sodium phosphate buffer, pH 7.4 (final volume 1.6 mL) mixed in a Gilson-type chamber containing a Clark oxygen electrode at 22 °C. GSH and thiosulfate concentrations were varied from 0.3-30 mM to determine the dependence of enzyme activity on substrate concentration.

### 3.3.11. Thiosulfate:GSH sulfurtransferase activity monitored by sulfite formation

The thiosulfate:GSH sulfurtransferase activity of *Bp*PRF and of the isolated rhodanese domain was monitored by detecting sulfite formation using a modified version of the colorimetric assay described previously (34). The reaction mixture contained 45 mM thiosulfate, 45 mM GSH, 0.7-3 μg enzyme and 200 mM sodium phosphate buffer, pH 7.4 (final volume of 500 μL). The reaction was initiated by addition of enzyme. After 5 min of incubation at 22 ˚C, the reaction was stopped by the addition of 500 μL of 0.23 M $HgCl_2$. After centrifugation at 16,000 × *g*, for 1 min, the supernatant (125 μlL) was mixed with 1 ml of a *p*-rosaniline solution containing 2:1 0.04% *p*-rosaniline prepared in 0.72 M HCl (w/v):0.2% formaldehyde. The absorbance of the resulting *p*-rosaniline sulfonic acid complex was measured at 570 nm. The concentration of sulfite formed was determined using a standard curve. The concentrations of thiosulfate and GSH were varied from 0.3-50 mM to determine the dependence of enzyme activity on substrate concentration.

### 3.3.12. Thiosulfate:thiol sulfurtransferase activity monitored by $H_2S$ formation

The sulfurtransfer activities of *Bp*PRF and of the isolated rhodanese domain was measured by detecting $H_2S$ formation using the lead acetate assay described previously (18). The reaction mixture contained thiosulfate (0.5-25 mM) and either GSH (2-40 mM) or cysteine (1-50 mM) in 200 mM sodium phosphate buffer, pH 7.4 (final volume of 1 mL) and was pre-incubated at 37 °C for 10 min. The reaction was initiated by addition of 0.7-15 μg enzyme. Formation of

lead sulfide was measured at 390 nm and the concentration of $H_2S$ formed was calculated using an extinction coefficient of 5,500 $M^{-1}cm^{-1}$ for lead sulfide (18)

**3.3.13. GSSH:sulfite sulfurtransferase actvity**

The reactions were performed in a Coy anaerobic chamber to prevent oxidation of GSSH by the PDO domain. The standard reaction mixture contained 1 mM GSSH and 1 mM sulfite, 0.5-50 μg enzyme, and 20 mM sodium phosphate buffer, pH 7.4 (200 μL final volume). The derivatization reaction was initiated by the addition of enzyme. After 5 min of incubation, monobromobimane was added to a final concentration of 3 mM and incubated at room temperature for 15 min. The derivatization reaction was terminated by addition of 100 μL of 0.2 M sodium citrate, pH 2.0. Production of thiosulfate from GSSH and sulfite was monitored by HPLC. For this, a 60 mM stock solution of monobromobimane was prepared in DMSO and protected from light during preparation and handling. Bimane adducts of GSSH, $Na_2S$, GSH, sulfite, and thiosulfate, were prepared in 20 mM sodium phosphate, pH 7.4. Each standard (final concentration 250 μM) was incubated with a final concentration of 3 mM monobromobimane (200 μl final volume) for 10 min at 22 ˚C.

The derivatized samples were centrifuged at 10,000 × *g* for 10 min at 4 °C, and the supernatants were separated on a 4.6 × 150 cm C18 reverse phase HPLC column (3 μM packing, SunFire) using an Agilent 1100 series HPLC system equipped with a multi-signal fluorescence detector. The column was equilibrated with the following solution: 80 % solvent A (897.5 mL water, 100 mL methanol, and 2.5 mL acetic acid) and 20 % solvent B (97.5 mL water, 900 mL methanol, and 2.5 mL acetic acid). Samples (50 μL) were injected onto the column and resolved using the following gradient of solvent B: 20 % from 0-5 min, 20-45 % from 5-10 min, 45 % isocratic from 10-15 min, 45-50 % from 15-25 min, 50 % isocratic from 25-28 min, 50-100 %

from 28-30 min, 100 % isocratic from 30-39 min, 100-20 % from 39-42 min, 20 % isocratic from 42-48 min. The flow rate was 0.75 min/mL. Fluorescence of the bimane adducts was detected using 340 nm excitation and 450 nm emission. The concentration of thiosulfate was determined using the peak areas and a standard curve.

### 3.3.14. Stoichiometry of $O_2$ consumption and sulfite formation

The stoichiometry of coupling between the PDO and rhodanese active sites was monitored using wild-type and C314S *Bp*PRF as follows. The reaction mixture contained 1 mM GSSH, 75 nM enzyme, and 200 mM sodium phosphate buffer, pH 7.4 (1.6 ml final volume) in a Gilson-type chamber containing a Clark oxygen electrode. The reaction was initiated by addition of GSSH and $O_2$ consumption was recorded. After 5 min at 22 °C, an aliquot of the reaction mix (50 μl) was added to 60 mM monobromobimane (20 μl) to a final concentration of 17 mM. After incubation for 15 min at room temperature, the reaction was quenched with 100 μl of 0.2 M sodium citrate, pH 2.0. The derivatized samples were processed and separated by HPLC as described above to determine concentrations of sulfite formed and thiosulfate consumed

### 3.3.15. Reaction stoichiometry under single and multiple turnover conditions

The reaction stoichiometry of wild-type and C314S *Bp*PRF under single turnover conditions was monitored as described above with the following variation. The reaction mixture contained 250 μM thiosulfate, 250 μM GSH, and varying concentrations of enzyme (250, 125, 83, 62.5, 50 and 42 μM). The reaction was initiated by addition of GSH. After incubation for 30 min at 22 °C, an aliquot of the reaction mix (50 μL) was mixed with 20 μL of 60 mM monobromobimane and processed as described above. For analysis of the reaction stoichiometry under single turnover conditions in the absence of $O_2$, the enzymatic assay and derivatization reactions were performed in a Coy anaerobic chamber (atmosphere of 95:5 $N_2$:$H_2$).

### 3.3.16. Protein crystallization

The C-terminal truncated *Bp*PRF (ΔC*Bp*PRF) and C314S *Bp*PRF were crystallized by sitting drop vapor diffusion using 0.75 μL:0.75 μL protein stock:well solution. ΔC*Bp*PRF (5 mg/mL in 50 mM Tris, pH 8, 0.25 M NaCl, 10 % glycerol, 5 mM thiosulfate) crystallized in 3 days at 20 °C in the following conditions: 0.2 M zinc acetate, 0.1 M MES, pH 6, 10 % PEG-8000. A single rhombohedral rod-shaped crystal was harvested directly from the drop without cryoprotection and flash-cooled in liquid nitrogen. C314S *Bp*PRF (5 mg/mL in 50 mM Tris, pH 8.0, 0.25 M NaCl, 10% glycerol) crystallized in 2 days in the following conditions: (0.12 M NaCl, 0.1 M imidazole, pH 8.0, 25 % PEG-8000). To obtain structural data for C314S *Bp*PRF in complex with GSH, 5 mM GSH was added to the drop overnight. The hexagonal rod-shaped crystals were cryo-protected by passing harvested crystals through 2 μL of reservoir solution with an additional 15% glycerol followed by flash cooling with liquid nitrogen.

### 3.3.17. Data collection and crystal structure determination

Diffraction data were collected at the Advanced Photon Source (APS, Argonne National Laboratory) on the GM/CA beamline 23ID-D or 23ID-B (Table 3.1). For ΔC*Bp*PRF, data were collected on a single crystal to 1.79 Å resolution. For the apo- and GSH-soaked C314S *Bp*PRF crystals, data were collected to 2.49 and 2.09 Å, respectively. All data were processed using XDS (35). The truncated structure was solved by molecular replacement using BALBES (36) with the *Aa*PRF (PDB ID: 3TP9) as a search model. Phenix AUTOBUILD was used to build an ~70 % complete model. To complete the model, consecutive rounds of model building and refinement were performed using Coot (37) and PHENIX (38). The structures were validated using MolProbity (39). Electron density is complete for all *Bp*PRF residues except for eight in the linker region between the PDO and rhodanese domains and the N-terminal histidine tag.

TABLE 1. X-ray data collection and refinement statistics

| Data Collection<br>PDB ID | Wild-type PRF<br>5VE3 | C413S PRF-Apo<br>5VE4 | C413S PRF-GSH<br>5VE5 |
|---|---|---|---|
| Space group | $P2_12_12_1$ | $P6_522$ | $P6_522$ |
| Cell dimensions | | | |
| a,b,c (Å) | 63.7, 108.3, 119.6 | 84.5, 84.5, 549.4 | 83.5, 83.5, 547.6 |
| α, β, γ (°) | 90, 90, 90 | 90, 90, 120 | 90, 90, 120 |
| X-ray Source | APS 23ID-D | APS 23ID-B | APS 23ID-B |
| Wavelength (Å) | 1.033 | 1.033 | 1.033 |
| $d_{min}$ (Å) | 1.79 (1.86-1.79)[1] | 2.65 (2.75-2.65) | 2.35 (2.43-2.35) |
| R-merge | 0.119 (1.47) | 0.126 (1.35) | 0.126 (1.56) |
| Inner-shell R-merge | 0.045 (5.3 Å)[2] | 0.047 (7.8 Å) | 0.050 (7.0 Å) |
| Avg I/σ(I) | 14.6 (1.2) | 11.6 (1.7) | 11.0 (1.6) |
| Completeness (%) | 100 (96.0) | 100 (100) | 99.0 (99.0) |
| Multiplicity | 12.4 (9.0) | 8.6 (8.5) | 8.7 (9.2) |
| Total observations | 966,980 (67,309) | 303,925 (28,966) | 422,379 (43,869) |
| $CC_{1/2}$ | 0.999 (0.537) | 0.997 (0.898) | 0.998 (0.904) |
| CC* | 1.0 (0.836) | 0.999 (0.973) | 0.999 (0.975) |
| Refinement | | | |
| Data range (Å) | 41.26-1.79 | 43.94-2.65 | 41.75-2.35 |
| Reflections used in refinement | 77,982 (7,448) | 35,305 (3,392) | 48,680 (4,773) |
| $R_{work}/R_{free}$ (%) | 16.1/19.6 | 23.2/26.7 | 19.7/25.2 |
| Number of non-hydrogen atoms | 6051 | 8265 | 8471 |
| protein | 5538 | 8153 | 8154 |
| ligands | 2 | 24 | 74 |
| water | 511 | 88 | 189 |
| Amino acid residues | 698 | 1047 | 1048 |
| Deviation from ideality | | | |
| bond lengths (Å) | 0.013 | 0.003 | 0.007 |
| bond angles (°) | 1.20 | 0.70 | 0.97 |
| Average B-factor | 38.1 | 81.9 | 76.6 |
| macromolecules | 37.6 | 82.4 | 77.0 |
| ligands | 29.6 | 59.0 | 83.1 |
| solvent | 44.1 | 45.6 | 58.4 |
| Ramachandran plot | | | |
| favored (%) | 98.0 | 96.0 | 97.5 |
| allowed (%) | 2.0 | 4.0 | 2.3 |
| outliers (%) | 0 | 0 | 0.2 |

[1]Values in parentheses pertain to the outermost shell of data.
[2] $d_{min}$ inner shell

The C314S structure was solved via molecular replacement using Phaser within the Phenix software suite with the complete truncated model as a search model. Molecular replacement successfully placed two copies of the chain and the third was added in manually using Coot. Notably, a chloride ion sits in the place of the C314 persulfide in the C314S structure. The GSH-bound structure was solved via rigid body refinement in Phenix Refine. Electrostatic surface potentials were calculated using the APBS program in PYMOL (40-42). Figures were prepared using PYMOL(43). Authors N.M. and M.S. solved the crystal structures.

### 3.4. Results

#### 3.4.1. Purification and properties of BpPRF

Recombinant wild-type and variants of *Bp*PRF purified using a one-step protocol were obtained in >95% purity as judged by SDS PAGE analysis (not shown). The yield for the full-length proteins (wild-type and C314S), was ~120 mg protein per liter of culture. The rhodanese domain was obtained with a yield of 22 mg of protein per liter of culture. *Bp*PRF eluted from a size exclusion column with a molecular mass corresponding to 40 kDa, consistent with it being a monomer (predicted mass = 41.5 kDa). The rhodanese domain eluted as a mixture of a monomer and a dimer (not shown). The monomeric organization of *Bp*PRF is distinct from that of CstB, which is tetrameric (23).

The thermal stability of the *Bp*PRF variants was assessed in a turbidometric assay. The $T_m$ value for the isolated rhodanese domain (55 ± 2 °C) was slightly higher than for wild-type (50 ± 2 °C) and C314S (51.6 ± 0.8 °C) *Bp*PRF. This result indicates that the stand-alone rhodanese domain is well folded and contrasts with the instability of the catalytic rhodanese domain of CstB when it was expressed by itself (23).

#### 3.4.2. Metal Analysis

Plasma emission spectroscopy revealed the presence of 0.54 ± 0.07 mol iron/mol monomer wild-type *Bp*PRF. The metal content was also assessed by a colorimetric assay (32), which yielded a similar value (0.60 ± 0.03 mol iron/mol monomer). The iron content of C314S *Bp*PRF was 0.46 ± 0.02 mol iron/mol monomer (Table 3.2). Attempts to fully reconstitute the metal site with $FeCl_2$ under anaerobic conditions were unsuccessful.

### 3.4.3. Structure of BpPRF

The crystal structure of *Bp*PRF co-crystallized with thiosulfate, was obtained at 1.79 Å resolution by molecular replacement using the *Aa*PRF structure (PDB 3TP9) as template (Table 3.1). The final model contains two chains representing a crystallographic dimer in the asymmetrical unit. Each monomer consists of an N-terminal PDO domain (residues 1-230), a 15-residue linker (residues 231-245), and a C-terminal rhodanese domain (residues 246-357) (Fig. 3.2A). The PDO domain displays a typical metallo-β-lactamase-type fold consisting of two central β-sheets enclosed by three helices on each side (15,29,44). Density for eight of the fifteen residues in the linker region was missing, indicating that it is disordered (Fig. 3.2A). The C-terminal domain displays a characteristic rhodanese fold with a five stranded parallel β-sheet core framed by two α-helices on one side and three α-helices on the other side of the domain (45). Additionally, a β-hairpin extension is seen on the N-terminal side of the rhodanese domain (Fig. 3.2A). The two active sites are located at different ends of the protein, separated by a rotation angle of ~90° (Fig. 3.3A).

The PDO domain active site contains a mononuclear non-heme iron coordinated by His58, His114 and Asp133 comprising a 2His:1Asp facial triad. The remaining coordination sites are occupied by water molecules, which complete an octrahedral geometry around the

ferrous iron (Fig. 3.2B). Cys314 located in the rhodanese active site, was captured in its persulfidated, Cys-SSH

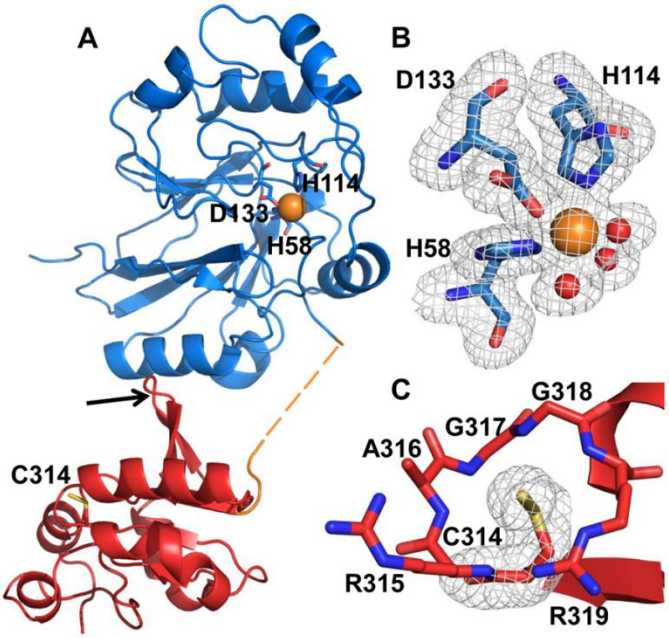


**Figure 3. 2**. **Crystal structure of *Bp*PRF.** The X-ray crystal structure of ΔC*Bp*PRF was solved at 1.79 Å resolution by molecular replacement using the *Aa*PRF structure (PDB ID: 3TP9) as a template. *A*, The structure of the *Bp*PRF monomer consists of an N-terminal PDO domain (blue), a fifteen residue linker region (orange) and a C-terminal rhodanese domain (red). The linker region lacked density for eight residues (dashed lines) suggesting a flexible, disordered state. The iron is shown as an orange sphere and ligands in the PDO domain and the active site cysteine, Cys314, in the rhodanese domain are shown in stick representation. The rhodanese domain β-hairpin extension is highlighted by the black arrow. *B*, close-up of the PDO active site with representative electron density (3.0σ Fo-Fc omit density in grey mesh) for side chains of His58, His114, Asp133 and three water molecules (shown as red spheres) coordinated to the iron center (orange sphere). *C*, Close-up of the rhodanese domain active site with representative electron density (3.0σ Fo-Fc omit density in grey mesh) for the Cys314 side chain displaying the additional density for the persulfide modification.

form (Fig. 3.2C). The PDO active site is located at the bottom of a large pocket (Fig. 3.3A) framed on one side by a positively charged ridge comprising residues Arg193-Lys216 and by Tyr176 on the other (Fig. 3.3B). The rhodanese active site is located at the bottom of a shallow pocket that is lined by the positively charged residues, Arg315 and Arg319 on one side, and hydrophobic residues Ala316, Gly317 and Gly318, on the other (Figs. 3.3C).

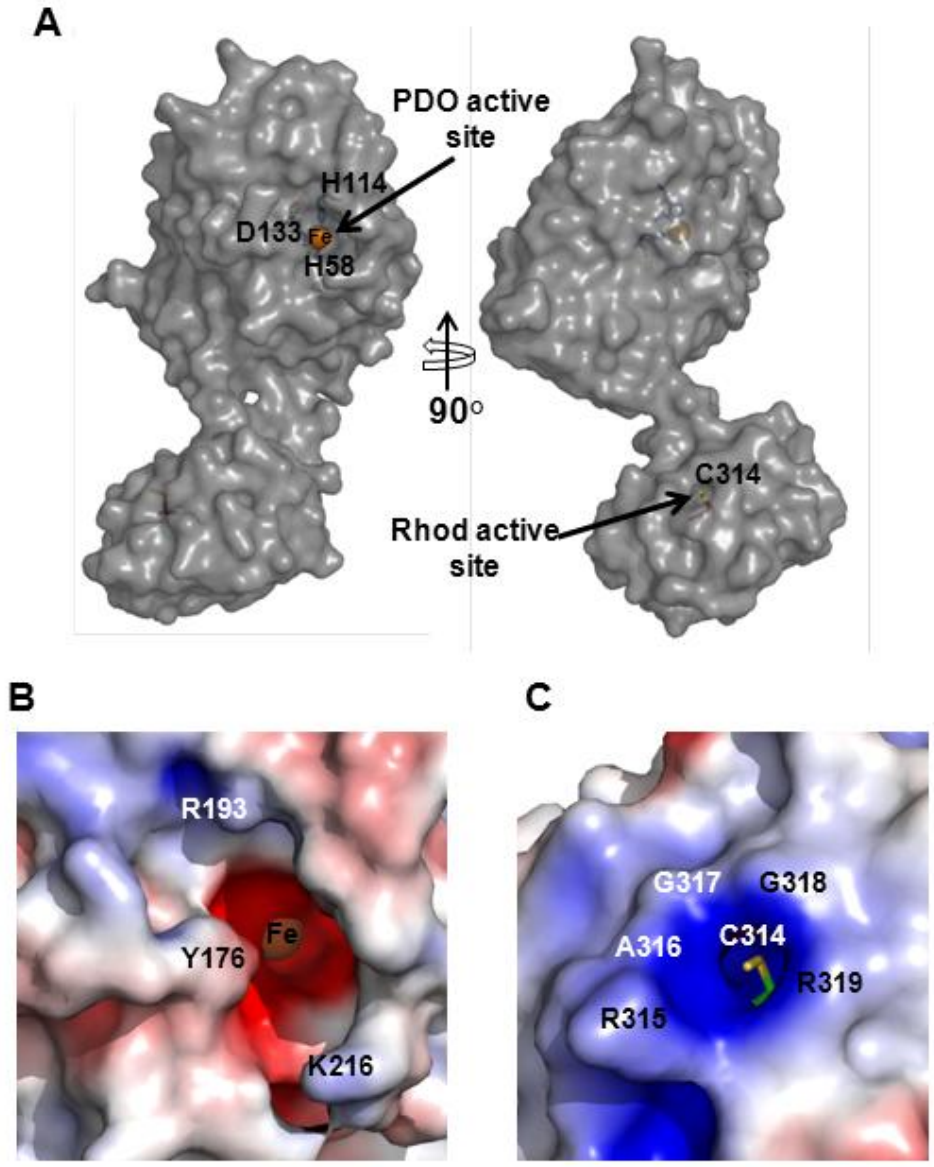


**Figure 3.3. Surface represenation of *Bp*PRF active sites.** *A,* Surface representation of *Bp*PRF displaying the PDO and rhodanese domain active site pockets located on different faces of the enzyme. The PDO domain iron is displayed as an orange sphere. The iron ligands and the catalytic cysteine are labeled. *B*, Close-up of the electrostatic surface around the PDO domain active site. The positively charged ridge of the active site contributed by residues Arg193-Lys216 and the polar Tyr176 frame the active site pocket and may play a role in substrate binding. *C*, close upof the rhodanese domain showning a mostly positive electrostatic surface potential . The active site cysteine is framed by positively charged and hydrophobic residues (Arg315, Ala316, Gly317, Gly318, Arg319). In B and C, blue and red denote positive and negative electrostatic potential and represent a range of -5 to +5 kT/e.

C314S *Bp*PRF crystallized in a different space group (Table 3.1) but in the same conformation as wild-type *Bp*PRF. Crystals of C314S *Bp*PRF that had been soaked with GSH, displayed additional density in two of the three chains present in the asymmetric unit. GSH coordinates to iron in the PDO active site and displaces one of the iron-coordinated waters. It is within hydrogen bonding distance of Tyr176, Arg193, Arg142 and Lys216 (Fig. 3.4A).

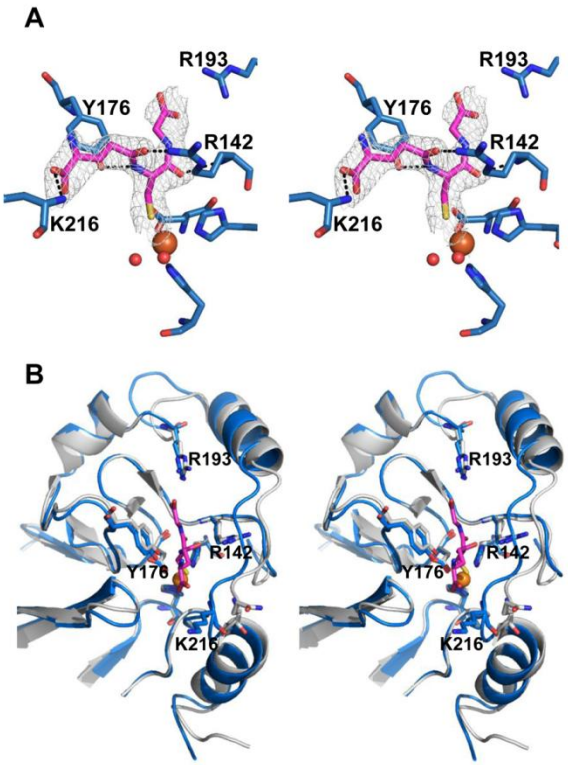


**Figure 3.4. Close up of the PDO active site of *Bp*PRF with GSH.** *A*, Stereo view of the C314S *Bp*PRF PDO domain with GSH bound. The surrounding residues that may participate in substrate binding and/or stabilization are shown with electron density (3.0σ Fo-Fc omit density in grey mesh) for GSH. Tyr176, Arg142, and Lys216 are hydrogen bonded (black dashes) to GSH. Two waters (red spheres) are coordinated to the iron center (orange sphere) in addition to the sulfur atom of GSH. *B*, Stereo veiw of C314S *Bp*PRF PDO domain (blue) in complex with GSH overlaid on human PDO (15) (PDB ID: 4CHL) (grey). GSH (shown in magenta) is displyed in stick representation. Conserved residues predicted to be involved in substrate binding, stabilization and/or positioning are Ty176, Arg193, Leu212, Arg142 and Pro215 (*Bp*PRF numbering).

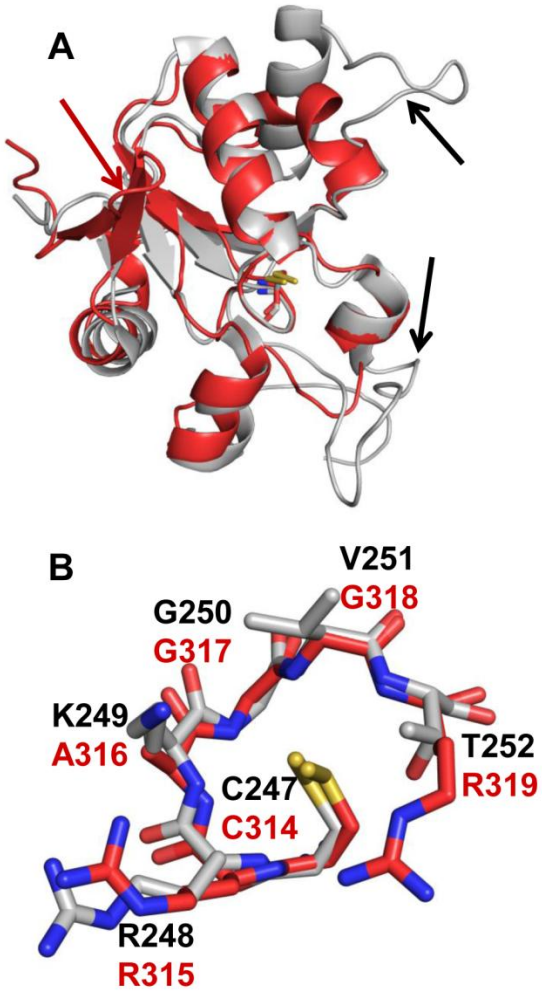


**Figure 3.5. Comparison of the *Bp*PRF rhodanese domain with bovine rhodanese.** *A*, Structural overlay of the *Bp*PRF rhodanese domain (red) with the catalytic domain of bovine rhodanese (PDB ID: 1RHD) (grey). The active site cysteine residues, C247 (bovine) and C314 (*Bp*PRF) are shown in stick representation A β-hairpin extension seen only in *Bp*PRF is highlighted by a red arrow. Two loop extensions seen only in bovide rhodanese, are highlighted by black arrows. *B*, structural overlay of the rhodanese active site loops from *Bp*PRF (red) and bovine rhodanese (grey).

### 3.4.4. Structural comparisons between BpPRF and homologous human proteins

The architecture of the *Bp*PRF PDO active site is very similar to that of human PDO (Fig. 3.4B). The substrate-binding pocket is framed by two α-helices on one side and by Tyr176 on the other. Key residues that are predicted to be involved in substrate binding in human PDO,

Tyr197, Arg214, Arg163, Leu231 and Pro234 are conserved in *Bp*PRF (Tyr176, Arg193, Arg142, Leu212 and Pro215) and are found in similar orientations. Lys216, which is not conserved in human PDO, lines the entrance to the active site and might play a role in substrate positioning.

The *Bp*PRF rhodanese domain and the catalytic domain of bovine rhodanese display very similar folds (Fig. 3.5A). Minor structural differences include the N-terminal β-hairpin extension in *Bp*PRF and two extra loops in bovine rhodanese. The active sites are also very similar with the conserved residues, Cys314, Arg315 and Gly318 (*Bp*PRF numbering), being in similar orientations (Fig. 3.5B). However, Thr252 and Lys249 in bovine rhodanese occupy the same positions as Arg319 and Ala316, respectively, in *Bp*PRF. These substitutions indicate differences in charge distribution that might contribute to differences in substrate specificity.

**3.4.5. PDO activity of BpPRF**

The rate of $O_2$ consumption during conversion of GSSH to sulfite (Eq. 3.3) was monitored using an $O_2$ electrode (Fig. 3.6 and yielded the following kinetic parameters for wild-type *Bp*PRF: $K_{m(GSSH)}$ = 70 ± 8 μM, and $K_{m(O2)}$ = 130 ± 30 μM and $k_{cat}$ = 143 $s^{-1}$ at 22 ˚C, (Table 3.2). C314S *Bp*PRF exhibited a 29-fold lower $k_{cat}$ and an ~5-fold higher $K_m$ for GSSH than wild-type *Bp*PRF. Addition of 2.5 mM ascorbate to the standard assay resulted in an ~20% increase in the PDO specific activity (not shown). Cysteine persulfide and thiosulfate were also tested as potential substrates for the PDO domain. However, neither displayed detectable activity.

It is important to note that the method used to synthesize GSSH results in its contamination with an equal concentration of GSH and an ~3-fold excess of $H_2S$, as described previously (14). The potential effects of GSH and sulfide on PDO activity was examined in addition to the effect of sulfite (a PDO product) and thiosulfate (rhodanese substrate/product)

(Table 3.3). Sulfite, which consumed $O_2$, increased the background rate and was therefore used at a lower concentration (0.6 mM) than the other metabolites (5 mM each). GSH was slightly activating (1.3-fold increase in $k_{cat}/K_{m(GSSH)}$) as seen previously with human PDO (14). Thiosulfate was without effect, while $H_2S$ and sulfite decreased $k_{cat}/K_{m(GSSH)}$ 1.6- and 2.2-fold.

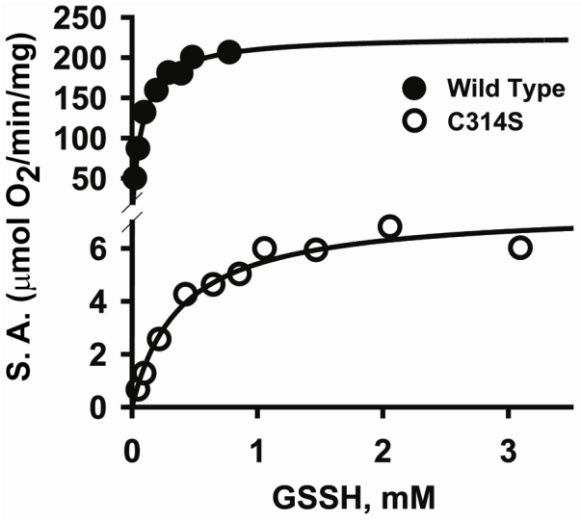


**Figure 3.6. Kinetics of PDO activity of *Bp*PRF.** Dependence of PDO activity on GSSH concentration for wild-type *Bp*PRF (solid circles) and C314S *Bp*PRF (open circles). Oxygen consumption by *Bp*PRF in 100 mM sodium phosphate buffer, pH 7.4, was monitored at 22 ˚C in the presence of varying concentration of GSSH. The data are representative of three independent experiments.

TABLE 3.2. **Comparison of the PDO activities of wild-type and C314S *Bp*PRF.**[a]

| Enzyme | Iron Content | $V_{max}$ | $K_m$ (GSSH) | $K_m$ ($O_2$) | $k_{cat}$ | $k_{cat}/K_m$ (GSSH) | $k_{cat}/K_m$ ($O_2$) |
|---|---|---|---|---|---|---|---|
| | *mol Fe/mol* | *$\mu$mol min$^{-1}$ mg$^{-1}$* | *mM* | *mM* | *$s^{-1}$* | *$mM^{-1}$ $s^{-1}$* | *$mM^{-1}$ $s^{-1}$* |
| Wild type | 0.60 ± 0.03 | 207 ± 6 | 0.070 ± 0.008 | 0.13 ± 0.03 | 143 | 2043 | 1100 |
| C314S | 0.46 ± 0.02 | 7.3 ± 0.1 | 0.37 ± 0.04 | --- | 5 | 14 | --- |

[a]The kinetic parameters were determined by monitoring $O_2$ consumption in the presence of GSSH at 22 ˚C and pH 7.4, as described under Experimental Procedures.

TABLE 3.3. **Influence of sulfur-containing additives on the kinetics of the PDO activity of *Bp*PRF.**[a]

| Additive | $V_{max}$ | $K_m$ | $k_{cat}$ | $k_{cat}/K_m$ |
|---|---|---|---|---|
| | *$\mu$mol min$^{-1}$ mg$^{-1}$* | *mM* | *$s^{-1}$* | *$mM^{-1}$ $s^{-1}$* |
| None | 207 ± 6 | 0.070 ± 0.08 | 143 | 2043 |
| 5 mM GSH | 410 ± 8 | 0.103 ± 0.007 | 283 | 2748 |
| 5 mM $S_2O_3^{2-}$ | 302 ± 18 | 0.12 ± 0.02 | 209 | 1742 |
| 5 mM $Na_2S$ | 186 ± 10 | 0.10 ± 0.01 | 127 | 1270 |
| 0.6 mM $SO_3^{2-}$ | 232 ± 10 | 0.17 ± 0.03 | 160 | 941 |

[a]The kinetic parameters were determined by monitoring $O_2$ consumption in the presence of GSSH as described under Experimental Procedures.

### 3.4.6. Sulfurtransferase activity of BpPRF

Conversion of cyanide to thiocyanate in the presence of thiosulfate (Eq. 3.5) was used to monitor the sulfurtransferase activity of *Bp*PRF (Figs. 3.7A and 3.8A). From this analysis,

$$S_2O_3^{2-} + CN^- \rightarrow SO_3^{2-} + SCN^- \qquad [3.5]$$

$K_{m(thiosulfate)}$ of 5.4± 0.7 mM, $K_{m(CN^-)}$ of 22.7 ± 0.7 mM and $k_{cat}$ of 5.1 $s^{-1}$ at 22 ˚C were obtained (Table 3.4). Under the same conditions, the sulfurtransferase activity of the C314S mutant, carrying an inactivating mutation in the rhodanese domain, was not detectable (data not shown).

Since GSSH, a product of the sulfurtransferase reaction (Eq. 3.2), is a substrate for the PDO domain (Eq. 3.3), this activity was monitored in a "coupled" assay, i.e. by detecting $O_2$

consumption (Figs. 3. 7C and 3.8C). This assay yielded the following parameters: $K_{m(GSH)}$ = 4.7 ± 0.7 mM, $K_{m(thiosulfate)}$ = 3.1 ± 0.2 mM and $k_{cat}$ = 6.2 $s^{-1}$ (Table 3). The same reaction was also monitored directly, i.e. by detecting sulfite (Eq. 3.2) colorimetrically, and yielded essentially the same results (not shown).

Cysteine was tested as an alternate sulfur acceptor in lieu of GSH, by monitoring $H_2S$ production using the lead sulfide assay (Eqs. 3.6 and 3.7) (Figs.3.7E and 3.8E).

$$S_2O_3^{2-} + \text{Cys-SH} \rightarrow SO_3^{2-} + \text{Cys-SSH} \qquad [3.6]$$

$$\text{Cys-SSH} + \text{Cys-SH} \rightarrow \text{Cys-S-S-Cys} + H_2S \qquad [3.7]$$

This analysis yielded the following values: $K_{m(Cys)}$ = 5.2 ± 0.4 mM, $K_{m(thiosulfate)}$ = 5.8 ± 0.8 mM and $k_{cat}$ = 0.2 $s^{-1}$. Given the relatively low cellular concentration of cysteine versus GSH and the considerably lower $k_{cat}/K_{m(cys)}$ value (Table 3.4), cysteine is unlikely to be a physiologically relevant sulfur acceptor for *Bp*PRF.

Next, we attempted to monitor sulfurtransferase activity in the opposite direction (i.e. reverse of Eq. 3.2) by tracking thiosulfate formation under anaerobic conditions (to inhibit GSSH consumption by PDO). However, unlike human rhodanese (18,20), sulfur transfer activity from GSSH to sulfite was not detected with *Bp*PRF.

TABLE 3.4. **Kinetic parameters for the sulfurtransferase activity of *Bp*PRF**[c]

| Donor | Acceptor | $V_{max}$ | $K_m$ *Donor* | $K_m$ *Acceptor* | $k_{cat}$ | $k_{cat}/K_m$ *Donor* | $k_{cat}/K_m$ *Acceptor* |
|---|---|---|---|---|---|---|---|
| | | $\mu mol\ min^{-1}\ mg^{-1}$ | *mM* | *mM* | $s^{-1}$ | $mM^{-1}\ s^{-1}$ | $mM^{-1}\ s^{-1}$ |
| 1. $S_2O_3^{2-}$ | $CN^-$ | 7.4 ± 0.3 | 5.4 ± 0.7 | 22.7 ± 0.7 | 5.1 | 0.9 | 0.2 |
| 2. GSSH | $SO_3^{2-}$ | nd | nd | nd | nd | nd | nd |
| 3. $S_2O_3^{2-}$ | GSH | 8.9 ± 0.2 | 3.1 ± 0.2 | 4.7 ± 0.4 | 6.2 | 2.0 | 1.3 |
| 4. $S_2O_3^{2-}$ | Cys | 0.32 ± 0.01 | 5.8 ± 0.8 | 5.2 ± 0.4 | 0.2 | 0.04 | 0.04 |

[c]The kinetic parameters for the sulfur transfer reactions 1-4 were determined at pH 7.4 as follows. Reaction 1 monitored thiocyanate formation (22 ˚C), Reaction 2, monitored thiosulfate formation (22 ˚C), Reaction 3, monitored sulfite formation (at 22 ˚C), or GSSH formation (via $O_2$ consumption in the coupled PDO reaction at 22 ˚C), or $H_2S$ formation (37 ˚C), and Reaction 4, monitored $H_2S$ formation (37 ˚C), as described in the Experimental Procedures.

TABLE 3.5. **Kinetic parameters for the isolated rhodanese domain of *Bp*PRF**[d]

| Donor | Acceptor | $V_{max}$ | $K_m$ *Donor* | $K_m$ *Acceptor* | $k_{cat}$ | $k_{cat}/K_m$ *Donor* | $k_{cat}/K_m$ *Acceptor* |
|---|---|---|---|---|---|---|---|
| | | $\mu mol\ min^{-1}\ mg^{-1}$ | *mM* | *mM* | $s^{-1}$ | $mM^{-1}\ s^{-1}$ | $mM^{-1}\ s^{-1}$ |
| $S_2O_3^{2-}$ | $CN^-$ | 18 ± 1 | 9.2 ± 0.8 | 23 ± 1 | 4.6 | 0.5 | 0.2 |
| GSSH | $SO_3^{2-}$ | nd | nd | nd | nd | nd | nd |
| $S_2O_3^{2-}$ | GSH | 35 ± 2 | 3.8 ± 0.5 | 14.9 ± 0.5 | 9.0 | 2.3 | 0.6 |
| $S_2O_3^{2-}$ | Cys | 3.1 ± 0.1 | 6.1 ± 0.4 | 5.4 ± 0.3 | 0.8 | 0.1 | 0.1 |

[d]The kinetic parameters of the sulfur transfer reactions catalyzed by the isolated rhodanese domain were determined as summarized in Table 3.3 legend and described in detail under Experimental Procedures.

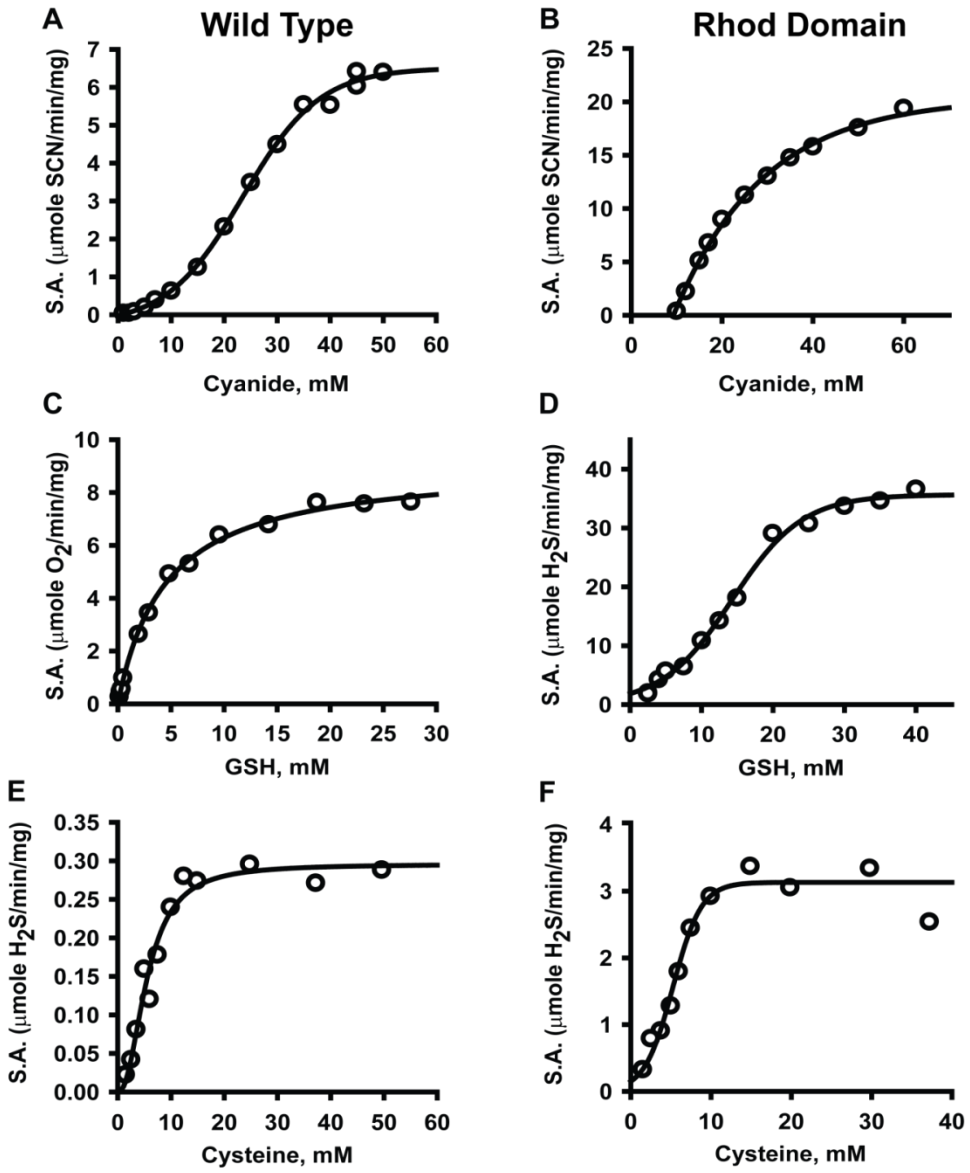


**Figure 3.7. Kinetics of *Bp*PRF-catalyzed sulfur transfer reactions.** The sulfurtransferase activity associated with the rhodanese domain in wild-type *Bp*PRF (A, C, E) or with the isolated rhodanese domain (Rhod domain) (B, D, F) was determined in the presence of a constant thiosulfate concentration (60 mM) and varying concentrations of cyanide (A and B), GSH, (C and D) or cysteine (E and F). The data are representative of 3-4 independent experiments. The data were fitted with the Michaelis Menten or sigmoidal equation as described under Experimental Procedures.

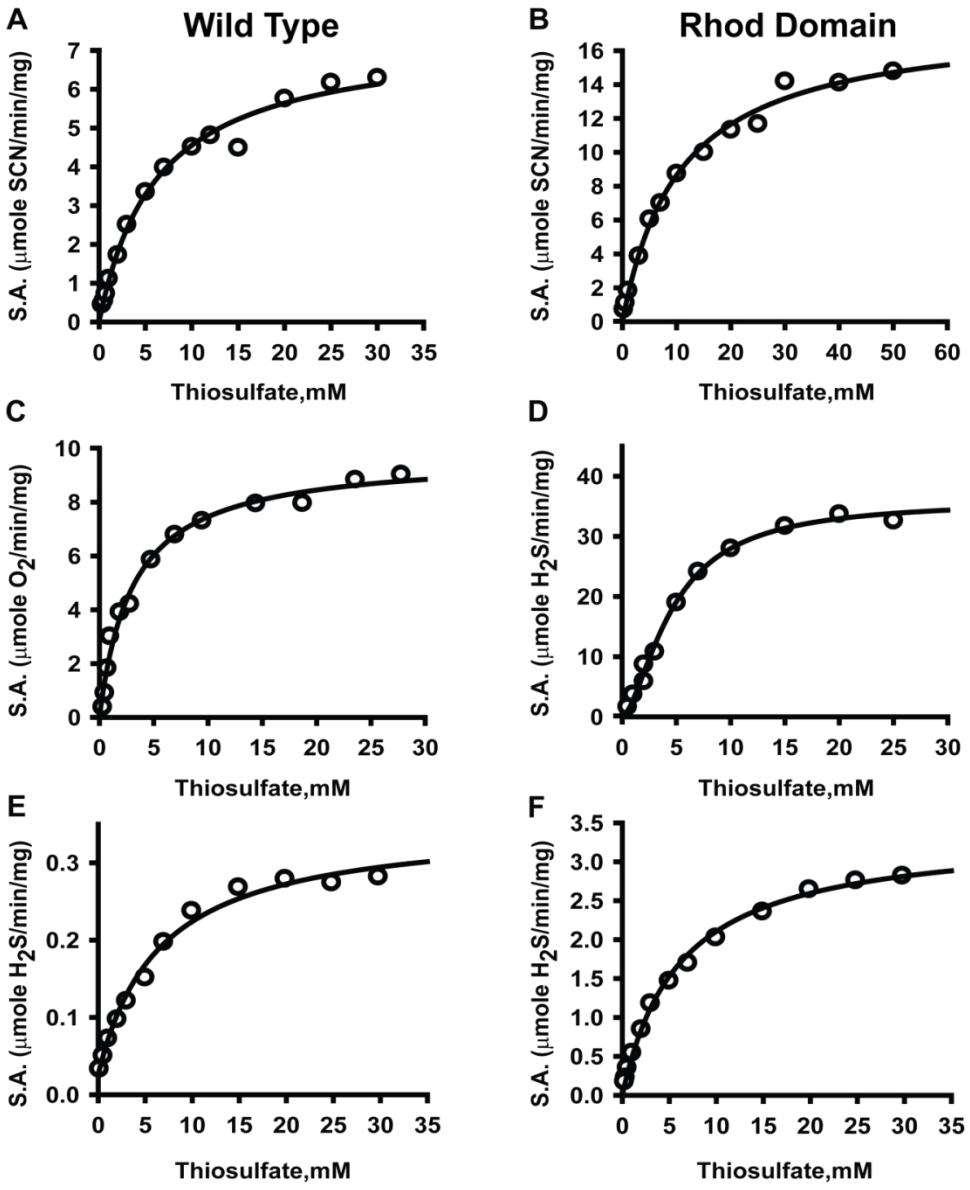


**Figure 3.8. Kinetics of *Bp*PRF-catalyzed sulfur transfer reactions.** Dependence of sulfurtransferase activty on varying thiosulfate concentrations in the presence of 60 mM cyanide (A and B), 30 mM GSH (C and D), and 50 mM cysteine (E and F) for wild-type BpPRF and the isolated rhodanese domain (Rhod Domain). The reactions were performed as described under Experimental Procedures. The data are representative of 3-4 independent experiments. Data were fitted with either the Michaelis Menten or sigmoidal equation.

### 3.4.7. Sulfurtransferase activity of the rhodanese domain

The isolated rhodanese domain is active and exhibits the following kinetic parameters in the cyanide detoxification assay (Fig. 3.7B, 3.8B): $K_{m(thiosulfate)}$ = 9.2 ± 0.8 mM and $K_{m(CN^-)}$ = 23

± 1 mM, $k_{cat}$ = 4.6 $s^{-1}$ (Table 4), which are very similar to those for full-length *Bp*PRF. GSSH synthesis from thiosulfate and GSH (Eq. 3.2) was monitored by following $H_2S$ formation (Eq. 3.8) (Fig. 3.7D and 3.8D).

$$GSSH + GSH \rightarrow GSSG + H_2S \qquad [3.8]$$

The following values were obtained from this analysis: $K_{m(GSH)}$ = 14.9 ± 0.5 mM and a $K_{m(thiosulfate)}$ = 3.8 ± 0.5 mM and $k_{cat}$ = 9.0 $s^{-1}$. As with the full-length protein, cysteine was a poor acceptor (6-fold lower $k_{cat}/K_m$ than GSH (Fig. 3.7F and 3.8F) and the reverse reaction (i.e. transfer from GSSH to sulfite) was not detectable (Table 3.5). Similar values for the kinetic parameters were obtained when the rate of sulfite production was detected (data not shown).

### 3.4.8. Stoichiometry of PRF reaction

Our kinetic data predicts that *Bp*PRF can catalyze a GSH dependent net oxidation of thiosulfate to sulfite (Eqs. 3.2 and 3.3). To verify this prediction, the stoichiometry of thiosulfate and $O_2$ consumed to sulfite formed was determined. As noted previously, the method used to synthesize GSSH results in an equivalent of GSH being present, which together with unreacted GSSG and an ~3-fold excess of $H_2S$, would confound the reaction stoichiometry. To circumvent this problem, GSSH was synthesized in situ using GSH and thiosulfate as substrates (Eq. 3.2).

Under single turnover conditions, the stoichiometry of sulfite formed/thiosulfate consumed/oxygen consumed was 2:1:1 (Fig. 3.9A) as predicted by Eqs. 3.2 and 3.3. Also, as expected, the reaction stoichiometry of sulfite formed/GSH consumed/thiosulfate consumed was 1:1:1 in the absence of oxygen (Fig. 3.9B).

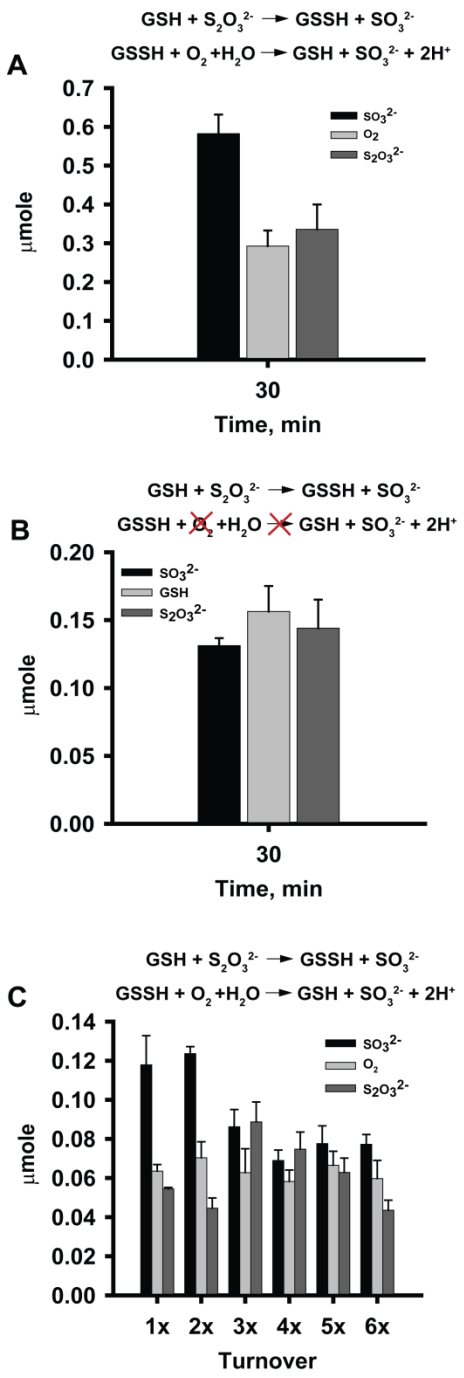


**Figure 3.9. Product analysis and reaction stoichiometry of the *Bp*PRF-**The reaction stoichiometry of *Bp*PRF under single turnover conditions was analyzed in the presence (*A*) and absence (*B)* of oxygen. The reactions were performed in the presence of 250 μM GSH, 250 μM thiosulfate and 250 μM enzyme. *C*, The stoichiometry of *Bp*PRF reactions under multiple turnover conditions was analyzed in the presence of 250 μM GSH, 250 μM thiosulfate and decreasing enzyme concentrations as described under Experimental Procedures.

However, when the *Bp*PRF reaction was monitored under multiple turnover conditions in the presence oxygen, the stoichiometry of sulfite formed/thiosulfate consumed/oxygen consumed switched to 1:1:1 after three turnovers (Fig. 3.9C). This change in stoichiometry indicates inefficient coupling between the PDO and rhodanese active sites, and is likely confounded by side reactions of the reactive products, particularly GSSH (46), as it builds up under these conditions.

**3.5 Discussion**

Natural fusions of PDO and rhodanese are found in bacteria and suggest a functional interaction between them in other organisms, where they are expressed as stand-alone proteins (47). In this study, we provide the first structural and kinetic characterization of a PRF. To our knowledge, the only other PRF that has been biochemically characterized is CstB from *S. aureus* (23,30,48), but the available CstB structure is missing density for the catalytic rhodanese domain. CstB is located in the *cst* operon (Fig. 3.1C). Its operonic partners include CstA, which is a rhodanese, and a sulfide quinone oxidoreductase, which oxidizes $H_2S$ to polysulfides (30). Expression of the *cst* operon is regulated by the persulfide/polysulfide-sensing repressor CstR and is induced by exogenous addition of $H_2S$ or polysulfides (49). CstB catalyzes the conversion of low molecular weight persulfides to thiosulfate via the intermediate formation of sulfite (Eq. 3.9) (23). In contrast to CstB, *Bp*PRF preferentially catalyzes sulfur transfer in the reverse

$$2RSSH + O_2 + H_2O \rightarrow 2S_2O_3^{2-} + 2RSH + 2H^+ \qquad [3.9]$$

direction, i.e. from thiosulfate to sulfite (Eq. 3.10), which was confirmed under single turnover conditions (Fig. 3.8).

$$S_2O_3^{2-} + O_2 + H_2O \rightarrow 2SO_3^{2-} + 2\ H^+ \qquad [3.10]$$

GSSH serves as the intermediate sulfur carrier in the *Bp*PRF reaction, transferring sulfur processed in the rhodanese active site to the PDO active site. Unlike CstB, which functions in the sulfide stress response, the cellular context in which *Bp*PRF functions, is not known (49). Since the gene encoding *Bp*PRF does not reside in an operon, the metabolic context in which it functions is not immediately obvious. The *Bp*PRF-encoding gene is located downstream from a putative peroxidase and a putative LysR-type regulator, which have been shown to be involved in regulating bacteria mobility, virulence, metabolism and quorum sensing (50) (Fig. 3.1C). A potential fate of sulfite, which is toxic, is its oxidation by sulfite oxidase to sulfate, which could be utilized in an assimilatory sulfate-reducing pathway. *B. phytofirmans* encodes a putative sulfite oxidase. Alternatively, *Bp*PRF might be involved in sulfur assimilation from thiosulfate and sulfite could be reduced by sulfite reductase (encoded by *B. phytofirmans*) to $H_2S$, which in turn is used for cysteine synthesis. In *B. cenocepacia,* CysB and SsuR regulate genes encoding enzymes involved in the aliphatic sulphonate assimilation pathway (25,51). BLAST analysis reveals that *B. phytofirmans* possesses two gene products that have 23 and 26% identity to the CysB and SsuR transcriptional regulators, respectively. Bioinformatic analysis of the sequence 100 base pairs upstream of the *Bp*PRF gene queried against CysB and SsuR binding sites, was performed using the FIMO MEME suite database (25,51,52). Several SsuR binding sites (Fig. 3.10) scored as positive motifs hits in the *Bp*PRF promoter region ($p < 0.005$), consistent with a role for *Bp*PRF in sulfur assimilation.

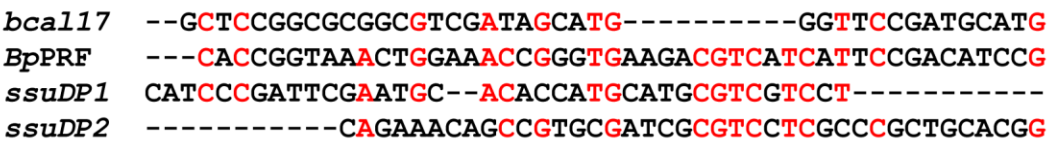


**Figure 3.10. Comparison of *B. cenocepacia* SsuR binding site sequences to the *Bp*PRF promoter region**. Alignment of *Bp*PRF promoter region with predicted SsuR binding sites that displayed high-scoring motif occurrences as assessed by the FIMO MEME suite database (*p*-value ≤ 0.005). While there is no obvious consensus sequence in the four promoter regions, similarities are observed. Nucleotides conserved in at least three of the four promoter sequences are shown in red.

The catalytic efficiency of *Bp*PRF ($k_{cat}/K_{m(GSSH)}$ = 2 × $10^6$ $M^{-1}s^{-1}$ at 22 ˚C) is 14-fold higher than of human PDO (1.4 × $10^5$ $M^{-1}s^{-1}$ at 22 ˚C. (14)) and ~$10^2$-fold higher than for CstB with its preferred substrate, CoASSH (18 × $10^3$ $M^{-1}s^{-1}$ at 25 ˚C) (23). Mutation of the catalytic cysteine residue, C314, in the rhodanese domain decreased iron content 1.3-fold and PDO activity, 29-fold. This result is surprising and indicates communication between the rhodanese and PDO active sites, which are however distant and oriented 90 ˚ away from each other in the crystal structure (Fig. 3.3A).

The thiosulfate:cyanide sulfurtransferase activity of *Bp*PRF ($k_{cat}$ = 5.1 $s^{-1}$ at 22 ˚C) is comparable to that of CstB (8.5 $s^{-1}$ at 25 ˚C) (23), and 180-730-fold lower than human rhodanese (20). The thiosulfate:GSH sulfur transfer activity of *Bp*PRF ($k_{cat}$ = 6.2 $s^{-1}$ at 37 ˚C) is 9-fold higher than for human rhodanese (0.67 $s^{-1}$ at 37 ˚C), which preferentially catalyzes the reaction in the reverse GSSH:sulfite sulfur transfer direction ($k_{cat}$ = 389 $s^{-1}$ at 25 ˚C). The isolated rhodanese domain was well-folded as evidenced by its high $T_m$ (55 ± 2 °C) versus that of the full-length protein (50 ± 2 °C) and its comparable $k_{cat}$ values in the thiosulfate:cyanide and thiosulfate:GSH sulfur transfer reactions (Tables 3.4 and 3.5). The isolated rhodanese domain exhibits a sigmoidal dependence on GSH and thiosulfate concentration (Fig 3.7D and 3.8D), in contrast to the hyperbolic dependence observed with full-length *Bp*PRF (Fig. 3.7C and 3.8C).

This difference in behavior could be due to approximately half of the isolated rhodanese domain existing as a dimer in solution while the full-length protein is a monomer. Unlike human rhodanese, sulfur transfer from GSSH to sulfite was not detectable with either the full-length *Bp*PRF or the stand-alone rhodanese domain (Tables 3.4 and 3.5).

It is possible that our structure of *Bp*PRF represents an "open" conformation versus a "closed" conformation in which the two domains are proximal to each other. We therefore attempted to model a putative closed conformation by superimposing the PDO and rhodanese domains on the structure of *Aa*PRF. In the latter, the PDO and rhodanese active sites are positioned directly across from each other and are separated by a distance of 27 Å (Fig. 3.11A). *Aa*PRF contains an additional non-catalytic rhodanese domain and a cysteine-containing loop (C202, *Aa*PRF numbering) located in the PDO domain active site. This loop, while absent in *Bp*PRF, is also present in CstB and postulated to facilitate substrate transfer between the PDO and catalytic rhodanese domains (23). To adopt a similar domain orientation, the 15-amino acid residue linker region of *Bp*PRF, which is ~36 Å in length, would have to span 47 Å and possibly require the unwinding of a secondary structure element. Furthermore, the electrostatic surface potential map reveals that positively charged resides line the entrance to the PDO and rhodanese active sites, suggesting that a direct interaction between them would be unfavorable (Fig. 3.11B). The structural independence of the active sites is also consistent with the high catalytic activity of the isolated rhodanese domain. This result is in contrast to CstB in which the rhodanese domain, once isolated, does not retain activity (23).

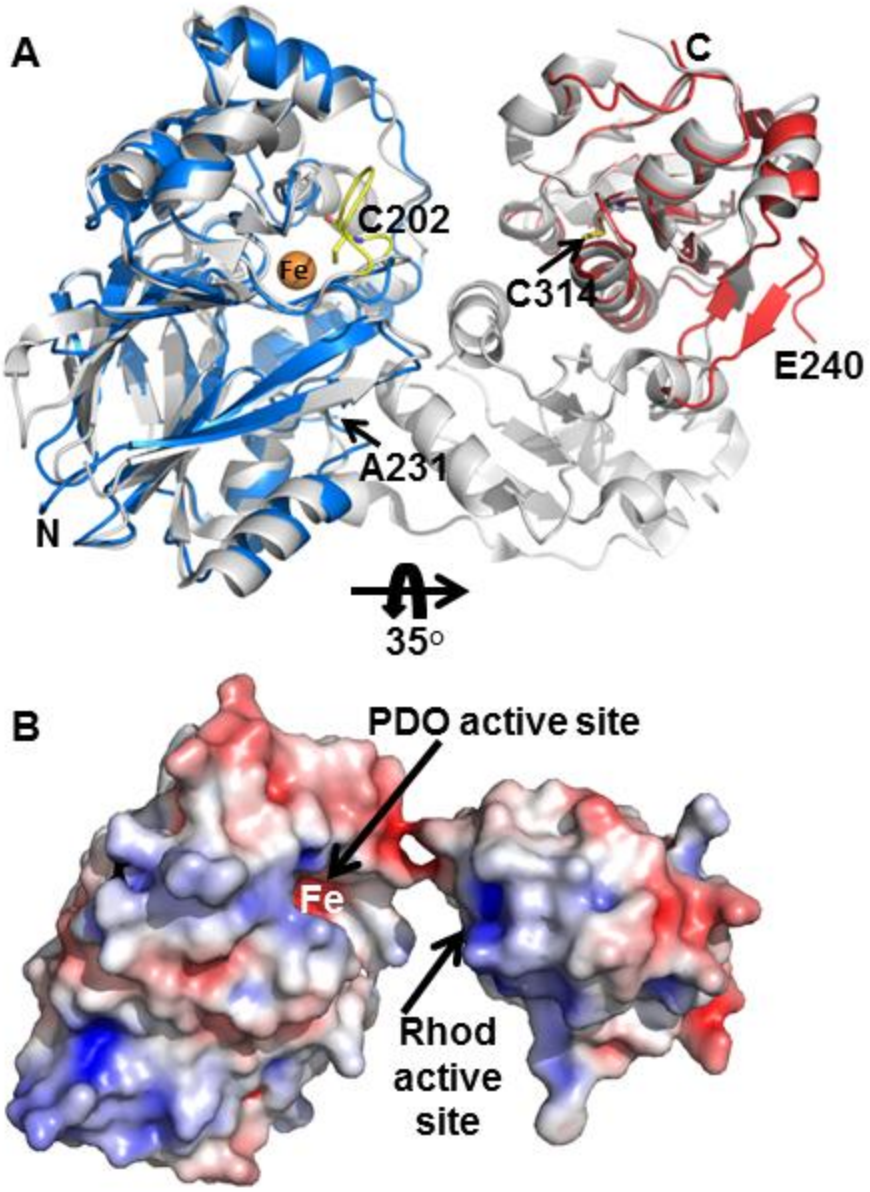


**Figure 3.11. Modeling of potential *Bp*PRF domain interaction interface.** *A*, overlay of *Bp*PRF PDO domain (blue) and the *Bp*PRF rhodanese domain (red) with the PDO domain and catalyic rhodanese domain of *Aa*PRF (PDB ID: 3TP9) (shown in grey). The active site loop of *Aa*PRF with C202 facing the iron center is shown in yellow. The *Bp*PRF active site iron is shown as an orange sphere. The N- and C-termini of *Bp*PRF are labeled. *B*, Surface electrostatic potential of the *Bp*PRF domains in the same orientation as in *A* but rotated by 35˚. The arrows highlight locations of the PDO and rhodanese (Rhod) active sites. Positive and negative electrical potential are shown in blue and red, respectively, and represent a range of -5 to +5 kT/e.

An overlay of five structures, i.e. two per asymmetric unit of wild-type *Bp*PRF and three per asymmetric unit of C314S *Bp*PRF, was used to assess significant conformational differences,

if any, between them (Fig. 3.12). Since the electron density for eight residues in the linker region was missing in these structures, the overlay was used to assess whether the flexible linker might allow a closer approach of the rhodanese and PDO domains, permitting a closed conformation. However, no significant conformational differences were observed between the structures (Fig. 3.12).

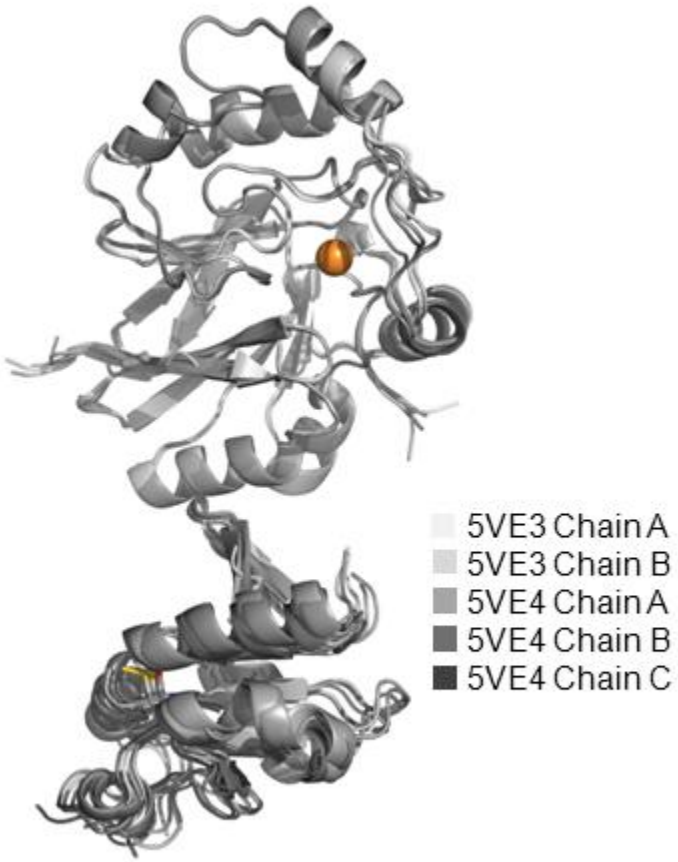


**Figure 3.12**. **Overalay of five *Bp*PRF structures shows low conformational variability among them.** The figure was generated by aligning the PDO domains (residues 1-231) using Pymol. The iron in the PDO domain is shown as an orange sphere. The overlay reveals minor variations in the position of the rhodanese domain and suggests limited mobility of the intervening linker region.

In summary, the relative orientation of the two domains in *Bp*PRF and their separation by a relatively short linker, suggests that the two active sites do not interact. In fact, the similar potential electrostatic surface map also suggests that the active sites are unlikely to interact directly. In light of the structural data, it is intriguing that the kinetic data provide some evidence for allosteric communication between the domains. For instance, mutation of the catalytic cysteine in the rhodanese domain adversely impacts the catalytic properties and to a lesser extent, the iron content of the PDO domain. Similarly, isolation of the rhodanese domain, improves its $k_{cat}$. Our kinetic data are consistent with a role for *Bp*PRF in sulfur assimilation rather than in a sulfide stress response pathway.

### 3.6 References


1. Beauchamp, R. O., Jr., Bus, J. S., Popp, J. A., Boreiko, C. J., and Andjelkovich, D. A. (1984) *Crit Rev Toxicol* **13**, 25-97

2. Kimura, H. (2010) *Antioxid Redox Signal* **12**, 1111-1123

3. Kabil, O., and Banerjee, R. (2010) *J Biol Chem* **285**, 21903-21907

4. Kabil, O., Motl, N., and Banerjee, R. (2014) *Biochim Biophys Acta* **1844**, 1355-1366

5. Zhao, W., Zhang, J., Lu, Y., and Wang, R. (2001) *EMBO J* **20**, 6008-6016

6. Elrod, J. W., Calvert, J. W., Morrison, J., Doeller, J. E., Kraus, D. W., Tao, L., Jiao, X., Scalia, R., Kiss, L., Szabo, C., Kimura, H., Chow, C. W., and Lefer, D. J. (2007) *Proc Natl Acad Sci U S A* **104**, 15560-15565

7. Wallace, J. L., Vong, L., McKnight, W., Dicay, M., and Martin, G. R. (2009) *Gastroenterology* **137**, 569-578, 578 e561

8. Gao, X. H., Krokowski, D., Guan, B. J., Bederman, I., Majumder, M., Parisien, M., Diatchenko, L., Kabil, O., Willard, B., Banerjee, R., Wang, B., Bebek, G., Evans, C. R., Fox, P. L., Gerson, S. L., Hoppel, C., Liu, M., Arvan, P., and Hatzoglou, M. (2015) *eLife* **4**

9. Vitvitsky, V., Kabil, O., and Banerjee, R. (2012) *Antioxid Red Signal* **17**, 22-31

10. Banerjee, R. (2017) *Curr Opin Chem Biol* **37**, 115-121

11. Singh, S., and Banerjee, R. (2011) *Biochim Biophys Acta* **1814**, 1518-1527

12. Hildebrandt, T. M., and Grieshaber, M. K. (2008) *FEBS J* **275**, 3352-3361

13. Mishanina, T. V., Libiad, M., and Banerjee, R. (2015) *Nat Chem Biol* **11**, 457-464
14. Kabil, O., and Banerjee, R. (2012) *J Biol Chem* **287**, 44561-44567

15. Pettinati, I., Brem, J., McDonough, M. A., and Schofield, C. J. (2015) *Hum Mol Genet* **24**, 2458-2469

16. Tiranti, V., Briem, E., Lamantea, E., Mineri, R., Papaleo, E., De Gioia, L., Forlani, F., Rinaldo, P., Dickson, P., Abu-Libdeh, B., Cindro-Heberle, L., Owaidha, M., Jack, R. M., Christensen, E., Burlina, A., and Zeviani, M. (2006) *J Med Genet* **43**, 340-346

17. Tiranti, V., D'Adamo, P., Briem, E., Ferrari, G., Mineri, R., Lamantea, E., Mandel, H., Balestri, P., Garcia-Silva, M. T., Vollmer, B., Rinaldo, P., Hahn, S. H., Leonard, J., Rahman, S., Dionisi-Vici, C., Garavaglia, B., Gasparini, P., and Zeviani, M. (2004) *Am J Hum Genet* **74**, 239-252

18. Libiad, M., Yadav, P. K., Vitvitsky, V., Martinov, M., and Banerjee, R. (2014) *J Biol Chem* **289**, 30901-30910

19. Bordo, D., and Bork, P. (2002) *EMBO Rep* **3**, 741-746

20. Libiad, M., Sriraman, A., and Banerjee, R. (2015) *J Biol Chem* **290**, 23579-23588

21. Melideo, S. L., Jackson, M. R., and Jorns, M. S. (2014) *Biochemistry* **53**, 4739-4753

22. Spallarossa, A., Forlani, F., Carpen, A., Armirotti, A., Pagani, S., Bolognesi, M., and Bordo, D. (2004) *J Mol Biol* **335**, 583-593

23. Shen, J., Keithly, M. E., Armstrong, R. N., Higgins, K. A., Edmonds, K. A., and Giedroc, D. P. (2015) *Biochemistry* **54**, 4542-4554

24. Barton, L. L., Fardeau, M.-L., and Fauque, G. D. (2014) Hydrogen Sulfide: A Toxic Gas Produced by Dissimilatory Sulfate and Sulfur Reduction and Consumed by Microbial Oxidation. in *The Metal-Driven Biogeochemistry of Gaseous Compounds in the Environment* (Kroneck, P. M. H., and Torres, M. E. S. eds.), Springer Netherlands, Dordrecht. pp 237-277

25. Iwanicka-Nowicka, R., Zielak, A., Cook, A. M., Thomas, M. S., and Hryniewicz, M. M. (2007) *J Bacteriol* **189**, 1675-1688

26. Shatalin, K., Shatalina, E., Mironov, A., and Nudler, E. (2011) *Science* **334**, 986-990

27. Motl, N., Yadav, P. K., and Banerjee, R. (2013) Enzymology of Hydrogen Sulfide Turnover. in *Hydrogen Sulfide and its Therapeutic Applications* (Kimura, H. ed.), Springer. pp 1-35

28. Czyzewski, B. K., and Wang, D. N. (2012) *Nature* **483**, 494-497

29. Sattler, S. A., Wang, X., Lewis, K. M., DeHan, P. J., Park, C. M., Xin, Y., Liu, H., Xian, M., Xun, L., and Kang, C. (2015) *J Biol Chem* **290**, 18914-18923

30. Shen, J., Peng, H., Zhang, Y., Trinidad, J. C., and Giedroc, D. P. (2016) *Biochemistry* **55**, 6524-6534

31. Sessitsch, A., Coenye, T., Sturz, A. V., Vandamme, P., Barka, E. A., Salles, J. F., Van Elsas, J. D., Faure, D., Reiter, B., Glick, B. R., Wang-Pruski, G., and Nowak, J. (2005) *Int J Syst Evol Microbiol* **55**, 1187-1192

32. Fischer, D. S., and Price, D. C. (1964) *Clin Chem* **10**, 21-31

33. Sörbo, B. H. (1953) *Acta Chem. Scand.* **7**, 1137-1145

34. Chauncey, T. R., Uhteg, L. C., and Westley, J. (1987) *Methods Enzymol* **143**, 350-354

35. Kabsch, W. (2010) *Acta Crystallogr D* **66**, 125-132

36. Long, F., Vagin, A. A., Young, P., and Murshudov, G. N. (2008) *Acta Crystallogr D Biol Crystallogr* **64**, 125-132

37. Emsley, P., and Cowtan, K. (2004) *Acta Crystallogr D Biol Crystallogr* **60**, 2126-2132

38. Adams, P. D., Afonine, P. V., Bunkoczi, G., Chen, V. B., Davis, I. W., Echols, N., Headd, J. J., Hung, L. W., Kapral, G. J., Grosse-Kunstleve, R. W., McCoy, A. J., Moriarty, N. W., Oeffner, R., Read, R. J., Richardson, D. C., Richardson, J. S., Terwilliger, T. C., and Zwart, P. H. (2010) *Acta Crystallogr D Biol Crystallogr* **66**, 213-221

39. Chen, V. B., Arendall, W. B., 3rd, Headd, J. J., Keedy, D. A., Immormino, R. M., Kapral, G. J., Murray, L. W., Richardson, J. S., and Richardson, D. C. (2010) *Acta Crystallogr D Biol Crystallogr* **66**, 12-21

40. Baker, N. A., Sept, D., Joseph, S., Holst, M. J., and McCammon, J. A. (2001) *Proc Natl Acad Sci U S A* **98**, 10037-10041

41. Dolinsky, T. J., Czodrowski, P., Li, H., Nielsen, J. E., Jensen, J. H., Klebe, G., and Baker, N. A. (2007) *Nucleic Acids Res* **35**, W522-525

42. Dolinsky, T. J., Nielsen, J. E., McCammon, J. A., and Baker, N. A. (2004) *Nucleic Acids Res* **32**, W665-667

43. The PyMol Molecular Graphics System. Version 1.3–1.4 Ed., Schrodinger, LLC

44. McCoy, J. G., Bingman, C. A., Bitto, E., Holdorf, M. M., Makaroff, C. A., and Phillips, G. N., Jr. (2006) *Acta Crystallogr D Biol Crystallogr* **62**, 964-970

45. Ploegman, J. H., Drent, G., Kalk, K. H., Hol, W. G., Heinrikson, R. L., Keim, P., Weng, L., and Russell, J. (1978) *Nature* **273**, 124-129

46. Yadav, P. K., Martinov, M., Vitvitsky, V., Seravalli, J., Wedmann, R., Filipovic, M. R., and Banerjee, R. (2016) *J Am Chem Soc* **138**, 289-299

47. Tiranti, V., Viscomi, C., Hildebrandt, T., Di Meo, I., Mineri, R., Tiveron, C., Levitt, M. D., Prelle, A., Fagiolari, G., Rimoldi, M., and Zeviani, M. (2009) *Nat Med* **15**, 200-205

48. Higgins, K. A., Peng, H., Luebke, J. L., Chang, F. M., and Giedroc, D. P. (2015) *Biochemistry* **54**, 2385-2398

49. Luebke, J. L., Shen, J., Bruce, K. E., Kehl-Fie, T. E., Peng, H., Skaar, E. P., and Giedroc, D. P. (2014) *Mol Microbiol* **94**, 1343-1360

50. Maddocks, S. E., and Oyston, P. C. (2008) *Microbiology* **154**, 3609-3623

51. Lochowska, A., Iwanicka-Nowicka, R., Zielak, A., Modelewska, A., Thomas, M. S., and Hryniewicz, M. M. (2011) *J Bacteriol* **193**, 1843-1853

52. Grant, C. E., Bailey, T. L., and Noble, W. S. (2011) *Bioinformatics* **27**, 1017-1018

# Chapter 4

## Conclusions

In this chapter the results presented in Chapters II-III are summarized and future directions are discussed. As over 20 PDO mutations have been described in EE patients (1-3), we set out to characterize the biochemical penalties associated with a subset of these mutations (L55P, T136A, C161Y and R163W). The PDO mutants displayed varying degrees of decreased activity and increased $K_m$ values for the GSSH substrate. Combined with thermal stability and iron content quantification, this study revealed that perturbations of these residues led to decreased enzyme stability and activity resulting in loss of PDO function. A previous study reported that the R163W and R163Q PDO mutations lowered the iron redox potential (4). It is not known whether the three other mutations that we characterized also affected the iron redox potential and whether any of them affected the $O_2$ affinity and these properties should be assessed in the future.

The organization of the mitochondrial sulfide oxidation pathway remains in question, and future studies should focus on characterizing the interactions between PDO and SQR or rhodanese. Both the PDO substrate, GSSH, and the PDO product, sulfite, are reactive. Sulfite is a co-substrate for rhodanese, can serve as a sulfane sulfur acceptor for SQR and is a substrate for sulfite oxidase (5,6). Understanding the interactions between PDO and SQR or rhodanese might provide insights into how the reactivity of the reactive sulfur species formed in the sulfide oxidation pathway is controlled.

Next we characterized a bacterial variant of PDO that is fused to a rhodanese domain. Characterization of a PRF will facilitate modeling of the interactions between human mitochondrial PDO and rhodanese. We determined the crystal structures and kinetic properties of a PDO-rhodanese fusion protein from *Burkholderia phytofirmans* (*Bp*PRF).

Our study of the *Bp*PRF rhodanese reactions indicates that the rhodanese domain preferentially catalyzes the sulfur transfer from thiosulfate to GSH forming GSSH and sulfite (Eq. 4.1).

$$GSH + S_2O_3^{2-} \rightarrow GSSH + SO_3^{2-} \qquad [4.1]$$

Curiously, *Bp*PRF does not display detectable sulfur transfer activity in the reverse direction, i.e., from GSSH to sulfite forming GSH and thiosulfate (Eq. 4.2).

$$GSSH + SO_3^{2-} \rightarrow GSH + S_2O_3^{2-} \qquad [4.2]$$

Similar observations have been made in our laboratory for the single-domain sulfur transferase TSTD1, which also does not appear to catalyze the sulfur transfer reaction from GSSH to sulfite (Eq 4.2) (Libiad and Banerjee, unpublished results). In contrast, human rhodanese, a double-domain sulfurtransferase catalyzes sulfur transfer depicted in Eq. 4.2 preferentially with a $k_{cat}$ of 389 $s^{-1}$, a $k_{cat}/K_{m(GSSH)}$ = 0.86 x $10^6$ $M^{-1}$ $s^{-1}$ and $k_{cat}/K_{m(sulfite)}$ = 6.5 x $10^6$ $M^{-1}$ $s^{-1}$ compared to a $k_{cat}$ of 0.67 $s^{-1}$, a $k_{cat}/K_{m(GSH)}$ = 2.0 x $10^3$ $M^{-1}$ $s^{-1}$ and a $k_{cat}/K_{m(thiosulfite)}$ = 0.03 x $10^3$ $M^{-1}$ $s^{-1}$ for the reaction shown in Eq. 4.1 (5). Since GSSH and sulfite are more reactive than GSH and thiosulfate, it is expected a priori that the sulfur transfer from GSSH to sulfite to form the more stable products, GSH and thiosulfate (Eq. 4.1) would be thermodynamically favored. It is therefore surprising that neither *Bp*PRF nor TSTD1 show detectable sulfur transfer activity in the direction shown in Eq. 4.1 and suggests that one of the products (i.e. GSH or thiosulfate) might

be inhibitory. Hence, as the product builds up after a few turnovers and inhibits the reaction, it precludes product formation under multiple turnover conditions.

To address this possibility, sulfur transfer reactions under single turnover conditions should be performed. If product formation is seen under these conditions, the inhibitory compound can be readily identified by performing the same reaction under single turnover conditions but with an excess of either GSH or thiosulfate. Additionally, this study should be expanded to TSTD1 to determine if a similar mechanism of product inhibition also underlies the apparent irreversibility of its sulfur transfer reaction. Studies on the TSTD1 and human rhodanese with GSH and thiosulfate as substrates (Eq. 4.1) revealed that they displayed substrate inhibition with thiosulfate, albeit at high millimolar concentrations (5-7). These observations suggest that thiosulfate might be a potential inhibitor for the sulfur transfer reaction in the reverse direction (Eq. 4.2).

Another future direction would be to examine the function of the N-terminal human rhodanese domain. Although catalytically inactive, the exact function of this domain is unknown. It has been proposed that the N-terminal domain is important for enzyme stability and/or it may be involved in allosteric regulation (8,9). As two examples of single domain sulfur transferases, the *Bp*PRF rhodanese domain and TSTD1, do not display sulfur transfer activity towards GSSH and sulfite, it is possible that the catalytic rhodanese domain has an inherent auto-inhibitory activity, which is alleviated by the presence of the non-catalytic domain. To investigate this possibility, I propose isolation and characterization of the catalytic rhodanese domain to determine whether the absence of the non-catalytic domain affects the kinetics of the sulfur transfer reactions and, specifically, inhibits the reaction depicted by Eq. 4.1. Such a study would

provide insight into the function of the non-catalytic domain in rhodanese and aid in our understanding of how its activity is regulated.

A future subject of investigation is the nature of the interactions between the PDO and rhodanese domain of the *Bp*PRF. Kinetic analysis showed that mutagenesis of the rhodanese active site cysteine to serine decreases the PDO $k_{cat}/K_{m(GSSH)}$ 146-fold, suggesting that the domains interact. Attempts at modeling a potential interaction interface between the two active sites did not provide any obvious clues into how these sites interact as the linker does not appear to be long enough to bridge the distance between the sites and surface electrostatics do not appear to be favorable. As crystallography only provides a snapshot of the enzyme, it is possible that the domains do interact directly and the conditions for capturing a "closed" conformation of the enzyme need to be determined. The wild-type enzyme was co-crystallized in the presence of thiosulfate resulting in the observed "open" conformation. The C314S enzyme, while in a different space group, crystallized in the same "open" conformation. It is possible that co-crystallization in the presence of thiosulfate and GSH might result in a conformational change since GSH should mimic the binding interactions of the GSSH substrate. Another solution is to co-crystallize the enzyme under anaerobic conditions in the presence of the GSSH substrate, although the problem with this approach is the inherent instability of GSSH. Tyr196 is located in the PDO domain active site and participates in a hydrogen bond interaction with GSH. It would be worth exploring if Tyr196 supports fluorescence quenching studies for monitoring conformational changes in the presence of GSH or other substrates that could report on the putative "open" and "closed" conformational states of the enzyme.

Modeling for the potential interaction interface between the PDO and rhodanese domains in a monomer suggests that the linker region may not be long enough and would have to undergo

an ~90° rotation and fold up towards the PDO active site. To investigate a possible interaction between the two domains, the length of the linker can be altered. A longer linker would provide increased range of movement while a shorter linker would preclude inter-domain interactions. The effects of these changes on the oligomeric state of the enzyme and the PDO and sulfurtransferase activities should be monitored. However, if the domains act independently of one another, the length of the linker might not have an effect on the activity of the enzyme.

Another possibility to be examined is if *Bp*PRF forms a transient dimer during turnover conditions that brings the two active sites in proximity of each other. In this model, the enzyme does not adopt a closed conformation, but rather, the oligomeric state changes during catalysis. *Bp*PRF crystallized with two-copies in the unit cell, which were arranged in a head-to-tail manner with the rhodanese domain of one monomer adjacent to the PDO domain of the second monomer (Fig. 4.1A).

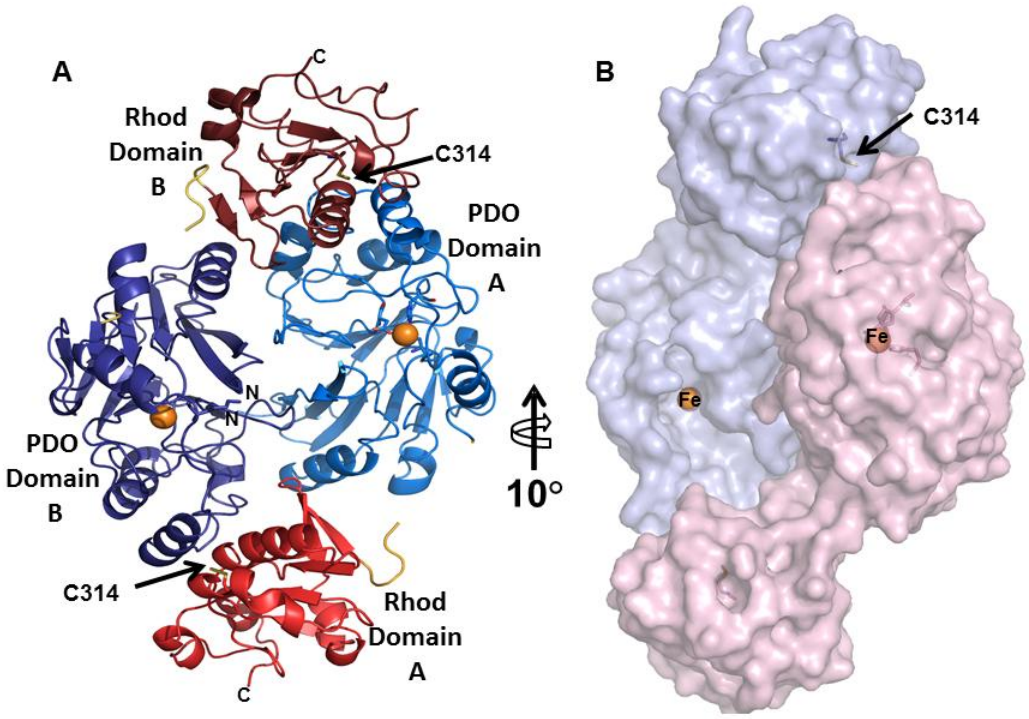


**Figure 4.1 Orientation of *Bp*PRF in the crystallographic unit cell.** Two copies of *Bp*PRF were observed in the unit cell. *A*, The *Bp*PRF monomers crystalized in a head-to-tail orientation with the rhodanese domain (red for chain A, dark red for chain B) of one monomer adjacent to the PDO domain (blue for chain A, dark blue for chain B) of the other monomer. Iron atoms are shown as orange spheres. *B*, Surface representation of the two copies of *Bp*PRF in the crystallographic unit cell. Chain A is shown in pink, and chain B is shown in blue. The iron atoms are represented as orange spheres. The PDO domain of chain A is proximal to the active site cysteine C314 of chain B, blocking solvent access. The top portion of the PDO active site groove run directly into the rhodanese domain on the adjacent chain, but does not connect to the active site cysteine.

In this head-to-tail arrangement of the *Bp*PRF monomers a surface groove runs from the PDO active site to the rhodanese domain of the adjacent monomer but blocks access to the rhodanese active site cysteine (Fig. 4.1B). It is not currently known if this is a functionally relevant interaction between monomers or an artifact of crystal packing. While transient dimer formation cannot be ruled out it would be appear to be entropically costly for monomers to come together during each catalytic cycle if the dimer is not stabilized by some ligand. Potential

experiments for investigation of a transient or stabilized dimer would involve size exclusion chromatography with multi-angle static light scattering (SEC-MALS) studies in the presence of GSH, sulfite or thiosulfate.

The *Bp*PRF rhodanese domain contains an N-terminal β-hairpin extension that is structurally unique to this rhodanese domain. A potential future direction of study is to determine the role of this unique structural feature. A possible approach is to identify key residues involved in stabilization of the β-hairpin by mutagenesis and to disrupt the structure in both the stand-alone rhodanese domain and the full length *Bp*PRF. Characterization of the activities and stability of the β-hairpin mutants will shed light on the functional role of this feature. Based on the *Bp*PRF structures, we propose that two residues would be good starting points for mutagenesis: Ser249 and Thr247, which participate in hydrogen bonds and stabilize the structure (Fig. 4.2A).

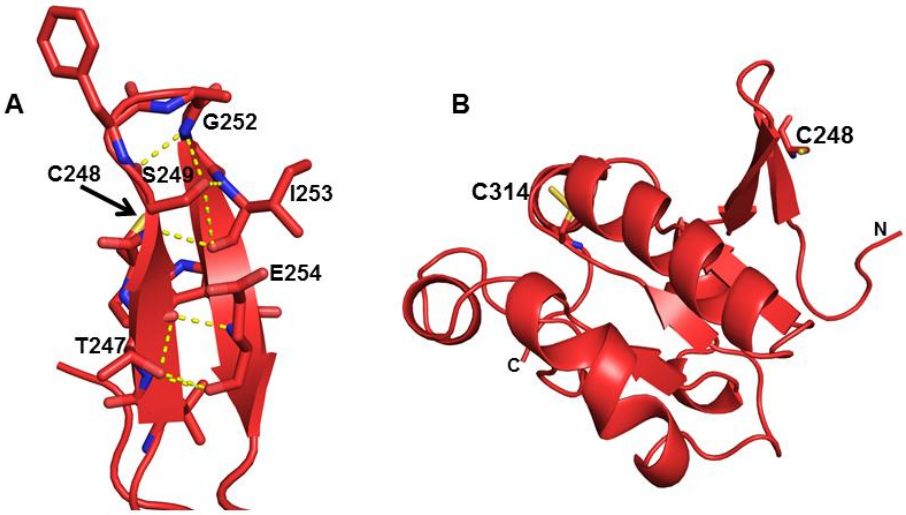


Figure 4.2**. Structural investigation of the β-hairpin extension in the *Bp*PRF rhodanese domain**. *A*, The β-hairpin secondary structure is stabilized by several hydrogen bond interactions, notably those between the functional group of Ser249 and the backbone amides of Gly252 and Ile253 and the backbone carbonyl of Ile253. Additional hydrogen bonds stabilizing the β-hairpin are between the functional group of Thr247 and the backbone amide and carbonyl

groups of Glu254. *B*, The two cysteine residues in the rhodanese domain are Cys314, the active site cysteine, and Cys248 which is located in the β-hairpin extension region. Cys248 is exposed to the surface of the enzyme and its functional group does not participate in hydrogen bonding interactions with other residues in the rhodanese domain.

The hydroxyl group of Ser249 participates in hydrogen bonds with the backbone amide group of Gly252 and the backbone amide and carbonyl groups of Ile253. The hydroxyl group of second key residue Thr247, participates in hydrogen bonds with the backbone carbonyl and nitrogen in the amide group of Glu254 on the adjacent strand.

Additionally, another key residue of interest in the β-hairpin loop is Cys248, which is surface exposed (Fig. 4.3B). As several *Bp*PRF substrates (GSSH and thiosulfate) are reactive towards cysteine, modification of Cys248 might play a regulatory role. Future study of the functional consequences of mutating this cysteine will provide insights into the possible role of the β-hairpin extension in *Bp*PRF.

One concern with the current study of the *Bp*PRF protein is that 40% of the wild-type enzyme as isolated, does not have iron bound. However, the crystallographic data suggests the enzyme is mostly if not completely loaded with iron. One possible explanation is that the only the holo-form of the enzyme is crystallized. While the colorimetric method used to quantify iron content is reliable with errors less than 5%, the Bradford assay used to determine protein concentration used bovine serum albumin as a standard, which could have led to inaccuracies in protein concentration determination and therefore to the iron to protein stoichiometry. To address the issue of whether the iron stoichiometry has been properly determined, amino acid analysis should be performed to determine the exact concentration of the *Bp*PRF.

Preliminary studies of spectral changes observed with the ferric form of the *Bp*PRF in the presence of $Na_2S$ indicated that $Na_2S$ binds with moderate affinity and leads to hydrodisulfide

(HSSH) production under anaerobic conditions. This result suggests a potentially novel role for a non-heme iron protein in polysulfide production. It remains to be seen whether *Bp*PRF can oxidize $H_2S$ under aerobic conditions to thiosulfate as reported for the heme proteins myoglobin and hemoglobin (10,11). If thiosulfate formation is supported by ferric PDO, it would help explain why elevated thiosulfate formation is seen in EE patients with mutations that lower the iron redox potential, which would favor the ferric oxidation state.

Finally, a broader question to be addressed in future studies is the function of PRF in bacteria. Our bioinformatics analysis suggests a potential role for the *Bp*PRF in a sulfur assimilation pathway, likely from thiosulfate, for eventual production of cysteine. Limited analysis of the distribution of PRF proteins performed by our laboratory (unpublished results) and others (6,12) reveals that PRF proteins are broadly distributed across both gram positive and gram negative bacteria. Future studies should include a phylogenetic analysis to better understand the distribution of PRF proteins in bacteria. Such a study would provide insights into the function of PRFs in bacterial species that are pathogenic, or occupy specialized environments and could suggest a possible advantage for bacteria that utilize PRF.

### 4.1 References


1. Tiranti, V., Briem, E., Lamantea, E., Mineri, R., Papaleo, E., De Gioia, L., Forlani, F., Rinaldo, P., Dickson, P., Abu-Libdeh, B., Cindro-Heberle, L., Owaidha, M., Jack, R. M., Christensen, E., Burlina, A., and Zeviani, M. (2006) *J Med Genet* **43**, 340-346

2. Tiranti, V., D'Adamo, P., Briem, E., Ferrari, G., Mineri, R., Lamantea, E., Mandel, H., Balestri, P., Garcia-Silva, M. T., Vollmer, B., Rinaldo, P., Hahn, S. H., Leonard, J., Rahman, S., Dionisi-Vici, C., Garavaglia, B., Gasparini, P., and Zeviani, M. (2004) *Am J Hum Genet* **74**, 239-252

3. Valente, L., Piga, D., Lamantea, E., Carrara, F., Uziel, G., Cudia, P., Zani, A., Farina, L., Morandi, L., Mora, M., Spinazzola, A., Zeviani, M., and Tiranti, V. (2009) *Biochim Biophys Acta* **1787**, 491-501

4. Henriques, B. J., Lucas, T. G., Rodrigues, J. V., Frederiksen, J. H., Teixeira, M. S., Tiranti, V., Bross, P., and Gomes, C. M. (2014) *PLoS One* **9**, e107157

5. Libiad, M., Yadav, P. K., Vitvitsky, V., Martinov, M., and Banerjee, R. (2014) *J Biol Chem* **289**, 30901-30910

6. Melideo, S. L., Jackson, M. R., and Jorns, M. S. (2014) *Biochemistry* **53**, 4739-4753

7. Jarabak, R., and Westley, J. (1974) *Biochemistry* **13**, 3233-3236

8. Libiad, M., Sriraman, A., and Banerjee, R. (2015) *J Biol Chem* **290**, 23579-23588

9. Westley, J., Adler, H., Westley, L., and Nishida, C. (1983) *Fundam Appl Toxicol* **3**, 377-382

10. Vitvitsky, V., Yadav, P. K., An, S., Seravalli, J., Cho, U. S., and Banerjee, R. (2017) *J Biol Chem* **292**, 5584-5592

11. Bostelaar, T., Vitvitsky, V., Kumutima, J., Lewis, B. E., Yadav, P. K., Brunold, T. C., Filipovic, M., Lehnert, N., Stemmler, T. L., and Banerjee, R. (2016) *J Am Chem Soc* **138**, 8476-8488

12. Shen, J., Keithly, M. E., Armstrong, R. N., Higgins, K. A., Edmonds, K. A., and Giedroc, D. P. (2015) *Biochemistry* **54**, 4542-4554